Stony Brook University

Mid Infrared III-V Semiconductor Emitters and Detectors

A Dissertation Presented

by

Seungyong Jung

to

The Graduate School

in Partial Fulfillment of the

Requirements

for the Degree of

Doctor of Philosophy

in

Electrical Engineering

Stony Brook University

December 2012

Stony Brook University

The Graduate School

Seungyong Jung

We, the dissertation committee for the above candidate for the

Doctor of Philosophy degree, hereby recommend

acceptance of this dissertation.

Gregory Belenky – Dissertation Advisor
Distinguished Professor, Department of Electrical and Computer Engineering

Sergey Suchalkin – Co-Advisor of Dissertation
Research Professor, Department of Electrical and Computer Engineering

Ridha Kamoua – Chairperson of Defense
Associate Professor, Department of Electrical and Computer Engineering

Mikhail Gouzman
Adjunct Professor, Department of Electrical and Computer Engineering

David J. Hwang
Assistant Professor, Department of Mechanical Engineering

This dissertation is accepted by the Graduate School

Charles Taber
Interim Dean of the Graduate School

Abstract of the Dissertation

Mid Infrared III-V Semiconductor Emitters and Detectors

by

Seungyong Jung

Doctor of Philosophy

in

Electrical Engineering

Stony Brook University

2012

A variety of new mid wave infrared (MWIR: 3~5 μm) and long wave infrared (LWIR: 5~10 μm) optoelectronic devices have been designed, fabricated, and characterized. Application of the strain engineering and new quinternary material into the active region of light emitting diodes (LEDs) allowed for increasing the internal quantum efficiency more than twofold. InAs/GaSb type II superlattice (SL) active region was used for the LWIR LEDs. It was experimentally demonstrated that only a few periods in the SL contribute to the radiative recombination process, which concludes that active region cascading with fewer periods will be more effective in the LWIR SL LED design. Application of the cascading scheme enabled type I QW λ=2 μm LEDs generating record quasi-continuous wave (qCW) power of 10 mW at room temperature. Novel scalable pixel design and fabrication method realized highly dimensional LED arrays with 512×512 pixels and the independently controlled dual color LED arrays emitting at 2 μm and 3 μm. A new precise technique for calibration of LED power has been developed.

For lasers, research has been focused on development of single mode tunable lasers. The diode lasers generating 100 mW room temperature CW power at 2 μm with diffraction limited beam shape have been fabricated using a cost effective wet etching technique. A new principle of laser tuning has been developed using optical pumping. Wavelength of quantum cascade lasers

emitting at 9 μm was tuned as high as 3 nm at room temperature using optical control of the effective refractive index over the lasing mode.

A novel opto-pair scheme for methane detection was designed and demonstrated. The photodetectors with nBn and nBp active region showed the specific detectivity of ~10^9 $cmHz^{1/2}/W$ at room temperature and were coupled with the LED emitting at 3.3 μm.

Table of Contents

List of Figures vii

List of Tables xv

Acknowledgements xvi

Publications xvii

Chapter 1 Introduction 1

Chapter 2 Light Emitting Diodes 3

2.1 Introduction 3

2.2 Fundamentals 6

2.2.1 Basics of LED operation 6

2.2.2 LED performance parameters 10

2.3 Material survey 15

2.4 Fabrication and characterization 19

2.4.1 Fabrication 19

2.4.2 Characterization 21

2.5 Experimental results and discussion 26

2.5.1 Type I QW bipolar cascade LEDs at 2 μm 27

2.5.2 Type I QW LEDs at 3.0 μm ~ 3.7 μm 31

2.5.3 Double heterostructure LEDs at 3.7 μm ~ 4.0 μm 37

2.5.4 Type II superlattice LEDs at 4 μm ~ 10 μm 41

2.5.5 High dimensional addressable LED arrays 50

2.5.6 Dual wavelength LEDs and LED arrays 55

2.5.7 Light extraction 61

2.6 Conclusion and future work 67

Chapter 3 Semiconductor lasers 69

3.1 Introduction 69
3.2 GaSb based single spatial mode lasers at 2.0 μm ~ 2.2 μm 72
3.2.1 Waveguide design 72
3.2.2 Selective wet etching 73
3.2.3 Laser heterostructure growth and fabrication 75
3.2.4 Laser characteristics 79
3.3 Optically tunable quantum cascade lasers 92
3.4 Conclusion and future work 99
Chapter 4 Photodetectors 101
4.1 Introduction 101
4.2 Figures of merits 101
4.2.1 Quantum efficiency and responsivity 101
4.2.2 Noise equivalent power 102
4.2.3 Detectivity 103
4.3 Characterization 104
4.4 Results and discussion 109
4.4.1 Introduction 109
4.4.2 Design, growth and fabrication 109
4.4.3 nBn vs. nBp detector 113
4.4.4 Front- and back-illumination 118
4.4.5 LED-Detector optopair 122
4.5 Conclusion and future work 124
References 126
Appendix 1 134

List of Figures

2.1 The radiant exitance of MIR LEDs as a function of peak wavelength obtained from several groups. Data is taken from LEDs operating at room temperautre. The crosshatched region indicates the corresponding to radiant exitance of a blackbody at 1000 K.. 6

2.2 a) homojunction diode in thermal equilibrium (left) and forward bias (right), b) double heterostructure at forward bias, c) QW structure at forward bias. 7

2.3 The types of the band alignments; Type I and Type II. 9

2.4 The recombination processes. 11

2.5 The cross section of the surface emitting LED. 12

2.6 The calculated free carrier absorption coefficient as a function of wavelength with the different doping concentrations of n-type GaSb. 13

2.7 The bandgap of III-V semiconductor materials. Band parameters were taken from [30]. The horizontal dashed lines indicate the MIR spectral range. The crosshatched region indicates the bandgap energy of GaSb/InAs superlattice. 15

2.8 Bandgap energy of AlGaAsSb and GaInAsSb lattice matched to GaSb as a function of the Ga content, estimated at T=300 K. The gray region visualizes the GaInAsSb bandgap. The VBO bowing for both alloys is neglected. 17

2.9 Band offsets (top) of GaInAsSb alloy against to $Al_{0.85}GaAsSb$ (solid) and $Al_{0.30}GaAsSb$ (dash) as a function of the Ga content. Wavelength of GaInAsSb alloy as a function of the Ga content is shown on the bottom. The arrows indicate the Ga content of GaInAsSb near the zero valence band offset with $Al_{0.85}GaAsSb$ and $Al_{0.3}GaAsSb$. 17

2.10 Calculated miniband energy of type II GaSb/InAs superlattice as a function of the InAs width at the fixed GaSb width of 20 Å at 80 K. The model used for this calculation can be found in [37, 38]. The wavelength was estimated at the minimum of the conduction band C1 and the maximum of the heavy hole band HH1. 18

2.11 The fabrication flow chart (left) and illustration (right) corresponding to the step indicated..... 21

2.12 The measurement system of LED optical power 22

2.13 The experimental setup for the calibration. 1–preamplifier, 2–detector, 3–integrating sphere, 4–blackbody thermal shield, 5–modulator, 6–blackbody cavity. 23

2.14 Electroluminescence of a LED and its Gaussian model. 24

2.15 The scheme for calculation of total power entering the thermal shield aperture. 24

2.16 The estimated coefficient, K as a function of wavelength (solid) and the normalized InSb detector sensitivity (dashed). 25

2.17 Optical power as a function of current obtained from a commercial LED: open sympbol-specificaiton values, closed symbol-measured values. 26

2.18 Bandstructure of the type I QW active region for λ~2 μm. 27

2.19 Normalized electroluminescence of the 1-stage and 2-stage LED measured from 20 ˚C to 50 ˚C with a 5 ˚C step under pulse mode (100 kHz, 5%). 28

2.20 Light- Current-Voltage of the 1-stage and 2-stage LED measured at 20 ˚C under qCW mode (3 kHz, 50%) 29

2.21 Temperature dependence of optical power of the 2-stage LED biased under qCW mode (3 kHz, 50%). The inset shows the characteristic temperature, T_1 of 70 K estimated at I=0.77 A. 30

2.22 The IR image of a working LED at room temperature (left) and schematic bandstructure with the quinternary AlInGaAsSb barrier (right). 31

2.23 Electroluminescence of each device at T=300 K. 32

2.24 Current-Voltage dependence of device 2 at T=300 K and T=80 K. 33

2.25 The dependence of light power on bias current for the devices with quaternary and quinternary barriers under qCW (3 kHz, 50%) mode at 300 K. 34

2.26 The internal efficiency of each device under qCW (3 kHz, 50%) mode at 300 K.. 34

2.27 The dependence of light power on bias current, measured under qCW (3 kHz, 50%) mode from device with the quinternary barrier emitting at 3.15 μm (device 2) 35

2.28 LED spectra at different temperatures. 36

2.29 The dependences of the output power vs. bias current for non-addressable 3×3 LED array at different temperatures and the current-voltage dependence at room temperature. 36

2.30 The calculated bandgap energy and band offsets of AlGaAsSb and GaInAsSb materials lattice matched to GaSb at 300 K 37

2.31 Electroluminescence of the QW LED300 (a), DH LED487 with In 50% (b), and DH LED 488 with In 54% (c), measured at 15 K and from 25 K to 300 K with a 25 K step at fixed CW current of 100 mA. 38

2.32 The peak wavelength (a) and FWHM (b) as a function of temperature: square – QW LED300, circle – DH LED487 with In 50%, and triangle – DH LED488 with In 54%. 39

2.33 Optical power and the internal efficiency as a function of current for λ=3.75 μm LED (square) and for λ=4.05 μm LED (circle) at room temperature under qCW mode (3 kHz, 50%)..... 40

2.34 L-I-V of QW LED300, DH LED487, and DH LED488 at room temperature (a) and 80 K (b) under qCW (3 kHz, 50%) mode. 41

2.35 The IR image of Bulk (a) and SL (b) LED at RT under 100 mA and electroluminescence of Bulk (left) and SL (right) LED, measured from 77 K to 300 K under 10 mA CW current (c)..... 42

2.36 Electroluminescence as a function of current for DH LED (a) and SL LED (b) measured at room temperature under CW bias current. Current range is from 10 mA to 50 mA with 10 mA step and from 100 mA to 600 mA with 100 mA step. 43

2.37 Optical power of the InGaAsSb bulk (left) and SL (right) LED as a function of current under qCW (3 kHz, 50%) mode with different temperatures. 44

2.38 The characteristic temperature T_1 at different bias currents for DH and SL LED. 45

2.39 The optical modulation frequency response for each LED at RT. The minority lifetime for the bulk (τ_{Bulk}~65 ns) and SL (τ_{SL}~65 ns) LED was obtained by fitting the measured graph (solid) with the transfer function (dot) from [50]. 45

2.40 Schematic band diagram of LED 1, 3, and 4. Only bandgap energy of the SL is shown..... 47

2.41 Electroluminescence of all LEDs measured at 77 K under qCW (10 kHz, 50%) mode..... 48

2.42 Electroluminescence of all LEDs measured at 870 mA and relative optical power..... 49

2.43 Schemes and MIR images of non-addressable (a) and addressable (b) LED arrays. 51

2.44 Read-in circuit for the prototype 6×6 array (a); MIR images of the operating 6×6 array without bias (b) and under total bias current of 54 mA (c)..... 52

2.45 The radiant exitance measured on 9 pixels of the 6×6 array as a function of current density under qCW (3 kHz, 50%) mode at room temperature for 3.66 μm LED. 53

2.46 The pixel layout for the 512×512 LED array..... 54

2.47 Fragment of 512×512 array after groove etching (a) and pixel mesa walls (b)..... 54

2.48 Completed 512×512 addressable LED array at several different magnifications. Both anode and cathode contacts are on the top of each mesa. 55

2.49 Current versus voltage characteristic (a) and emission spectrum (b) of a 512×512 array pixel. The inset of the right panel is the MIR image of a working array pixel. 55

2.50 The band diagram of the dual wavelength LED and (b) EL spectra. 56

2.51 (a) The structure of the dual wavelength LED. (b) The completed dual wavelength LED device. Infrared images for (c) the top LED ($\lambda = 3$ μm) and (d) bottom LED ($\lambda = 2$ μm). . 57

2.52 LIV characteristic for the dual wavelength LED. Closed and half closed symbol for the optical power versus current under qCW (3 kHz, 50%) and pulsed (3 kHz, 1%) mode operation, respectively. Open symbol for the voltage versus current. 59

2.53 (a) Scheme of dual wavelength LED arrays and (b) EL spectra of 2 μm and 3.4 μm LED pixels with infrared images. 60

2.54 Normalized near-field intensity and IR image of the uncoated (a, b) and coated LED (c, d) measured at room temperature under CW current of 20 mA. 62

2.55 Optical power of the uncoated (line) and coated (symbol) under qCW mode (3 kHz, 50%) at room temperature. 63

2.56 Normalized electroluminescence of the uncoated and coated LED. 63

2.57 The micrographs of surface patterned LEDs with 5 min etching (a) and 10 min etching (b); top- side view; middle and bottom- top view with different magnifications. 64

2.58 The IR images of non-etched (a), etched 5 min (b), and etched 10 min (c) LED under 10 mA (top) and 50 mA (bottom) CW current. 65

2.59 Optical power vs. current for non-etched (triangle), 5 min etched (circle), and 10 min etched (square) LED measured at room temperature under qCW mode. 66

2.60 Measured (solid) and calculated (dashed) far field of the etched 10 min etched LED under qCW mode at room temperature. Far-field of the non-etched LED is identical to the one etched (not shown). 66

2.61 The radiant exitance of the MIR LEDs as a function of peak wavelength obtained from several groups. The crosshatched region indicates the corresponding to radiant exitance of a blackbody at 1000 K. The data only present results obtained at room temperautre. Closed symbols indicate qCW or CW mode and open symbols indicate pulse mode. 68

3.1 The schematic band diagram of the type I QW laser and associated refractive indexes with optical field. 70

3.2 The cross-section of a generic ridge waveguide laser. 73

3.3 The refractive index difference and the maximum ridge width for single mode operation as a function of the lower p-cladding thickness. 73

3.4 The cross-section of the test sample representing the p-side of the laser structure. The etched surface is the $Al_{0.2}In_{0.25}GaAs_{0.235}Sb$ etch stop layer. The uniformly etched surface is comparable with the non-etched GaSb surface. The projection near the sidewall is aluminum oxide..... 74

3.5 The cross-section of the lasers with (a) or without (b) an etch stop layer. 75

3.6 Laser heterostructure with the AlInGaAsSb etch stopper (wafer 1: λ=2.0 μm) and without the etch stopper (wafer 2: λ=2.0 μm, wafer 3: λ=2.2 μm)..... 76

3.7 Fabrication procedure using the selective wet etching technique in clockwise order..... 77

3.8 SEM images of the completed narrow ridge lasers: (a) from the wafer 1, (b) from the wafer 2, (c) from the wafer 3. 78

3.9 L-I-V of the 6-μm-wide NR (solid) and 90-μm-wide BA (dash) laser under pulsed current at 20˚C. Inset shows the emission wavelength of the laser. The cavity length for both lasers is 1 mm..... 79

3.10 CW room temperature power and voltage of the 4.5-μm-wide (dash) and 6-μm-wide (solid) 2-mm-long AR/HR (5%/95%) coated NR lasers..... 80

3.11 Far field divergence of the 6-μm-wide NR (solid) and 90-μm-wide BA (dash) laser along the slow axis. Both lasers are measured under pulsed (10 kHz, 7 μs) current at 20 ˚C. The arrows indicate the presence of the first mode at 400 mA..... 81

3.12 Modal gain spectra of the 1-mm-long 6-μm-wide NR (a) and 90-μm-wide BA (b) laser measured with 1 MHz, 200 ns at 20 ˚C. The current applied below threshold is indicated for each curve..... 81

3.13 The peak modal gain vs. current (a) and current density (b) of the 6-μm-wide NR (square) and 90-μm-wide BA (circle) laser. 82

3.14 Peak power density (power per unit width per facet) vs. current density of the λ = 2.2 μm 6-μm-wide (solid) and 100-μm-wide (dashed) lasers with 1-mm-long uncoated cavities under pulse mode (100 kHz, 200 ns) at 20 ˚C. Three 6-μm-wide lasers from the same heterostructure wafer are plotted to show their uniformity. The inset is the measured far field divergence of each laser along the slow axis at the given current. The solid line in the far field of the 6-μm-wide laser is the Gaussian fitting. 83

3.15 Current dependence of the lateral beam waist intensity patterns measured at 20 ˚C under pulsed (5 – 30 kHz, 200 ns) current for the 1-mm-long uncoated 6-μm-wide λ = 2.2 μm lasers (a) and 3.5-μm-wide λ = 2.0 μm lasers (b). 84

3.16 L-I-V of the 2-mm-long coated (AR/HR = 5%/95%) narrow ridge lasers under pulse mode (solid line, 100 kHz, 200 ns) and CW mode (symbol) at 20 ˚C. The inset is the wavelength of each laser measured at 100 mA. 85

3.17 The far field divergence (symbols) along the slow axis for all narrow ridge lasers as a function of pulsed bias current (100 kHz, 200 ns) from 100 mA to 300 mA at 20 ˚C. The solid lines are the Gaussian fittings. 86

3.18 The refractive index difference and the corresponding maximum width of the ridge to support only the fundamental mode as a function of the bottom p-cladding thickness. The vertical arrows indicate the ridge widths discussed in this work (dashed - for λ = 2.0 μm and solid - for λ = 2.2 μm lasers). 87

3.19 The lateral near field pattern at beam waist (circle) at I = 50 mA of the 1-mm-long uncoated 6-μm-wide λ = 2.2 μm lasers measured under pulse mode (100 kHz, 200 ns) at 20 ˚C. The solid lines are the calculated near fields for the guided modes. The vertical dashed lines indicate the ridge width. 88

3.20 Modal gain spectra of 1-mm-long uncoated lasers measured in pulsed regime (1 MHz, 200 ns) at 20 ˚C: (a) the 100-μm-wide λ = 2.2 μm laser, (b) the 6-μm-wide λ = 2.2 μm laser, (c) the 3.5-μm-wide λ = 2.0 μm laser..... 90

3.21 The peak modal gain as a function of current density for all lasers. 91

3.22 (a) The layout of QCL waveguide layer sequence layout. (b) The schematic of the experimental setup. 93

3.23 (a) Optical pumping geometry used in our experiments. (b) Bandgaps of the semiconductor materials used in our device compared to the optical pumping photon energy. (c) The image of the device facet. (d) The image of the 250 μm window at the backside of our devices for optical pumping. 94

3.24 (a) Zoom-in of the quantum cascade laser emission spectrum under different optical pumping intensities. A frequency shift of a single longitudinal mode is clearly seen. Inset: emission spectrum of the device. (b) Spectral position of a longitudinal mode in the QCL emission spectrum (left axis) and QCL power output (right axis) as a function of optical pump intensity. 95

3.25 (a) Spectral position of the laser mode and the power output from our device as a function of the delay of the optical pumping pulse with respect to the QCL bias pulse. (b) Light output-current (L-I) and current-voltage (I-V) characteristics of the tested device for different optical pumping intensities. 97

3.26 (a) TM_{00} waveguide mode and waveguide refractive index profiles in our devices. (b) Dependence of the threshold current density in our devices on the reciprocal cavity length. The value of waveguide loss of $\alpha 0I$ ~12.2 cm^{-1} is obtained assuming $J_{th}(1/L) \propto \alpha_{tot} = ln(R_m)/L + \alpha_{0i}$, where R_m~0.28 is the uncoated facet reflectivity and L is the laser cavity length. 98

3.27 GaSb based type I QW laser fabricated by the selective wet etching with 3.5 μm of the ridge width. Far field was measured at room temperuature under pulse (10 kHz, 7 μs) current of 300 mA. 99

4.1 Calculated BLIP specific detectivity as a function of the peak wavelength at different background temperatures. 104

4.2 Related parameters for characterization of the specific detectivity. 105

4.3 (a) The system diagram of the responsivity measurement, (b) configuration of the detector and blackbody. 106

4.4 The equivalent circuit of the photocurrent measurement system without the preamplifier..... 107

4.5 The equivalent circuit of the photocurrent measurement system with the preamplifier.... 108

4.6 Photocurrent as a function of the reverse bias voltage, measured with or without the preamplifier. 108

4.7 Calculated band diagram of the nBn (a) and nBp (a) detector. The horizontal dashed line indicates the Fermi level. 110

4.8 Device geometry for the front-illumination (left) and back-illuminated (right) scheme. D is the diameter of the top aperture or back contact varied from 350 μm to 80 μm. 112

4.9 Room temperature current density vs. voltage characteristics for the etched and non-etched photodetector 113

4.10 Calibration of the photoresponse signal obtained by using a glow bar as a light source. The effective temperature of 1200 ˚C of the glow bar is estimated using the InSb detector and blackbody radiator. 114

4.11 Photo-response of the nBp (a) and nBn (b) detector measured at various temperatures. V_{bias}=0 V for both detectors. 115

4.12 The cut off wavelength and relative responsivity at zero bias as a function of temperature. Top x-axis is the thermal energy corresponding to the bottom x-axis. Square is for the nBn and circle is for the nBp. 116

4.13 Dark current density measured at different temperatures for the nBn (a) and nBp (b) detector..... 117

4.14 Dark current density as a function of 1/kT for the nBn (circle) and nBp (square) detector. The similar activation energy of 488 meV is obtained from both detectors. 117

4.15 The responsivity of the nBn and nBp detector measured at room temperature with a Blackbody emitting at 700 ˚C. The aperture diameter is 150 μm for both detectors. 118

4.16 Normalized room temperature photoresponse from the front- and back-illuminated detector..... 119

4.17 Absorption coefficients of InAs with different doping concentrations. 120

4.18 The peak responsivity and specific detectivity at 3.3 μm measured at room temperature using a blackbody operating at 700 ˚C and the chopper modulating at 500 Hz. Square: front-illumination; circle: back-illumination. 121

4.19 The responsivity dependence on optical area of the front- (square) and back- (circle) illuminated detectors measured at room temperature. Closed square is the peak responsivity obtained at λ=2.4 μm and open one is the peak responsivity at 3.3 μm. The bias voltage was -0.2 V..... 122

4.20 Normalized LED electroluminescence, detector photoresponse, and methane absorption spectrum. 123

List of Tables

2-1 The list of devices for comparison between quaternary and quinternary barrier LEDs. 32

2-2 The list of superlattice active regions to investigate hole transport. 46

3-1 Etching rate of the tartrate etchant and HCl etchant 75

4-1 Heterostructures of the nBn and nBp detector [30, 106]. 111

4-2 Material parameters used for the band structure simulation [107]. 111

4-3 The nBp detector samples for the absorption coefficient measurement. 120

Acknowledgements

None of this work would have been done without my colleagues in Optoelectronics Group. I would like to express my sincere appreciation to my advisors Prof. Sergey Suchalkin and Prof. Gregory Belenky for their invaluable discussions, continuous encouragement, and financial support. I also thank to Prof. Leon Shterengas, Prof. Dmitry Donetsky, Dr. Gela Kipshidze, and Prof. David Westerfeld for fruitful discussions and collaborations. It was also great pleasure for me to work with my fellow members Dr. Takashi Hosoda, Dr. Jianfeng Chen, Ding Wang, Rui Liang, and Youxi Lin. I must gratefully thank my parents and my wife, Jieun for their support and patience.

Publications

Journals:

1. S. Suchalkin, S. Jung, R. Tober, M. Belkin, and G. Belenky, "Optically Tunable Room Temperature Operated λ=9 μm Quantum Cascade Laser," *Appl. Phys. Lett.*, (2012) (Accepted)

2. D. Wang, D. Donetsky, S. Jung, and G. Belenky, "Carrier Lifetime Measurements in Long-Wave Infrared InAs/GaSb Superlattices Under Low Excitation Conditions," *J. Electron. Mater.*, 41, 3027 (2012)

3. S. Jung, R. Liang, G. Kipshidze, S. Suchalkin, L. Shterengas, and G. Belenky, "Single Spatial Mode 2 – 2.2 μm Diode Lasers Fabricated by Selective Wet Etching," *Semicond. Sci. Technol*., 27, 085004 (2012)

4. S. Jung, G. Kipshidze, R. Liang, S. Suchalkin, L. Shterengas, and G. Belenky, "GaSb Based Mid Infrared Single Lateral Mode Lasers Fabricated by Selective Wet Etching Technique with an Etch Stop Layer," *J. Electron. Mater.*, 41, 899 (2012)

5. S. Jung, S. Suchalkin, D. Westerfeld, G. Kipshidze, E. Golden, D. Snyder, and G. Belenky, "High Dimensional Addressable LED Arrays Based on Type I GaInAsSb Quantum Wells with Quinternary AlGaInAsSb Barriers," *Semicond. Sci. Technol*., 26, 085022 (2011)

6. S. Jung, S. Suchalkin, G. Kipshidze, D. Westerfeld, E. Golden, D. Snyder, and G. Belenky, "Dual Wavelength GaSb Based Type I Quantum Well Mid Infrared Light Emitting Diodes," *Appl. Phys. Lett.*, 96, 191102 (2010)

7. S. Jung, S. Suchalkin, G. Kipshidze, D. Westerfeld, D. Snyder, M. Johnson, and G. Belenky, "GaSb Based Type I Quantum Well Light Emitting Diode Addressable Array Operated at Wavelengths Up to 3.66 μm," *IEEE Photon. Technol. Lett.*, 21, 1087 (2009)

8. S. Suchalkin, S. Jung, G. Kipshidze, L. Shterengas, T. Hosoda, D. Westerfeld, D. Snyder, and G. Belenky, "GaSb Based Light Emitting Diodes with Strained InGaAsSb Type I Quantum Well Active Regions," *Appl. Phys. Lett.*, 93, 081107 (2008)

Conference Presentations:

1. L. Shterengas, G. Kipshidze, T. Hosoda, R. Liang, S. Jung and G. Belenky, "Diode Lasers Operating in Spectral Region from 1.9 to 3.5 μm," *IEEE International Semiconductor Laser Conference (ISLC)*, San Diego, CA, Oct. 7-10 (2012)

2. S. Suchalkin, M. Jang, S. Jung, R. Tober, M. Belkin, and G. Belenky, "Fast Electrical Wavelength Modulation of Mid-infrared Quantum Cascade Lasers," *Conference on Lasers and Electro-Optics (CLEO)*, San Jose, CA, May 7-11 (2012)

3. S. Jung, S. Suchalkin, D. Wang, D. Donetsky, M. Jang, R. Tober, M. Belkin, and G. Belenky, "Optical Control over the Effective Refractive Index of Quantum Cascade Laser Modes," *CoS3 Workshop*, Princeton, Apr. 13 (2012)

4. S. Jung, S. Suchalkin, G. Kipshidze, L. Shterengas, and G. Belenky, "Wet Etching Technique for Fabrication of GaSb Based Mid Infrared Single Lateral Mode Lasers," *Electronic Materials Conference*, Santa Barbara, CA, Jun. 22-24 (2011)

5. S. Jung, S. Suchalkin, G. Kipshidze, and G. Belenky, "GaSb Based Mid-Infrared Type I Quantum Well Dual Wavelength LEDs and LED Arrays," *MIRTHE-IROn-SensorCAT Virtual Conference*, Jan. 19-20 (2011)

6. S. Suchalkin, D. Westerfeld, S. Jung, G. Kipshidze, L. Shterengas, T. Hosoda, and G. Belenky, "Room Temperature Operated GaSb Based Type I Light Emitting Diodes," *SPIE Defense and Security*, Orlando, FL, Mar. 17-18 (2008)

Chapter 1

Introduction

An object with above zero temperature emits electromagnetic radiation, i.e. light. Such light emission (or detection) in semiconductor optoelectronic devices is the result of the energy conversion process. In the sense, development of semiconductor optoelectronic devices is aimed to maximize the conversion efficiency at desired wavelengths.

With respect to the frequency range of the electromagnetic radiation, mid infrared (MIR) is defined, but loosely, as the spectral region covering from 2 μm to 14 μm. The uniqueness of this region is the presence of absorption fingerprints of various molecules that are essentially manifested by their vibrational motions. Distribution of fundamental bonds including C-H and O-H in MIR region allows detection and even imitation of their presence, by matching spectral sensitivity of detectors and emitters to those molecules. One can realize many useful applications such as hazardous gas detection, environmental monitoring, process control, medical diagnosis and treatment, infrared imaging, etc. Another unique feature in MIR range is an atmospheric window at 3–5 μm and 8–14 μm that are often called the first and second MIR window, respectively, where free-space communication can be achieved.

Spontaneous emission, stimulated emission, and absorption in semiconductors are fundamental optical processes for light emitting diodes, lasers, and photodetectors, respectively. Predominant advantages of them over the non-semiconductor devices could be high efficiency, high radiance (or sensitivity), and fast response as well as compact size. The first stimulated emission from III-V compound semiconductors was observed by Hall *et al*. [1] and Nathan *et al*. [2], in 1962 by using the forward biased GaAs pn-junctions at liquid nitrogen temperature. In the same year, the first visible LED emitting orange color from GaAs was demonstrated by Holonyak and colleagues [3]. The photodetectors using compound semiconductors were demonstrated by Lawson *et al*. [4] by using mixture of cadmium telluride (CdTe) semiconductor and mercury telluride (HgTe) semimetal, so called MCT (HeCdTe) whose bandgap can be tuned from 0 eV to 1.5 eV.

This thesis presents the experimental results on LEDs, lasers and photodetectors. We shall use this opportunity of diverse researches to learn seemingly slight but critical difference in development strategies for each type of device. Firstly, we will explore how we can exploit the bandstructure engineering to design efficient LEDs, which will provide the property of the radiative recombination process in GaSb based material systems. Secondly, the lasers utilizing photon feedback mechanism will be demonstrated in realization of diffraction limited beam and wavelength tuning, based on the analysis of optical field, optical gain, and the effective refractive index of a lasing mode. Lastly, photodetectors using nBn [5] and nBp active region will be demonstrated to form the LED and detector opto-pair that is necessary for chemical sensing applications.

Chapter 2

Light Emitting Diodes

2.1 Introduction

High radiance, short switching time, emission spectrum tailoring, long-term reliability, and low cost as well as inherent surface emission are the key advantages of the MIR-IR LEDs, which are well suited for applications such as gas detection, medical diagnosis, and infrared scene projection (IRSP). Those applications, in fact, can be also realized using lasers that can provide higher sensitivity in gas detection, better focusability and intensity for medical treatment, and higher apparent temperature in IRSP, but with less tolerant in temperature and incomparably higher cost than the LEDs. Other competing devices, on the other side of the cost grounds, are tungsten filament lamps and electro-chemical sensors [6]. The glass envelope of the lamp, however, limits cut off wavelength near 4 μm and it shows very low spectral efficiency due to 99% emission into out of spectral interest as well as sufficiently slow switching speed, which is not acceptable for the scene projection. The electro-chemical sensor that monitors electrical change due to interaction between target gas and chemical surface suffers from chemical contamination and unreliable operation. Thus, exclusive benefits of LEDs to others are essentially inherent surface emission that allows relative ease of monolithic integration to form arrays, cost competitiveness that is suitable for high volume low sensitive gas sensors, and reliable operation with high spectral efficiency.

Many parameters that describe the performance of LEDs, such as the optical power density, external quantum efficiency, and conversion efficiency, can be affected by the geometrical or structural factors of LEDs, which often makes reasonable comparison between LEDs difficult. Thus, we will use the apparent temperature defined as the temperature of a blackbody emitting the same optical power density (radiant exitance) within the spectral range of a LED, which is especially meaningful for IR LEDs as a means to replace incandescent sources. The apparent temperature can be calculated using,

$$\frac{P_{LED}}{S_{LED}} = \int_{\lambda_{min}}^{\lambda_{max}} R(\lambda, T_A) d\lambda \qquad 2\text{-}1$$

, where P_{LED} is the total optical power emitted by a LED, S_{LED} is the LED emitting area, $R(\lambda, T_A)$ is the spectral radiant exitance of a blackbody at the temperature of T_A, and λ_{min} and λ_{max} are corresponding to wavelengths at the half peak intensity of a LED spectrum.

Various approaches have been made to realize efficient MIR LEDs by several groups. LEDs based on the InAs material systems were mostly demonstrated by Yakovlev and Matveev group of Ioffe Univesity in Russia and Krier group of Lancater University in UK. Yakovlev group has demonstrated LEDs using the $InAs_xSb_{1-x}$/InAsSbP materials system grown on InAs substrates by using a metal organic vapor phase epitaxy (MOVPE) system [7-10]. The wavelength of LEDs was controlled by decreasing As content in InAsSb from 100% to 84.3% with the wavelength control range of 3.45 μm to 4.5 μm, respectively. Pulsed powers of LEDs decreased from 1.2 mW to 0.1 mW as the wavelength increased. That was attributed to worse material quality as As increased due to increased lattice mismatch as well as enhanced Auger recombination rate in small bandgaps, resulting in one order of magnitude decrease of output power for the long wavelength device. Matveev group in Ioffe University has demonstrated InAs based LEDs grown by a liquid phase epitaxy (LPE) system [11-15]. Using the $InAs_xSb_{1-x}$ active region with InAsSbP barrier layers, they demonstrated LEDs emitting near 3.3 μm – 4.2 μm with optical power of 20 μW – 40 μW at room temperature. A LED was driven to temperature of 180 ˚C [15] but with stable operation, proving that the capability of high temperature stability and reliability of LEDs, together with negative luminescence that can imitate a cold object by extracting carriers under reverse bias so that total carrier density in an active region becomes smaller than the intrinsic carrier density. Krier group demonstrated high quality LPE grown InAs based LED structures, which was realized using rare earth (Yb) gettering to decrease residual carrier concentration in the active region [16-20]. The LEDs with the InAs/InAsSbP active region emitting at 3.3 μm have generated pulse power more than 3.5 mW as well as qCW power as high as 170 μW at room temperature. Recently, the InSb quantum dot active region was introduced to overcome lattice mismatch between InSb and InAs, and qCW optical power of 6 μW at 3.8 μm was reported.

The molecular beam epitaxy (MBE) grown InAs/InAsSb superlattice (SL) and InAs/$Ga_{0.75}$InSb /$Al_{0.15}GaAs_{0.05}$ W-QW active region LEDs were demonstrated by Phillips group of Imperial College in UK. The SL LEDs emitting at 4.2 μm and the W-QW LEDs emitting at 3.3 μm produced 100 μW and 55 μW under pulse mode at room temperature, respectively [21, 22]. Recently, Prineas of Iowa University in US demonstrated GaSb/InAs type II SL LEDs using the active region cascading scheme. Apparent temperatures of 1430 K for 3.85 μm [23, 24] and 1400 K for 8.6 μm [25] have been obtained from the LEDs operating under qCW mode at 77 K.

Figure 2.1 shows the radiant exitance of LEDs as a function of peak wavelength. Data, obtained from the literatures published between year 1994 and 2010, only present the LEDs measured at room temperature and treated with no modification to improve the extraction efficiency. The emitting area was inferred from the context if those literatures did not specify it. The solid and open symbols indicate the qCW (50% duty cycle) or CW and pulse mode, respectively. The crosshatched region displays the radiant exitance corresponding to that of a blackbody at 1000 K within the spectral range of LED FWHM that is assumed 10% – 15% of the peak wavelength. As one can see, there are no LEDs emitting more light than 1000 K blackbody under qCW or CW mode at room temperature.

The goal of MIR LED development in our group is to demonstrate MIR LEDs generating continuous wave apparent temperature more than 1000 K at room temperature or CW optical power as close as 1 mW. Prevalent issues in development of long wavelength LEDs include: 1) increase of the non-radiative Auger recombination rate, 2) increase of free carrier absorption at long wavelength, 3) shallow hole confinement due to insufficient valence band offset, 4) carrier imbalance due to large difference between the electron and hole effective mass, and 5) the small light extraction efficiency that is the fundamental issue in LEDs of any wavelength. Strategies to overcome each of them will be discussed in Section 2.3.

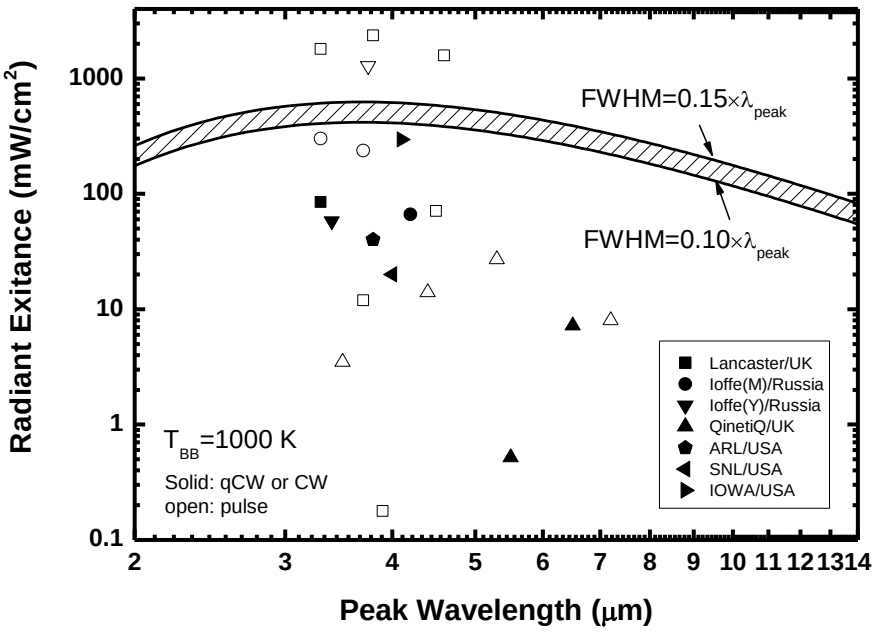

Figure 2.1 The radiant exitance of MIR LEDs as a function of peak wavelength obtained from several groups. Data is taken from LEDs operating at room temperautre. The crosshatched region indicates the corresponding to radiant exitance of a blackbody at 1000 K.

2.2 Fundamentals

2.2.1 Basics of LED operation

The LEDs are composed of p-n diodes. If a semiconductor is not doped with any other materials, it is called an intrinsic semiconductor. By adding impurities, the intrinsic semiconductor will be an electron dominant (n-type) or hole dominant (p-type) semiconductor. Depending on whether an impurity atom is providing electrons or holes, the impurity atom is called a donor or acceptor atom, respectively. In the III-V material system, for example, beryllium (Be) from group II and tellurium (Te) from group VI can be an acceptor and donor element, respectively.

Figure 2.2(a) shows the band diagram of a homojunction diode that is consisted of the same bandgap materials with the different type of conductivity. Thermal equilibrium indicates that the diode is under condition of no external forces such as electric field so that, in thermal equilibrium condition, the Fermi level (E_F) is a constant throughout a system.

When the p- and n-type semiconductor are brought into a junction, majority carriers of each side will diffuse into the other side due to the difference of carrier densities. This will create a charged region, called space charge region, at the pn junction interface. The charged region, originated from the donor impurities, will create an internal electric field that is applied to the opposite direction of the diffusion force. Since the diffusion and electric field force are balanced to be the same at the equilibrium condition, net current in the diode will be zero.

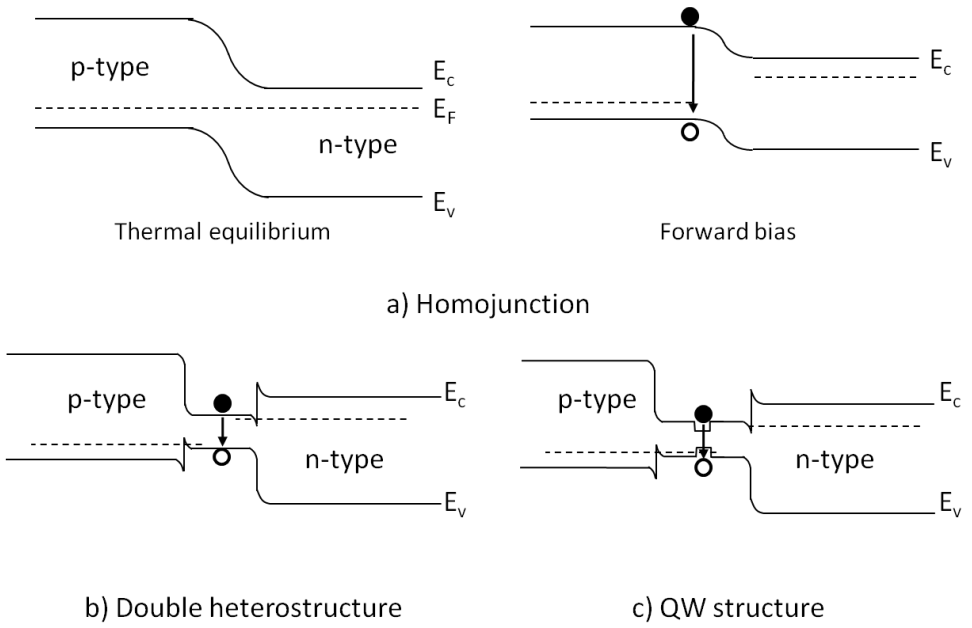

Figure 2.2 a) homojunction diode in thermal equilibrium (left) and forward bias (right), b) double heterostructure at forward bias, c) QW structure at forward bias.

When an external bias is applied to the opposite direction of the internal electric field (forward bias), electrons and holes diffuse into the space charge region where they become the excess minority carriers[§]. When the excess minority carriers diffuse into the neutral region, they will recombine with the majority carriers. If the recombination is a band to band radiative recombination process, photons will be generated. Thus, as shown in Figure 2.2(a; right), the homojunction diode will have a large recombination area due to the absence of carrier confinement layers.

[§] Under non-equilibrium condition, electrons from n-type and holes from p-type semiconductor will be injected to the pn diode. If the injected carriers are transferred to different type of region, they will become minority carriers. For example, when electrons from n-type move to p-type, those electrons are called minority carrier in p-type semiconductor.

Most of modern optical devices are formed as double heterostructures (DHs) or QW structures (Figure 2.2(b, c)). When two different semiconductor materials are brought into a junction, it is called the heterojunction. The crystalline order of the heterostructure is preserved throughout the whole growth of layers so that heterostructures can be considered as a single crystal. The superiority of DH or QW active regions over the pn homojunction is carrier confinement realized by separating the active region from injection layers using high bandgap materials. As shown in Figure 2.2(b), the cladding layers in DH prevent carriers from leaking out of the active region, resulting in more effective photon generation than that of the homojunction structure.

The QW active region is consisted of a thin layer (below a few tens of nanometers) enclosed by confinement layers called barrier layers. The density of states and allowed energy levels in the QW are quantized and controlled by the thickness of the QW and barrier layers. The thin active region provides several advantages over the DH: wavelength controllability and application of strain engineering. The wavelength of the DH is determined by the bandgap energy of the active region while that of the QW can be varied by the thickness and strain of the QW layer to some extent. The strain energy, due to the lattice mismatch between two layers, can be accommodated up to a certain thickness called a critical thickness. Otherwise, the excess strain energy will be released in the form of dislocations. If a lattice-mismatched layer is grown within the critical thickness, the strain can change the physical properties of the QW layer such as the effective mass of hole in valence band. It is called the strained QW. The strain (ε) is defined as,

$$\varepsilon = \frac{a_0 - a_1}{a_0} \qquad 2\text{-}2$$

, where a_0 is the lattice constant of the substrate and a_1 is the lattice constant of the grown layer. When ε is minus (plus) sign, it is called the compressive (tensile) strain.

The effect of the strain on the QW band structure is different depending on either the compressive or the tensile strain. The lattice deformation induced by the strain will change both hydrostatic and shear component of the strain. Since the bandgap energy is the function of the hydrostatic and shear component (changing distance between atoms results in modification of binding energy), conduction (C.B.) and valence band (V.B.) will be shifted by the hydrostatic component while heavy hole (HH) and light hole (LH) band will experience relative shift caused

by the shear component. Consequently, the change of the band structure will result in the change of the wavelength. In addition, the effective mass[**] of V. B. will be reduced by the strain, which will reduce the density of states in V.B. This is especially beneficial for laser diodes to decrease the threshold current.

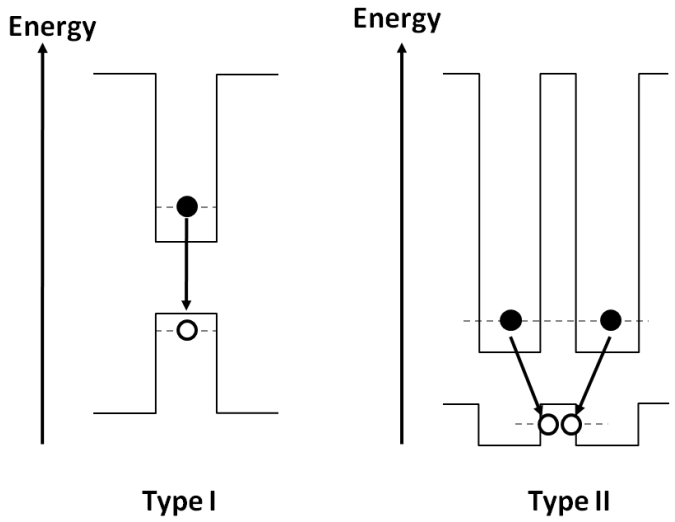

Figure 2.3 The types of the band alignments; Type I and Type II.

There are several types of band alignments at the QW interface as shown in Figure 2.3. The nature of type I and II can be distinguished by band offsets. Band offset (ΔE) is the discontinuities in energy of the conduction band (conduction band offset (CBO): ΔE_C) and valence band (valence band offset (VBO): ΔE_V) at the heterojunction interface, which can be expressed as,

$$\Delta E_C = E_{C1} - E_{C2} \quad 2\text{-}3$$

$$\Delta E_V = E_{V1} - E_{V2} \quad 2\text{-}4$$

, where E_{C1} and E_{V1} are the conduction and valence band of material 1, and E_{C2} and E_{V2} are the conduction and valence band of material 2. Type I is characterized by different signs of ΔE_C and ΔE_V, while in type II structure ΔE_C and ΔE_V have the same sign. Therefore, electrons and holes will be confined in the smaller bandgap in Type I while they will be confined in different region in Type II band alignment.

[**] The dispersion of the conduction band(c.b.) and valence band(v.b) as a function of wave vector, k, (E-K relation) can be expressed as $E=\hbar k^2/2m^*$, where m^* is the effective mass of electron or hole. When the splitting between HH and LH is occurred, the dispersion of v.b. will be changed due to the change of the interaction between HH and LH.

2.2.2 LED performance parameters

If all injected carriers are successfully confined in the active region, recombined radiatively, and if emitted photons are escaping from the LED without loss, the external quantum efficiency will be 100%. However, some portion of the injected carriers will escape from the active region (hetero-barrier leakage), some portion of the recombination will be the non-radiative process, and some of emitted lights in active region will be trapped in the LED structure.

There are two basic ways of recombination of non-equilibrium carriers [††] in semiconductors: the radiative and non-radiative recombination. In the non-radiative recombination process, the excess energy is transferred to the lattice (phonon emission) or carriers (Auger recombination). The recombination rate R_{tot} can be expressed as,

$$R_{tot} = An + Bn^2 + Cn^3 \qquad 2\text{-}5$$

, where n is carrier density, A is the Shockley Read Hall (SRH) coefficient, B is the radiative recombination coefficient, and C is the Auger recombination coefficient. The SRH recombination is proportional to the carrier density, n, because the charge carrier trapped in a localized state within the band gap already occupies a state and waits for the recombination partner. No simultaneous participation of two carriers is required. Such states are likely formed by defects and surface states in a crystal so that the SRH recombination rate can provide the information of material quality. The non-radiative Auger recombination process describes that an energy released due to recombination of an electron-hole pair is transferred to another carrier to be excited to upper states. The Auger recombination becomes more pronounced as the carrier injection increases and the bandgap of the active region decreases because the less energy transformed in the Auger process, the easier to fulfill both energy and momentum conservation requirements during the recombination process. Among several Auger recombination mechanisms, CHCC and CHSH are dominant processes in III-V semiconductors. CHCC refers that the recombination energy between a Conduction band electron and a Heavy hole band hole is transmitted to excite another Conduction band electron to a higher state in the Conduction band. S in the CHSH indicates the split off valence band. It is proportional to n^3 because it requires simultaneous participation of three carriers (Figure 2.4). In the radiative recombination

[††] carriers generated by the external force

process, the recombination energy in the electron-hole pair is released in the form of electromagnetic emission (photon emission), which is the major luminescence mechanism for LEDs and lasers. The recombination coefficient B of a direct bandgap material is much larger than that of an indirect bandgap material that is obviously not preferred for efficient photonic devices. The recombination coefficient B at the equilibrium condition for direct bandgap bulk semiconductors was derived using a simple quantum mechanical model by Garbuzov [26], written as,

$$B = 3 \times 10^{-10} \left(\frac{E_g}{1.5}\right)^2 \left(\frac{300}{T}\right)^{1.5} \ (cm^3/s) \qquad 2\text{-}6$$

. Typical value of B for III-V direct gap semiconductors ranges 10^{-9} –10^{-10} cm^3/s.

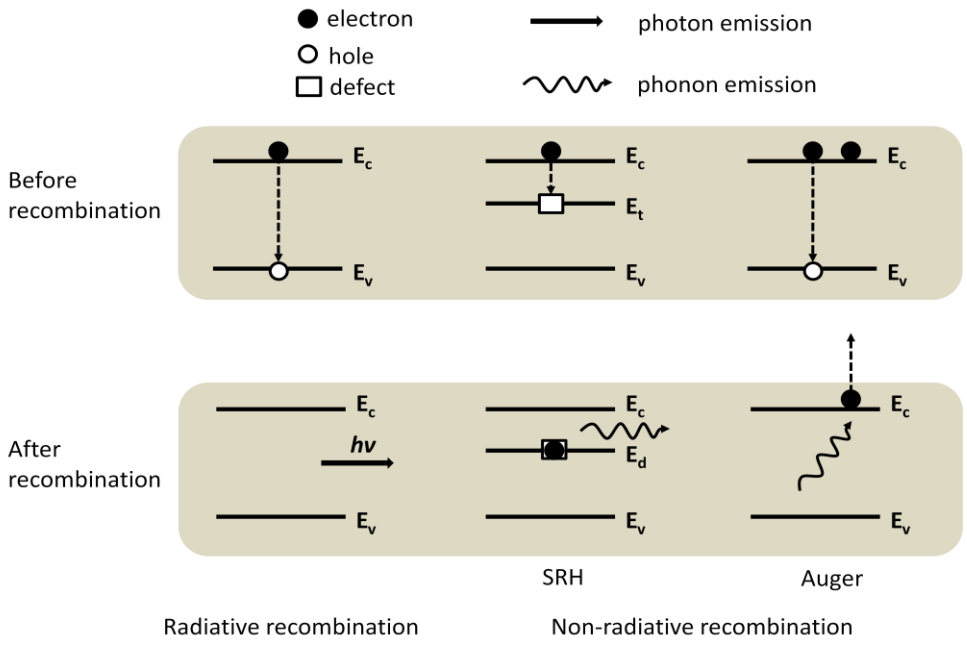

Figure 2.4 The recombination processes.

The cross section of a typical surface emitting LED is shown in Figure 2.5. If a photon generated at the active region (circled area) is incident to the normal direction to the semiconductor-air interface, the photon can escape from the LED. However, when the photon is incident with an angle larger than the critical angle, it will experience total internal reflection. The critical angle is the angle above which total internal reflection occurs, which is estimated using Snell's law as,

$$\theta_c = sin^{-1}\left(\frac{n_{r,air}}{n_{r,semi}}\right) \sim \frac{n_{r,air}}{n_{r,semi}} \quad \text{2-7}$$

, where $n_{r,air}$ and $n_{r,semi}$ are the refractive index of air and the semiconductor. For small angle, the critical angle can be approximated as $n_{r,air}/n_{r,semi}$. Since III-V semiconductors have the large refractive index, only some portion of generated photons can escape from the LED structure. For instance, the refractive index of GaSb is about 3.8 and thus the critical angle is about 15˚. Although the lights are incident within the critical angle, a part of them will be reflected at the semiconductor – air interface. The reflectivity can be expressed by Fresnel reflection given by,

$$R = 1 - T = 1 - \frac{4n_s n_{air}}{(n_s + n_{air})^2} = \left(\frac{n_s - n_{air}}{n_s + n_{air}}\right)^2 \quad \text{2-8}$$

, where R is reflection and T is transmission. For GaSb substrate, 35% of the lights incident to the normal direction to the semiconductor surface will be reflected back to the LED structure.

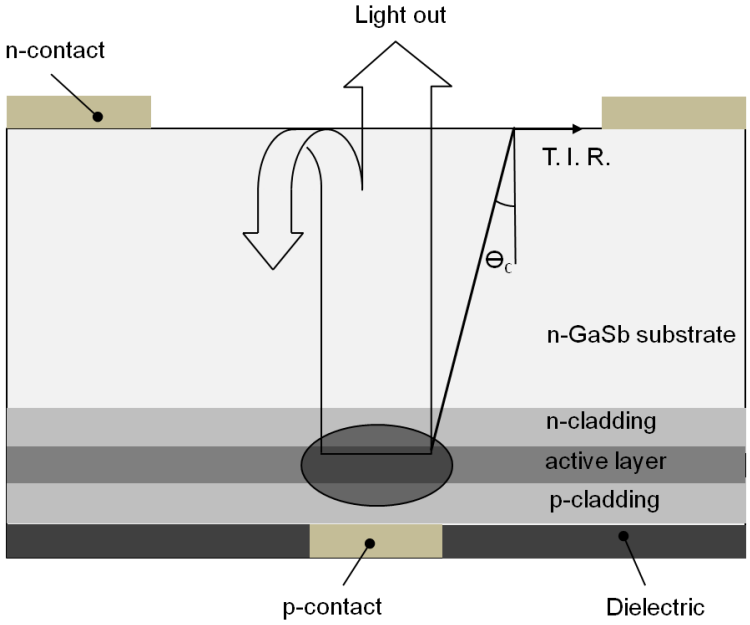

Figure 2.5 The cross section of the surface emitting LED.

The light propagating in the LED structure experiences absorption through an active region and substrate. In ideal case, a substrate should be transparent with respect to the wavelength of the generated photons if the bandgap energy of the substrate is higher than the photon energy. However, absorption may occur due to the presence of free carriers, doping impurities, and defects in the active region and substrate, which will be more critical for the long wavelength region [27-29]. Free carrier absorption can be estimated using the expression [28],

$$\alpha_{fc} = \frac{q^3 \lambda^2 N}{4\pi^2 \varepsilon_s c^3 n_r (m^*)^2 \mu_n} \qquad 2\text{-}9$$

, where q is the elementary charge, λ is the wavelength, N is the density of free carriers, n_r is the refractive index, m^* is the effective mass, ε_s is the dielectric constant of a semiconductor, and μ_n is the mobility of free carriers. Figure 2.6 shows the free carrier absorption coefficient as a function of wavelength with different doping concentrations of an n-type GaSb. As the wavelength increases from 1 to 10 μm, the coefficient increases two orders of magnitude.

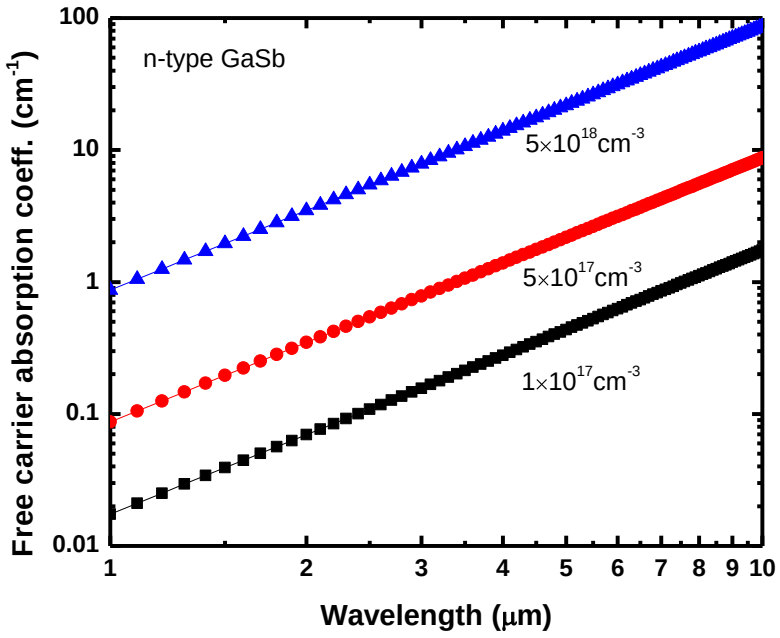

Figure 2.6 The calculated free carrier absorption coefficient as a function of wavelength with the different doping concentrations of n-type GaSb.

The output power is not appropriate metric to compare the device performance in LEDs (although mostly used) because the output power will be depending on the size of the emitting area, photon energy (wavelength), and bias current. The internal efficiency, η_{int}, is defined as the ratio of the number of photons generated from the active region per unit time to the number of electrons injected into 'the LED' (not the LED active region) per unit time, written as,

$$\eta_{int} = \frac{P_{int}/hv}{I_F/q} \qquad 2\text{-}10$$

, where P_{int} is the power emitted from the active region, hv is photon energy, I_F is the injected current, and q is the elementary charge. The internal efficiency, however, does not take into account how many carriers are injected into 'the active region' since carrier loss during transport from the external contact to the active region and the amount of leakage current passing though the LED structure without recombination are unknown without special characterization. The parameter that characterizes the ratio of the number of carriers injected into the active region over the total number of carriers injected into the device is the injection efficiency (also called as the internal efficiency in lasers with the completely different meaning, see Chapter 3). If the injection efficiency is known, we can estimate the radiative efficiency η_{rad}, defined as the radiative recombination rate to the total recombination rate,

$$\eta_{rad} = \frac{R_{rad}}{R_{tot}} = \frac{\eta_{int}}{\eta_{inj}} \qquad 2\text{-}11$$

The extraction efficiency η_{ext} is the parameter showing the fraction of the generated photons that escape the LED structure. By definition, the extraction efficiency is the ratio of the output power emitted from the LED to the power emitted from the active region.

$$\eta_{ext} = \frac{P_{out}}{P_{int}} \qquad 2\text{-}12$$

, where P_{out} is output power of the LED. The typical extraction efficiency of an LED is about 3%, meaning that only 3% of light emitted from the active region contributes to output power. The external quantum efficiency, η_{EQE}, is defined as the ratio of the number of photons emitted out from the LED per unit time to the number of electrons into the LED per unit time.

$$\eta_{EQE} = \frac{P_{out}/hv}{I_F/q} = \frac{P_{out}\ q}{I_F\ hv} = \eta_{int}\eta_{ext} \qquad 2\text{-}13$$

The conversion efficiency, also often called the wall-plug efficiency or the external power efficiency [6], η_{cv}, is defined as the ratio of the output power to the electrical input power.

$$\eta_{cv} = \frac{P_{out}}{P_{in}} = \frac{P_{out}}{I_F V_b} = \frac{P_{out}}{I_F(V_d + R_S I_F)} \qquad 2\text{-}14$$

, where P_{in} is the electrical input power, V_b is the bias voltage, V_d is the diode voltage (~E_g/q), and R_S is the series resistance.

2.3 Material survey

Available III-V material systems in the MIR region are shown in Figure 2.7. The horizontal dashed lines indicate the corresponding energies to wavelength from 3 μm to 10 μm. Material parameters are referred from [30]. InAs and InSb are the only binary materials whose bandgap energies belong to the MIR range among III-V materials. InAs with an InAsSbP barrier or InSb with an AlInSb barrier active region grown on InAs substrates is commonly used for λ=3-6 μm active regions. Incorporation of InAs and InSb is apparently limited by the lattice mismatch of ~7% so that a compressively strained self-assembled InSb quantum dot layer can be alternative to the bulk active region [19]. For ternary materials, the bandgap energies of GaInAs, InAsSb, GaInSb, and AlInSb are accessible into the MIR range. Among them, InAsSb is the most promising material due to its wide wavelength cover range. The bandgap of InAsSb with ~37% of As can reach the longest wavelength of ~14 μm among III-V alloys but its usability is limited up to λ~6 μm due to lattice mismatch with available substrates. To overcome such an issue, buffer layers such as step graded InAsSb layers on InAs [31] or relaxed GaInSb layers on GaSb [32], have been grown in between the active region and substrate to mitigate lattice mismatch.

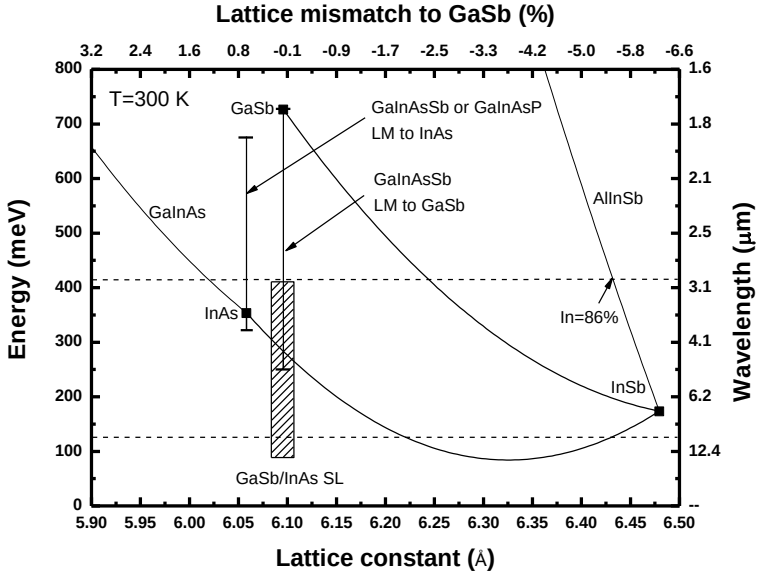

Figure 2.7 The bandgap of III-V semiconductor materials. Band parameters were taken from [30]. The horizontal dashed lines indicate the MIR spectral range. The crosshatched region indicates the bandgap energy of GaSb/InAs superlattice.

Quaternary InAsSbP grown on InAs and GaInAsSb grown on either InAs or GaSb can be also used for the MIR active region. The main advantage using the quaternary alloy is the change of the bandgap energy while maintaining the lattice matching condition. The bandgap of GaInAsSb lattice matched to GaSb can cover the wavelength of 1.7 μm to 5 μm. The miscibility gap of GaInAsSb lattice matched to GaSb is located within the indium composition of 30% ~ 70% [30, 33], which, however, can be accessible to some extent by using the low temperature growth technique such as MBE. In terms of wavelength controllability and growth flexibility, type II InAs/GaSb superlattice (the crosshatched region in Figure 2.7) grown on GaSb shows promising performance not only for emitters [22, 25, 34] but also for detectors [35].

We have chosen the GaInAsSb/AlGaAsSb material system as the primary type I QW/Barrier materials. The materials can be grown with the lattice matching condition on GaSb substrates that also provide transparent window for the MIR region. N-type doped GaSb substrate should be chosen if a LED is designed to emit light through the substrate since free holes have about one order of magnitude higher absorption than free electrons [29, 36]. Figure 2.8 shows the room temperature bandgap energy of AlGaAsSb and GaInAsSb lattice matched to GaSb as a function of the Ga content. The gray region visualizes the GaInAsSb band position. The valence band offset (VBO) bowing for both alloys is neglected. AlGaAsSb becomes the indirect bandgap material with the Ga content below 84%, while GaInAsSb shows the direct bandgap energy throughout the whole range of the Ga content. As the Al content increases, the bandgap of AlGaAsSb increases. The Al content of 80~90% can be used for cladding layers and the Al content of 30% for barrier or waveguide layers.

Figure 2.9(top) shows the band offsets of GaInAsSb alloy against to $Al_{0.85}GaAs_{0.068}Sb$ (solid) and $Al_{0.30}GaAs_{0.024}Sb$ (dash). The arrows address the Ga content of 25% or 75% in GaInAsSb that can offer the flat VBO with Al 85% or Al 30% of AlGaAsSb, respectively. Thus, LEDs with type I QWs emitting above 2.6 μm may suffer from insufficient VBO with $Al_{0.3}GaAs_{0.024}Sb$ barrier under the lattice matching condition. One solution is to apply the compressive strain into the GaInAsSb QWs. The heavy hole and light hole band splitting will offer additional ~100 meV of the VBO within the compressive strain of 1.5% so that the type I QW configuration can be maintained up to 3 μm.

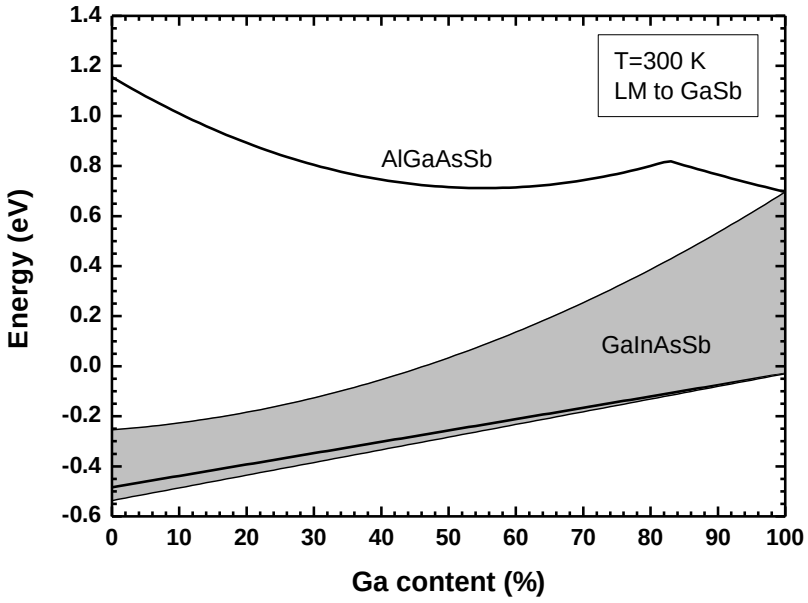

Figure 2.8 Bandgap energy of AlGaAsSb and GaInAsSb lattice matched to GaSb as a function of the Ga content, estimated at T=300 K. The gray region visualizes the GaInAsSb bandgap. The VBO bowing for both alloys is neglected.

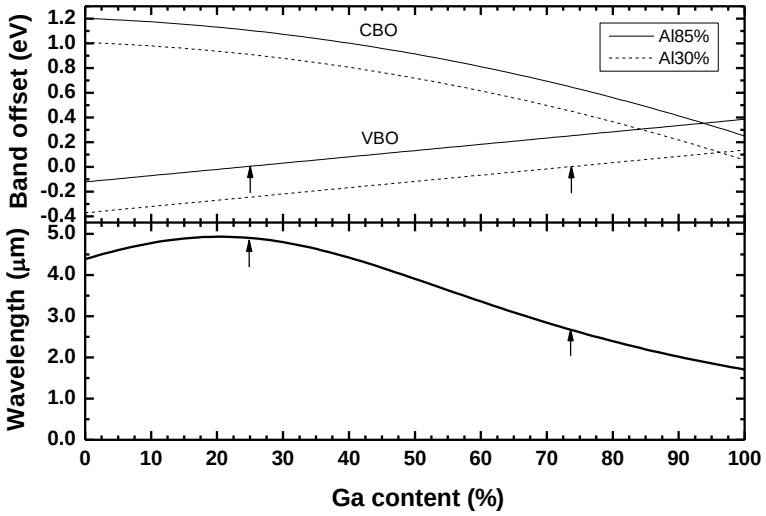

Figure 2.9 Band offsets (top) of GaInAsSb alloy against to $Al_{0.85}GaAsSb$ (solid) and $Al_{0.30}GaAsSb$ (dash) as a function of the Ga content. Wavelength of GaInAsSb alloy as a function of the Ga content is shown on the bottom. The arrows indicate the Ga content of GaInAsSb near the zero valence band offset with $Al_{0.85}GaAsSb$ and $Al_{0.3}GaAsSb$.

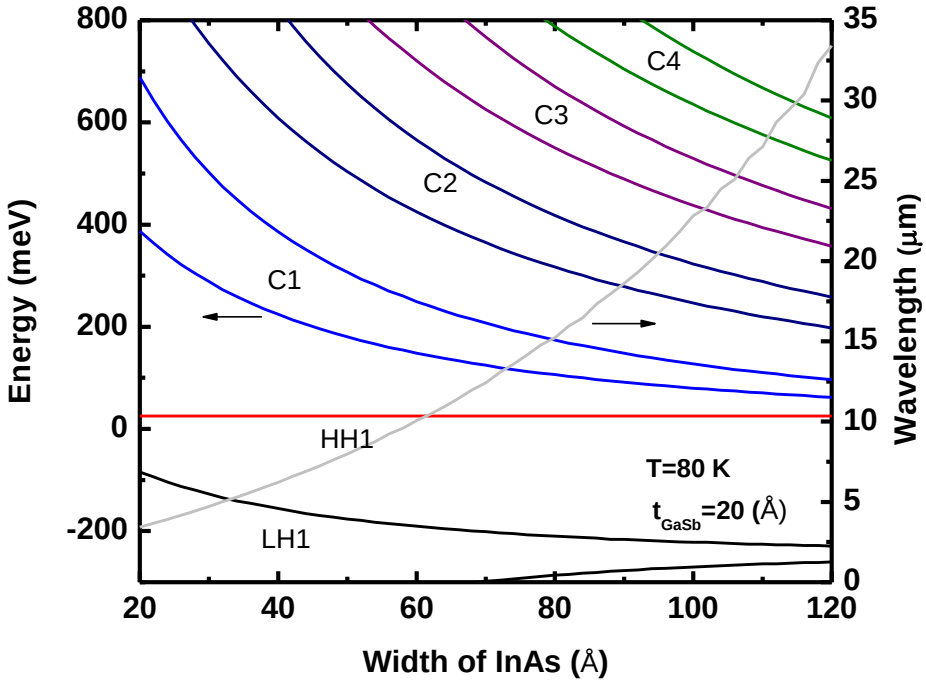

Figure 2.10 Calculated miniband energy of type II GaSb/InAs superlattice as a function of the InAs width at the fixed GaSb width of 20 Å at 80 K. The model used for this calculation can be found in [37, 38]. The wavelength was estimated at the minimum of the conduction band C1 and the maximum of the heavy hole band HH1.

Another important material system used in the long wavelength LEDs is the type II Ga(In)Sb/InAs superlattice. The superlattice is essentially alternating thin semiconductor layers with a period that is shorter than the electron mean free path. The electronic band structure of the superlattice is not only determined by the constituent materials but also by the thickness of them, thus often called 'quasi-bulk'. The calculated minibands of the GaSb/InAs superlattice as a function of InAs width at the fixed GaSb width of 20 Å is shown in Figure 2.10. Modified Kronig-Penny model described by G. Bastard [37, 38] has been used for the calculation. The bandgap energy is estimated at the minimum of the conduction miniband C1 and the maximum of the heavy hole band HH1. As the InAs width increases, the decrease of the quantized energy level in the InAs results in the wavelength change from 3 μm – 35 μm. The fixed width of the GaSb layer maintains the same energy level of HH1 regardless of the InAs width. Such wavelength control that only requires thickness change is the incomparable advantage of the

superlattice. Discrepancy between the calculated and measured bandgap [39] can be easily explained by that the energy level of the superlattice is greatly affected by the interface condition and strain [40]. However, the calculation can provide the relative tendency of the bandgap energy. Electrons and holes are confined in different layers in the type II broken gap configuration. That is the type II broken gap GaSb/InAs superlattice confines electrons in the InAs layer and holes in the GaSb layer, which is especially beneficial to suppress the Auger recombination but may also reduce the radiative recombination due to less wave function overlap between electrons and holes.

2.4 Fabrication and characterization

2.4.1 Fabrication

Fabrication includes all steps after material growth and before device packaging. The fabrication procedure described in this section can be applied not only to LEDs but also to lasers and photodetectors. Figure 2.11 shows the general fabrication steps. Order of the steps or additional steps can be varied or added depending on applications. This section covers general processing procedure and the specific case for each device will be addressed in the results section.

Surface of as-grown wafers should be cleaned and degreased from organic and metallic contaminants by using acetone (ACE), isopropanol (IPA), and de-ionized (DI) water in order. After nitrogen (N_2) gas blow, the wafer should be dehydrated on a hot plate at 120 ˚C~150 ˚C for 1~2 min. Photoresist will be coated on the wafer surface using a spinner with a suitable spinning speed and time depending on the specification of the photoresist. Photoresist, a photosensitive polymer, can be positive or negative and positive means the exposed area with UV light is soluble with developer, for negative, vice versa. Negative photoresist with reversed sidewall slope is preferred for a metal lift-off process. After making patterns for metal deposition, the wafer will be soaked into etchants to remove a native oxide layer. The surface of GaSb wafer is covered with a Ga_2O_3 native oxide layer formed due to reaction of surface dangling bonds and oxygen. This layer has to be removed to form metal contacts with good adhesion and conductivity. Removal of the GaSb oxide can be performed using etchants such as NH_4OH-based diluted with de-ionized (DI) water (NH_4OH:DI=1:20) or HCl-based (HCl:DI=1:10) solution.

Titanium (Ti), platinum (Pt), and gold (Au) are typically used to form the Ohmic contacts on the p-contacts and for the final contact layers on the n-contacts. In general, each layer has a specific purpose: Ti for adhesion with semiconductor surface, Pt for diffusion barrier of Au, and Au for high conductivity. For the n-contact, alloy with Ni, Au, and Ge is used to form Ohmic contacts for n-type GaSb, followed by an annealing process.

After lift-off process, epi-layer etching could be the next step to define mesa or ridge. Wet or dry etching can be used depending on the required degree of accuracy. Wet etching is simple and cost effective but isotropic etching profile and less uniformity are the limiting factors especially for low dimensional features. A selective wet etching technique is developed to fabricate narrow ridge waveguide lasers with vertical sidewalls, which is described in Section 3.3.2. Dry etching can perform superior anisotropic etching patterns with precise depth control but effort to optimize an etching recipe and maintenance of costly equipments could be drawbacks.

Dielectric deposition immediately follows the etching. Silicon nitride (Si_3N_4) is used as the dielectric layer deposited using a plasma enhanced chemical vapor deposition (PECVD). The characteristic of Si_3N_4 is superior to silicon oxide in terms of reliability and high refractive so that application of Si_3N_4 is preferred in optoelectronic devices. The precursor of Si_3N_4 is diethylsilane (DES), ammonia (NH_3), and nitrogen (N_2). The use of DES, which is a colorless liquid with a chemical formula of $(C_2H_5)_2SiH_2$, is beneficial for environmental safety compared to silane that is a highly explosive gas [41]. The thickness of ~200 nm is expected under 5 min deposition at the growth temperature of 250 ˚C with the ratio of DES:NH_3:N_2=1:1:10. If adhesion between the Si_3N_4 and semiconductor surface is problematic, nitrization process based on NH_3 plasma can be performed before the deposition.

Chemical and mechanical polishing is usually performed after completion of epi-side processing. This step is necessary to facilitate die cleaving and to increase light transmission (or minimize free carrier absorption through the substrate especially for long wavelength devices). Aluminum and titanium carbide powders are typically used for lapping and polishing, respectively.

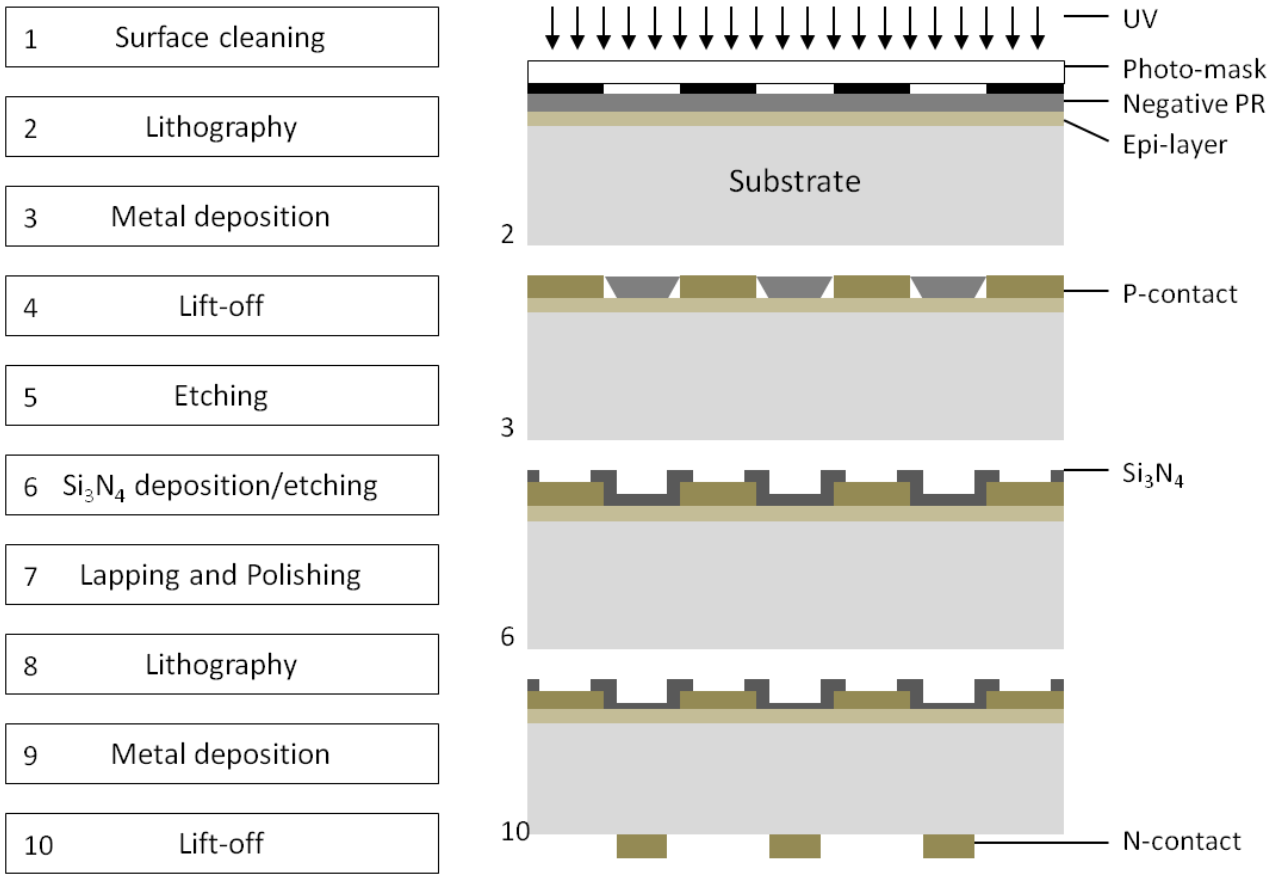

Figure 2.11 The fabrication flow chart (left) and illustration (right) corresponding to the step indicated.

2.4.2 Characterization

Optical power is one of the most important parameters of LEDs. There are several methods to measure optical power. One can obtain the relative optical power by integrating electroluminescence of a LED, measured using a FTIR at different bias currents. Since FTIR can measure signal with low intensity, one can obtain light current dependence at very low bias current range. However, it requires sufficient time and effort to measure each current point and perform data processing. In addition, one has to assume that the EL intensity is uniform along the emission plane if the near field or spatial dependence is not characterized. Another method is a measurement system using a photodetector (PD). It can provide high sensitivity and selective spectral bandwidth by choosing suitable detector and band pass filter. Photocurrent produced by modulated LED light is usually amplified by a trans-impedance amplifier and lock-in amplifier

to improve the signal to noise ratio in the system. In order to obtain absolute power, the LED emission pattern must be known and the PD and LED should be well aligned along the optical axis to carry out accurate measurement. However, many geometrical and optical factors, such as three dimensional adjustment and optical loss from lenses (if used), can readily affect the measurement results so that it may be difficult to expect high reproducibility and reliability.

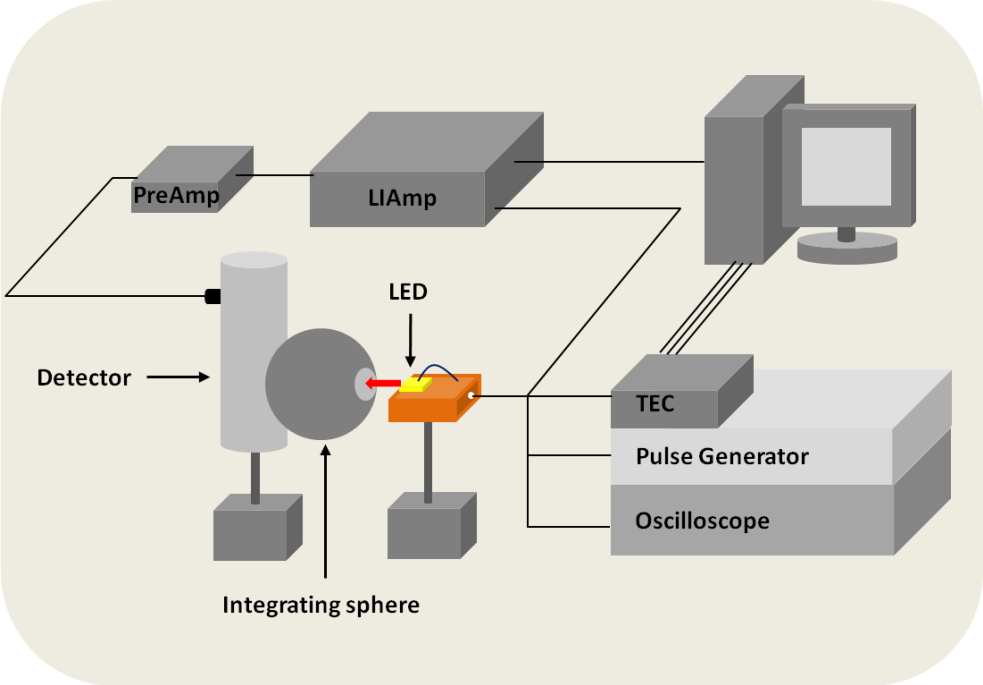

Figure 2.12 The measurement system of LED optical power.

The measurement system that we used for the presented LEDs is shown in Figure 2.12. LED light is collected and homogenized through the gold-coated integrating sphere with 1 inch of the aperture diameter. Such large aperture increases tolerance of optical adjustment and allows for reliable and reproducible measurement results. Either InSb or MCT photodetector was used to measure mid or long wavelength signal, respectively. A pre- and lock-in-amplifier synchronized with a pulse generator were used to improve the signal to noise ratio. The system was controlled by a LabView program for measurement automation.

A novel calibration method using a blackbody radiator was developed to calibrate the entire measurement setup. The configuration of the system is illustrated in Figure 2.13. We introduce the setup responsivity K (W/V) in equation 2-15 as the coefficient between the output voltage of the lock-in amplifier and LED output power, expressed as,

$$P_{LED} = K(\lambda_0)V_{LED} \quad \text{2-15}$$

, where λ_0 is the wavelength corresponding to the peak of the LED emission spectrum and V_{LED} is the photovoltaic signal produced by LED power. Since the photodetector sensitivity has a strong spectral dependence, the responsivity coefficient K is a function of the LED spectral bandwidth, which can be expressed as,

$$K(\lambda_0) = \frac{S_{eff}\int_0^\infty S(\lambda'' - \lambda_0)d\lambda'' \int_0^\infty D(\lambda)R(\lambda, T_B)\lambda d\lambda}{\Delta V_B \int_0^\infty D(\lambda')S(\lambda' - \lambda_0)\lambda' d\lambda'} \quad \text{2-16}$$

, where S_{eff} is the effective area of the blackbody source, $D(\lambda)$ is the photodetector sensitivity in arbitrary units, $R(\lambda, T_B)$ is the spectral radiant exitance of the blackbody at a temperature T_B, is the $S(\lambda'' - \lambda_0)$ luminescence spectrum of an LED in arbitrary units centered at λ_0, and V_B is the voltage signal produced by the blackbody. The derivation of this expression is given in Appendix 1. Although we can use the measured electroluminescence of a LED, a Gaussian model has been used for the demonstration purpose, which will introduce the uncertainty of ±3% compared to the case using the electroluminescence. The operating temperature of the blackbody was set at 1000 ◦C. Inner aperture of the blackbody source has a diameter (D) of 6.2 mm and outer aperture has diameter (d) of 2.5 mm (Figure 2.15).

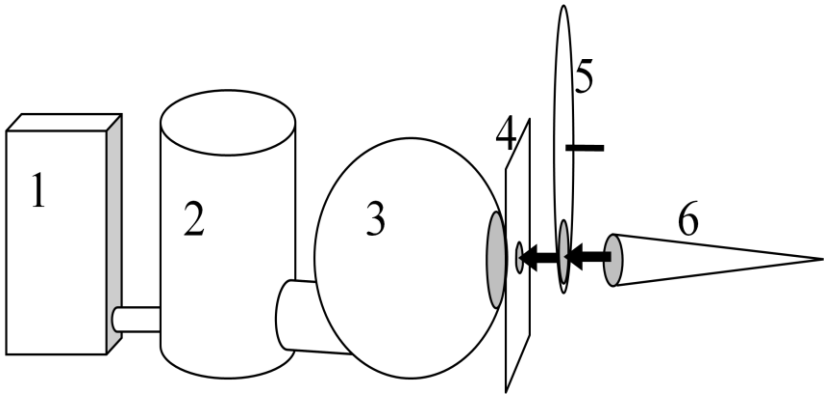

Figure 2.13 The experimental setup for the calibration. 1–preamplifier, 2–detector, 3–integrating sphere, 4–blackbody thermal shield, 5–modulator, 6–blackbody cavity.

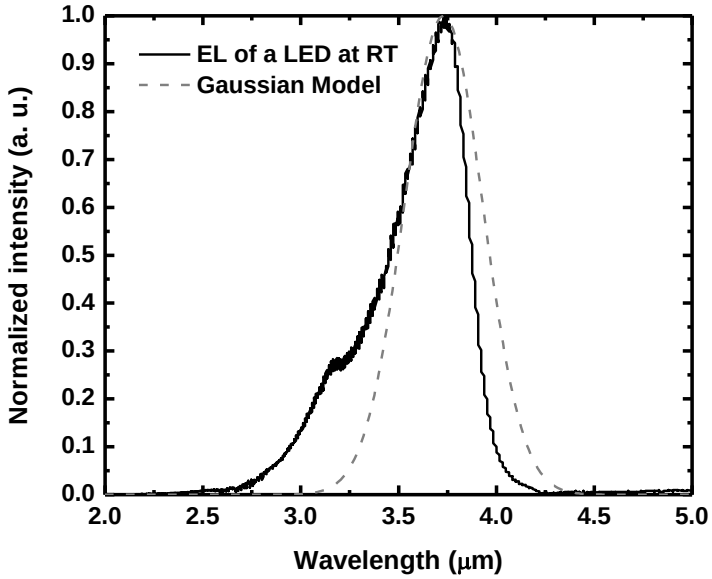

Figure 2.14 Electroluminescence of a LED and its Gaussian model.

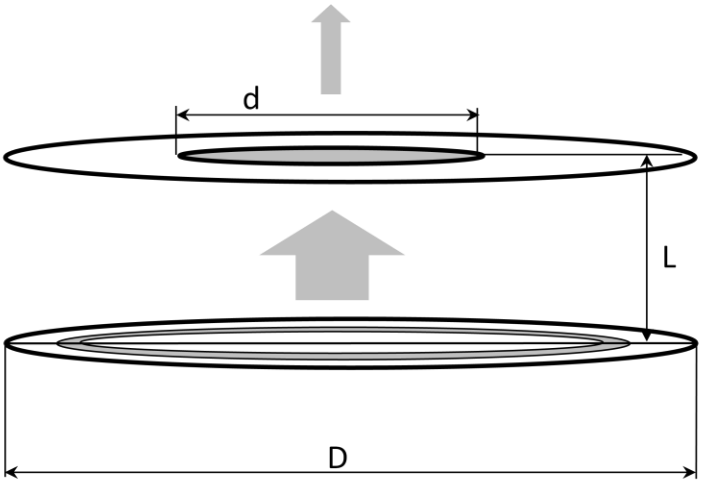

Figure 2.15 The scheme for calculation of total power entering the thermal shield aperture.

The distance (L) between two apertures is filled with the 8 mm thick thermal shield and 4 mm thick ceramic sealing. The trans-impedance preamplifier with the linear gain of 5000 [V/A] has been employed to convert photocurrent into voltage (V_B). The total number of quanta entering the integrating sphere was calculated using the geometrical parameters of the blackbody source. Figure 2.16 shows the coefficient K, which is estimated as a function of the wavelength. The increase of K near the wavelength of 4 μm is due to CO_2 absorption of the InSb detector,

indicating that spectral dependence of the detector sensitivity is well reflected into the coefficient. To demonstrate the reliability of this calibration method, one of commercial LEDs has been measured and compared with its specification. The measured power from the measurement system shows good agreement with the specification of the LED, as shown Figure 2.17. Since the LED was measured without a temperature controller, discrepancy may be occurred due to device heating at high bias current.

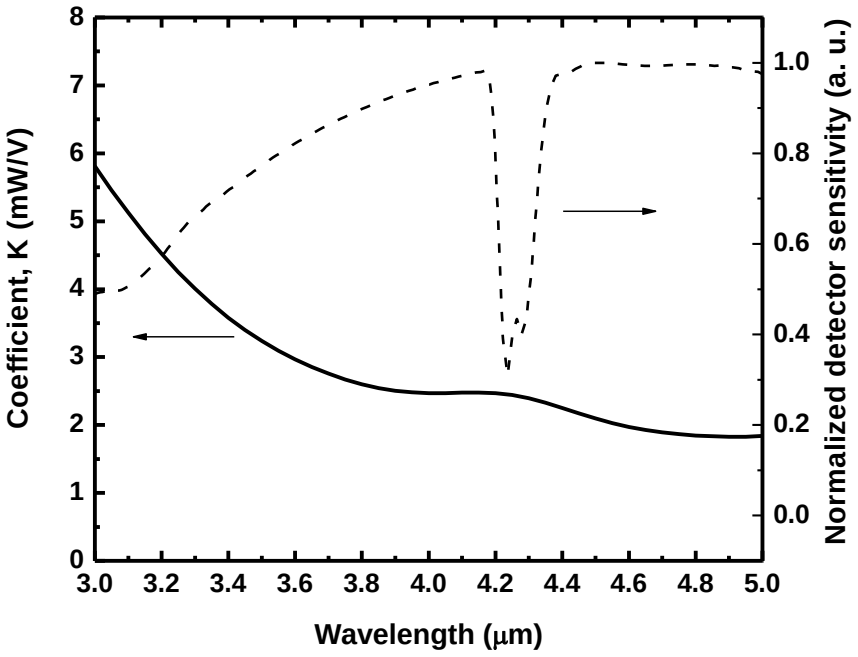

Figure 2.16 The estimated coefficient, K as a function of wavelength (solid) and the normalized InSb detector sensitivity (dashed).

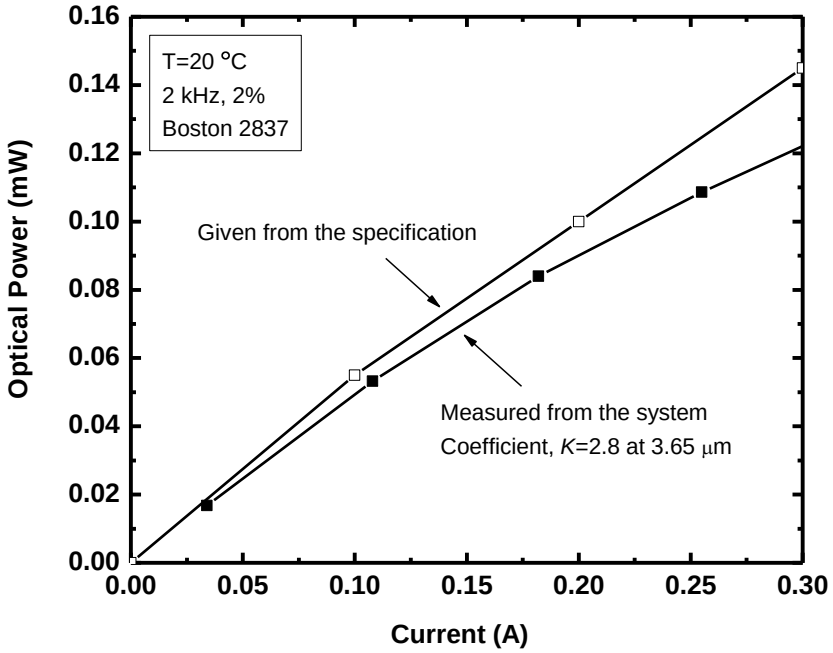

Figure 2.17 Optical power as a function of current obtained from a commercial LED: open sympbol-specificaiton values, closed symbol-measured values.

2.5 Experimental results and discussion

This section presents single emitters with various active region designs in order of the short wavelength to the long wavelength active region. For λ=2~2.5 μm, the compressively strained type I GaInSb QW active regions are exploited. Bipolar cascade LEDs emitting near 2 μm generated room temperature qCW optical power as high as 11 mW. For λ=3~3.7 μm, a quinternary AlGaInAsSb barrier has been introduced into active region instead of the quaternary $Al_{0.30}GaAs_{0.024}Sb$ barrier. LEDs emitting at 3.3 μm exhibited 0.7 mW qCW power at room temperature and apparent temperature more than 1000 K. For λ>3.7 μm, double heterostructure with a GaInAsSb bulk or GaSb/InAs type II superlattice active region are designed. Various functionalities of the MIR LEDs based on an optimized heterostructure design have been demonstrated including highly dimensional LED arrays with 512×512 addressable pixels and independently controlled dual wavelength LEDs and their arrays.

2.5.1 Type I QW bipolar cascade LEDs at 2 μm

Figure 2.18 shows the band positions of $Al_{0.85}GaAs_{0.068}Sb$ and $Ga_{0.8}InSb$ alloys at 300 K. The high Al content between 80% ~ 90% was used for the AlGaAsSb alloy as the cladding layer and the Al content of 30% was used for the barrier layer composition. Those Al contents are consistently used for devices using the AlGaAsSb/GaInAsSb material system in this thesis. The $Ga_{0.8}InSb$ QW layer grown on GaSb is compressively strained as much as 1.2% so that the heavy hole band is shifted upward about 50 meV, resulting in the total VBO of ~120 meV. The CBO is about 250 meV.

The bipolar active region cascading design was demonstrated as an effective way to stack several active regions within a single device [42-44]. Among several, major advantages of the active region cascading are electron recycling and operating voltage conversion. Recombination of injected electron and holes in the first active region is followed by interband tunneling through reversely biased p-n junction and carrier injection into the next active region. Thus, the internal quantum efficiency more than 100% can be achievable. A controlled ratio between input current and voltage, the consequence of active region cascading, allows for impedance matching between the device and driving electronics [45].

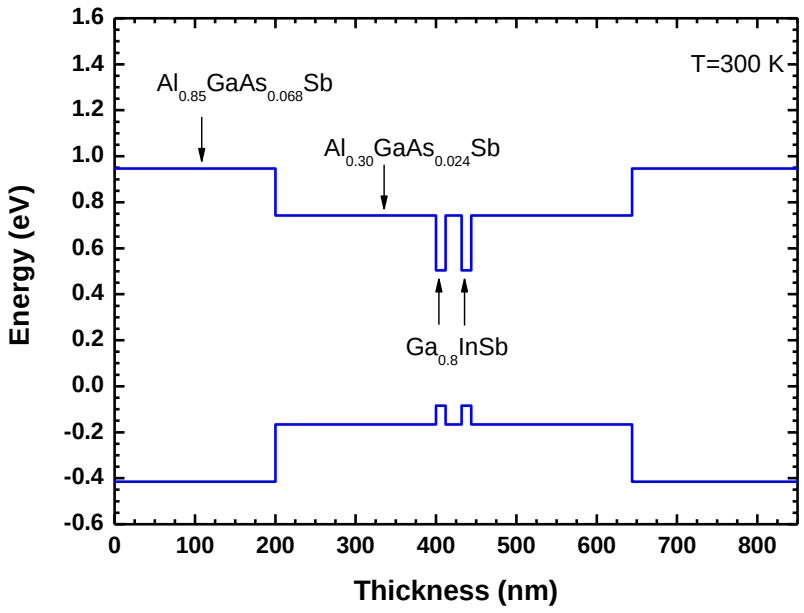

Figure 2.18 Bandstructure of the type I QW active region for λ~2 μm.

Two stage cascaded LED structure and single stage reference LED structure were grown on n-type GaSb substrates by using a Veeco Gen 930 solid source MBE system. A 500-nm-thick Te doped $Al_{0.85}GaAs_{0.068}Sb$ cladding layer was grown on top of a 200-nm-thick grading layer. An active region consisted of two 12-nm-thick $Ga_{0.8}InSb$ QWs and a 20-nm-thick $Al_{0.3}GaAs_{0.024}Sb$ spacer that were enclosed by 200-nm-thick $Al_{0.3}GaAs_{0.024}Sb$ barrier layers. Then, a 500-nm-thick Be doped $Al_{0.85}GaAsSb$ cladding layer and a 200-nm-thick grading layer were grown, followed by a 100-nm-thick GaSb cap layer. For the 2-stage LED, a tunnel junction between the identical active regions was formed with n- and p-type GaSb layers with the thickness of 500 nm, respectively. All layers were lattice matched to GaSb and doped with the concentration of 1×10^{18} cm^{-3} except for the QW layers.

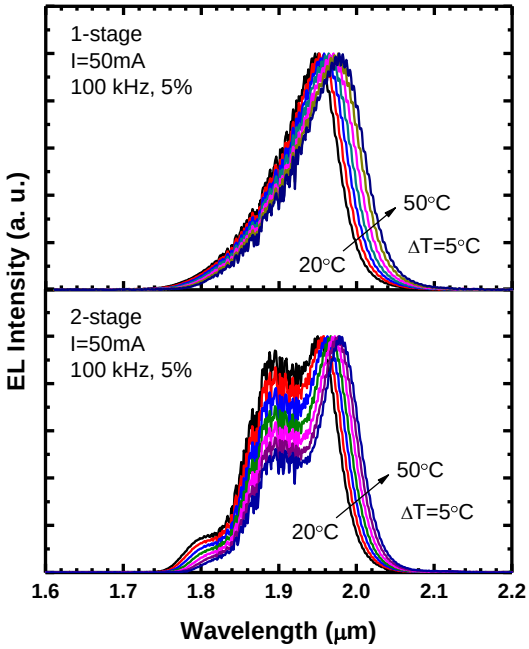

Figure 2.19 Normalized electroluminescence of the 1-stage and 2-stage LED measured from 20 ˚C to 50 ˚C with a 5 ˚C step under pulse mode (100 kHz, 5%).

Electroluminescence spectra of each LED were measured at different temperatures (Figure 2.19), using a Fourier transform infrared (FTIR) spectrometer. The emitting area was $1.3\times10^{-3}cm^2$ for both LEDs. The peak wavelengths of the LEDs were not well resolved due to distortion by water absorption near 1.9 μm. We estimate the peak wavelength as 1.93 μm based on a line shape analysis from the short and long wavelength tail. The short wavelength peaks (1.8

μm and 1.9 μm) of the 2-stage LED are possibly artificial peaks due to interference occurred in the thick active region. The wavelength-tuning rate is about 0.95 nm/˚C for both LEDs.

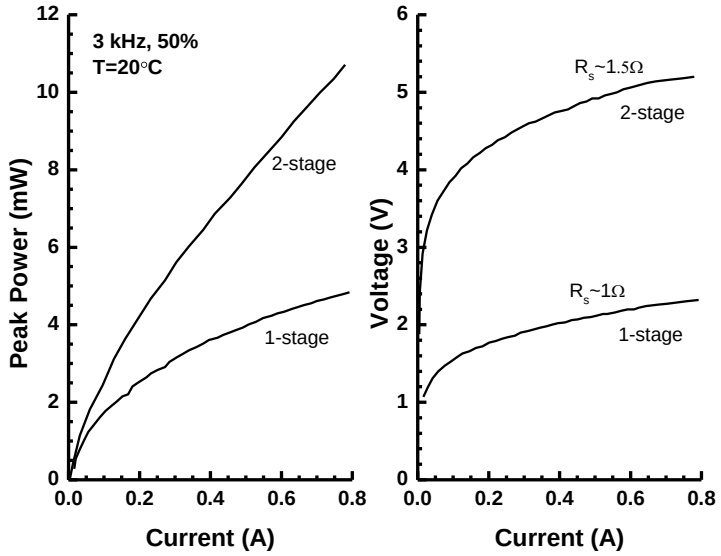

Figure 2.20 Light- Current-Voltage of the 1-stage and 2-stage LED measured at 20 ˚C under qCW mode (3 kHz, 50%).

Optical power measured at room temperature is shown in Figure 2.20. The 1-stage and 2-stage LED generated optical power as high as 5 mW and 11 mW under qCW mode (3 kHz, 50%) at 20˚C, respectively. The 2-stage LED produced nearly twice-higher optical power at the same bias current than that of the 1-stage LED. Applied voltage at the same optical power is well scaled with the factor of two; for instance, at 4 mW, voltage of the 1-stasge LED is 2.1 V and that of the 2-stage LED is 4.2 V. Using Ni/Au/Ge/Ni/Au alloy contact followed by annealing and overlay process, the bias voltage can be reduced by ~1 V. The series resistance is estimated at high bias current region and 1.0 Ω for the 1-stage and 1.5 Ω for the 2-stage is estimated.

The performance parameters are estimated at the fixed output power of 4 mW. Assuming that the radiative efficiency is the same for both single stage and cascaded devices, and no additional voltage is consumed in the tunnel junction, we can expect the same wall plug efficiency (WPE) from the LEDs. We obtained the values of the WPEs for the 1-stage and 2-stage LED as 0.36% and 0.51%, respectively. The higher WPE on the 2-stage LED is attributed to the higher radiative efficiency of the cascading active region where the Auger recombination rate is reduced since the required carrier concentration in each QW for a fixed optical power

level can be decreased in the cascade scheme. In contrast to lasers, carrier concentration in LEDs is not pinned at threshold current. Thus, the Auger recombination can be considerable at higher bias currents. The internal efficiency is estimated using the equation 2-13,

$$\eta_{int} = \frac{\eta_{EQE}}{\eta_{ext}} = \frac{P_{out}\, q}{\eta_{ext} I_F\ hv} \qquad 2\text{-}17$$

, where η_{EQE} is the external quantum efficiency, η_{ext} is the extraction efficiency, hv is the bandgap energy, and q is the elementary charge. Taking into account critical angle and multiple reflection in a typical planar structure, the η_{ext} is estimated to be ~4%. The internal efficiencies for the 1-stage and 2-stage LED are 30% and 84%, respectively. The radiative efficiency per QW, η_{rad}/QW , can be estimated as 17% for the 1-stage and 23% for the 2-stage LED, using the injection efficiency of 90% taken from a laser diode with the similar heterostructure [46]. Figure 2.21 shows optical power of the 2-stage LED with different temperatures. The 2-stage LED generated 7 mW of qCW power at 50 ˚C and the characteristic temperature of 70 K at I=0.77 A was obtained.

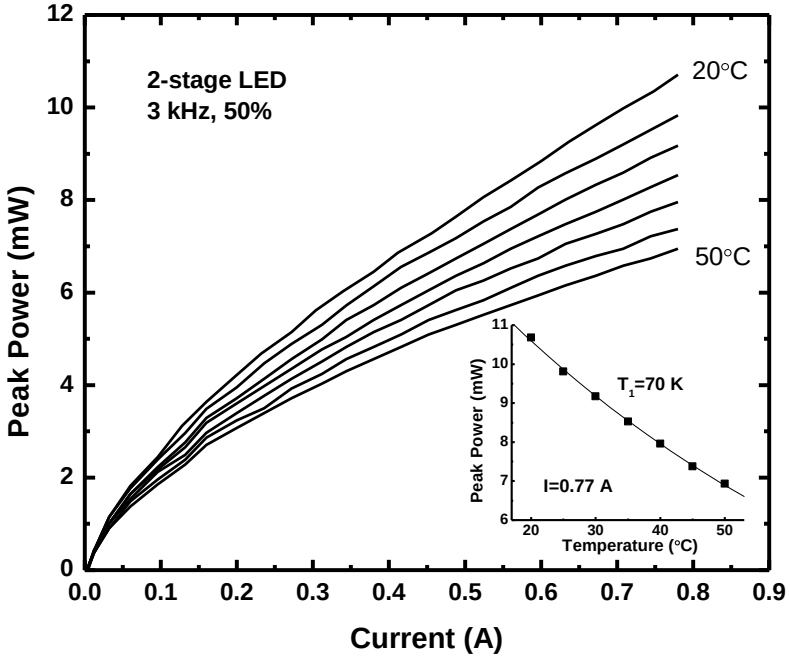

Figure 2.21 Temperature dependence of optical power of the 2-stage LED biased under qCW mode (3 kHz, 50%). The inset shows the characteristic temperature, T_1 of 70 K estimated at I=0.77 A.

2.5.2 Type I QW LEDs at 3.0 µm ~ 3.7 µm

Hole localization can be problematic for AlGaAsSb/GaInAsSb type I QW LEDs operating at wavelengths above 3 µm. Devices emitting above 3 µm require In content >50% in the QW and simultaneously As content >20% should be kept in the QW to maintain the strain below 1.6%–1.9%. The increased As content leads to a strong reduction of hole confinement resulting in degraded performance at higher temperatures.

We evaluated two different approaches to improve hole confinement. In the first approach, we increased the Al content in the AlGaAsSb barrier from 30% to 35% and in the second approach we employed a quinternary AlGaInAsSb barrier in the LED design. As we obtained lattice-matching condition in the quaternary alloy, application of quinternary alloy provides an additional degree of freedom allowing for independent control of strain and valence band offset. In both cases, hole confinement was restored due to an increase in the valence band offset between the barrier and the QW.

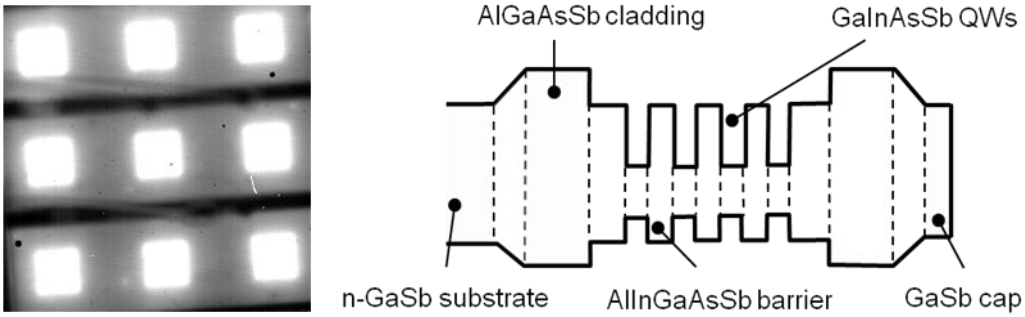

Figure 2.22 The IR image of a working LED at room temperature (left) and schematic bandstructure with the quinternary AlInGaAsSb barrier (right).

Four compressively (1.7% – 1.9%) strained GaInAsSb QWs separated by 40 nm were incorporated into the AlGaAsSb or AlGaInAsSb barriers (Table 2-1). The emission wavelength was controlled by adjusting the In content in the QW material and the QW width. The active region was sandwiched between doped layers of either $Al_{0.9}GaAs_{0.07}Sb$ or $Al_{0.6}GaAs_{0.05}Sb$ to form the diode structure (Figure 2.22). The substrate was *n*-doped with Te to $2\sim3\times10^{17}$ cm^{-3}, and the epitaxial side was *p*-doped with Be to 2×10^{18} cm^{-3}. A 50-nm-thick Be doped *p*+GaSb cap was grown on top of the structure.

Figure 2.23 shows the room temperature electroluminescence for each device. As the temperature decreases from 300 to 80 K, the maximum of each spectrum shifts toward shorter wavelengths at a rate of ~2.3 nm/K. The shorter wavelength of device 1 is possibly due to blue shift caused by high temperature exposed to the wafer during the structure growth. The device voltage and series resistance increase as the temperature decreases from 200 to 80 K (Figure 2.24). This is attributed due to a reduced carrier concentration in the claddings or barriers at lower temperatures.

Table 2-1 The list of devices for comparison between quaternary and quinternary barrier LEDs.

Device	Cladding	Barrier	QW	Number of QWs	QW width (nm)
1	$Al_{0.9}GaAs_{0.07}Sb$	$Al_{0.35}GaAs_{0.03}Sb$	$In_{0.545}GaAs_{0.22}Sb$	10	12
2	$Al_{0.6}GaAs_{0.05}Sb$	$Al_{0.2}In_{0.25}Gas_{0.24}Sb$	$In_{0.540}GaAs_{0.24}Sb$	4	17
3	$Al_{0.6}GaAs_{0.05}Sb$	$Al_{0.2}In_{0.2}GaAs_{0.2}Sb$	$In_{0.540}GaAs_{0.24}Sb$	4	17
4	$Al_{0.9}GaAs_{0.07}Sb$	$Al_{0.35}GaAs_{0.03}Sb$	$In_{0.545}GaAs_{0.22}Sb$	5	12

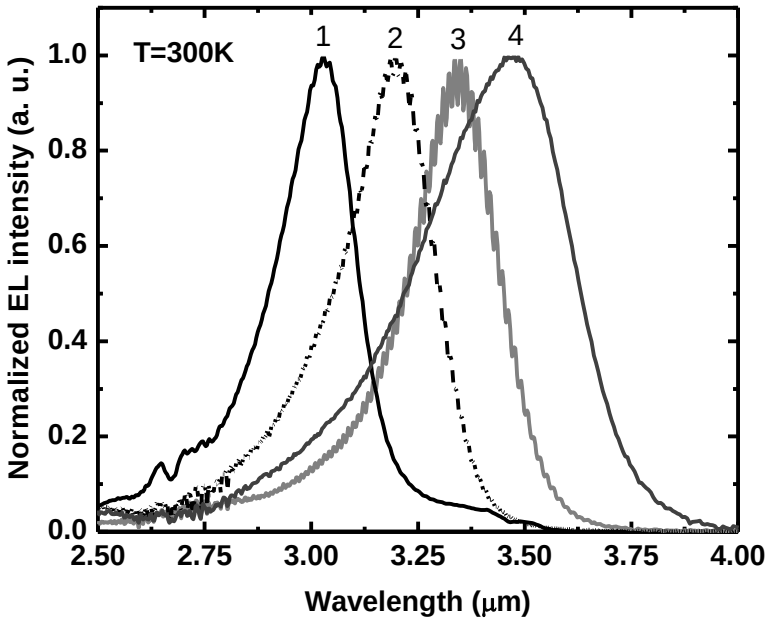

Figure 2.23 Electroluminescence of each device at T=300 K.

Optical power as a function of current for each device is shown in Figure 2.25. Measurements were performed under qCW (3 kHz, 50%) mode at room temperature. The difference between two groups with the different barrier material is apparent. More than twofold increase in optical power is obtained from device 2 in comparison to the power of device 1, indicating that the improved VBO using the AlGaInAsSb barrier results in the better internal efficiency. The sub-linear tendency of the L-I curves is due to a combination of device heating, increased Auger recombination, and hetero barrier leakage over the QWs. The dependence of output power on bias current for device 2 at several different temperatures is shown in Figure 2.27. Optical power was increased about 5 times at 80 K compared to the room temperature.

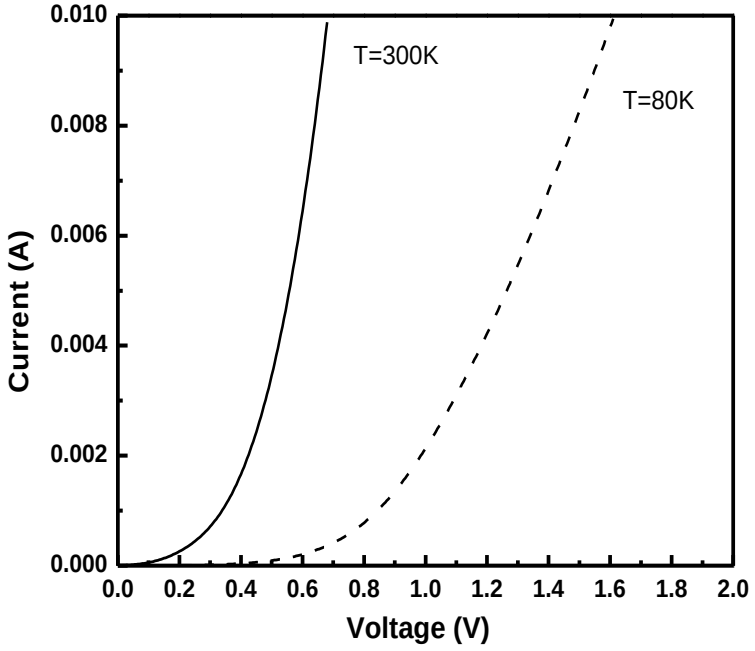

Figure 2.24 Current-Voltage dependence of device 2 at T=300 K and T=80 K.

Figure 2.26 plots the internal efficiency of each device calculated using the equation 2-17. The extraction efficiency is estimated using the small angle approximation, written as,

$$\eta_{ext} = \frac{1}{4}\frac{n_{air}^2}{n_s^2}T \qquad 2\text{-}18$$

, where n_{air} and n_s is the refractive index of air and semiconductor, and T is the Fresnel transmission (equation 2-8). Taking into account the T~0.7 and n_s of 3.8, the extraction efficiency is about 3%. Device 2 shows the internal efficiency as high as 24% at low current and

it decreases to 9% at the highest bias current due to the reason mentioned above. Although the value of the efficiency is incomparable, the quaternary devices show relatively small efficiency drop as bias current increases, which is possibly originated from many numbers of QWs, allocating less carriers in each QW, compared to the others.

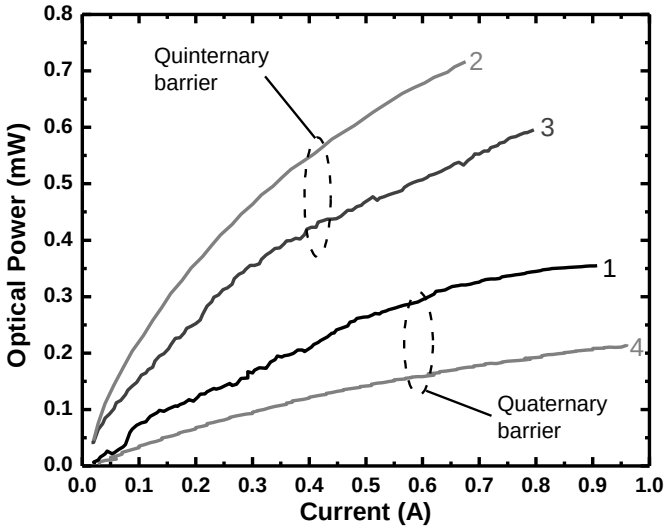

Figure 2.25 The dependence of light power on bias current for the devices with quaternary and quinternary barriers under qCW (3 kHz, 50%) mode at 300 K.

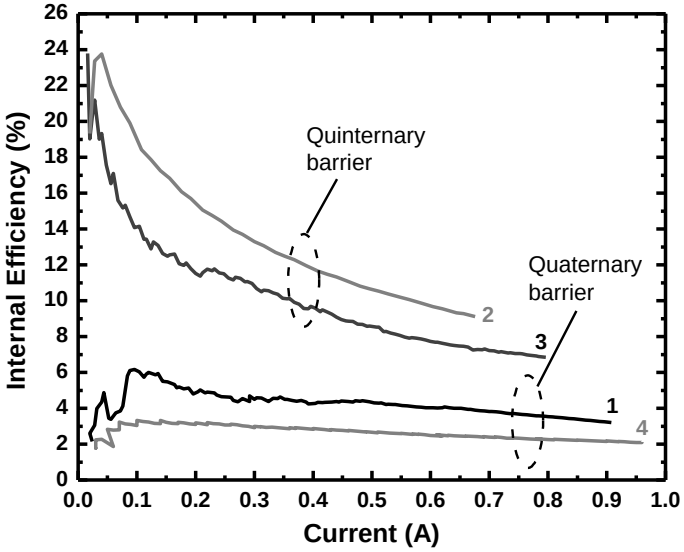

Figure 2.26 The internal efficiency of each device under qCW (3 kHz, 50%) mode at 300 K.

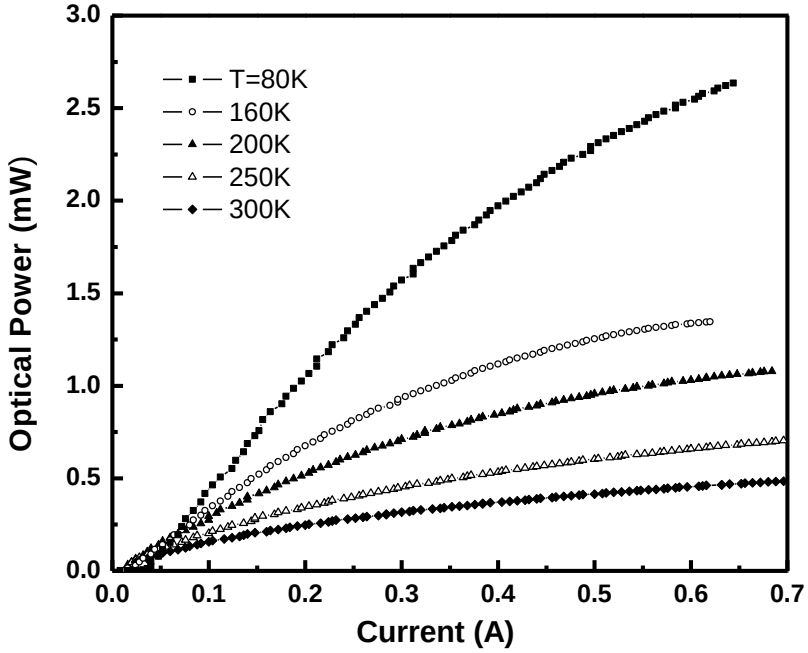

Figure 2.27 The dependence of light power on bias current, measured under qCW (3 kHz, 50%) mode from device with the quinternary barrier emitting at 3.15 μm (device 2).

Applying the same strategy, i.e. using the AlGaInAsSb barrier material with the compressively strained QW structure, we pushed the wavelength up to 3.66 μm by adding more In and As into the QWs. The active region composed of $Al_{0.9}GaAs_{0.07}Sb$ cladding (200 nm) / $Al_{0.2}In_{0.25}GaAs_{0.24}$ barrier (100 nm, 25 nm spacer) /$In_{0.56}GaAs_{0.29}Sb$ (18 nm) 4×QWs with 1.5% of the compressive strain.

Figure 2.28 and Figure 2.29 plot the electroluminescence and optical power with different temperatures, respectively. The peak wavelength was blue-shifted with the rate of 0.25 meV/K as temperature changed from 300 K to 100 K. The fringes in the spectra are due to interference through the LED substrate. The additional spectral peak at the high-energy side (~3.15 μm) of the room temperature spectrum is probably originated from the transition from the higher electron sub-band to the valence sub-band in the QW. Optical power under qCW mode has reached to 1.6 mW at 100 K and to 0.2 mW at 300 K.

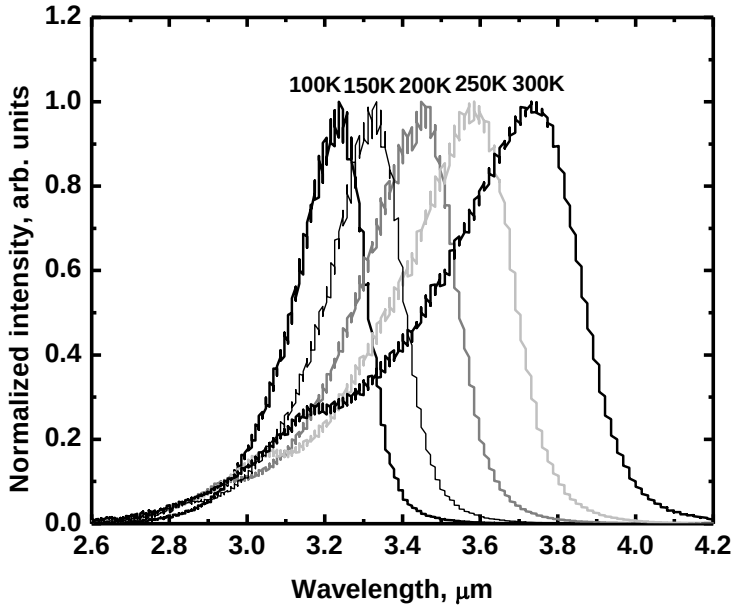

Figure 2.28 LED spectra at different temperatures.

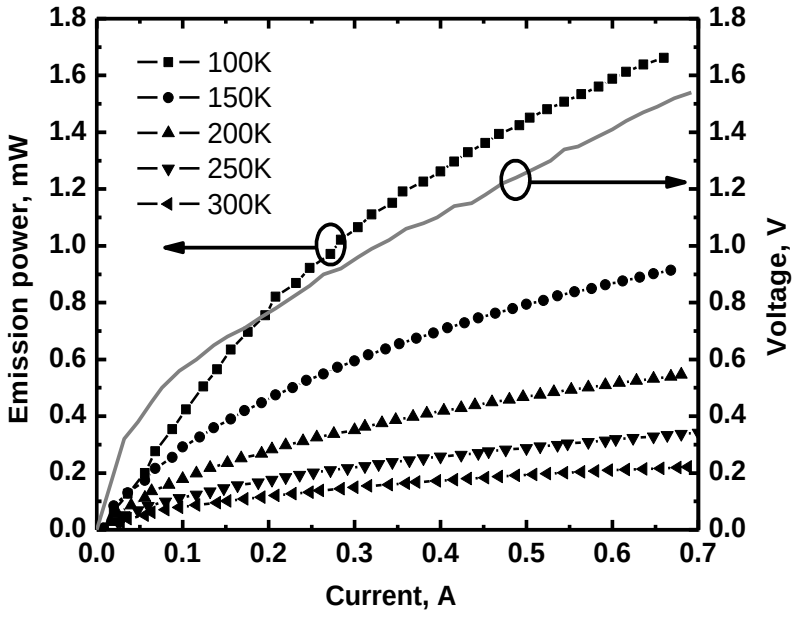

Figure 2.29 The dependences of the output power vs. bias current for non-addressable 3×3 LED array at different temperatures and the current-voltage dependence at room temperature.

2.5.3 Double heterostructure LEDs at 3.7 μm ~ 4.0 μm

As we push the wavelength longer than 3.7 μm, requirement of In content >50% in GaInAsSb makes material growth difficult to obtain high quality active region since the composition fall into the middle of the miscibility gap where In content of 30% ~ 70% belongs to [30, 33]. To avoid the miscibility gap, a LPE grown DH LED emitting at 3.7 μm [7] was demonstrated using the type II interface between AlGaAsSb and $Ga_{0.066}In_{0.934}As_{0.83}Sb_{0.17}$, resulting in pulse power of 3.2 mW at room temperature. Another approach to emit the wavelength with the type I interface is to exploit non-equilibrium growth capability of MBE [47]. To minimize effort to improve hole confinement in QW structure, we rather used the DH structure composed of $Al_{0.85}GaAs_{0.068}Sb$/GaInAsSb/ $Al_{0.85}GaAs_{0.068}Sb$.

Two active regions were tested with the same Al cladding layers. The bandgap energies and band offsets of each active region are calculated and shown in Figure 2.30. The bandgap energy of $In_{0.50}GaAs_{0.46}Sb$ and $In_{0.54}GaAs_{0.49}Sb$ is about 0.32 eV and 0.3 eV, respectively and the VBO is about 120~130 meV for both LEDs.

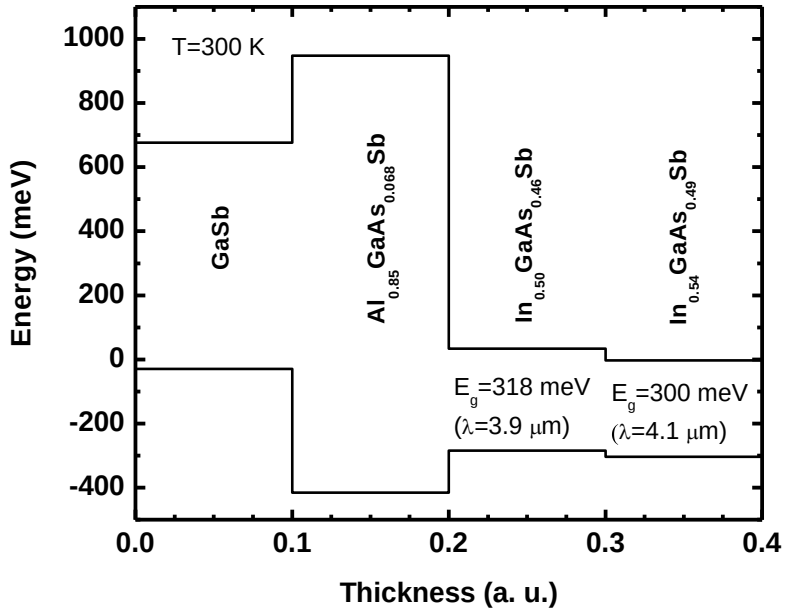

Figure 2.30 The calculated bandgap energy and band offsets of AlGaAsSb and GaInAsSb materials lattice matched to GaSb at 300 K.

The $In_{0.50}GaAs_{0.46}Sb$ (λ=3.75 μm) or $In_{0.54}GaAs_{0.49}Sb$ (λ=4.05 μm) undoped active region was enclosed by the 300 nm thick n- and p-$Al_{0.85}GaAs_{0.068}Sb$ cladding layers doped with Te or Be of 1×10^{18} cm^{-3}, respectively. A 100-nm-thick p-type GaSb cap layer was grown on the top of the structure. All layers were intended to be lattice matched to GaSb. Using HR-XRD, the compressive strain of InGaAsSb was estimated about 0.01% for λ=3.75 μm and 0.3% for λ=4.05 μm LED with respect to GaSb. The wafers were fabricated with the same manner as described before. The emitting area of each pixel is 120×120 μm^2 and a LED device has total 9 pixels.

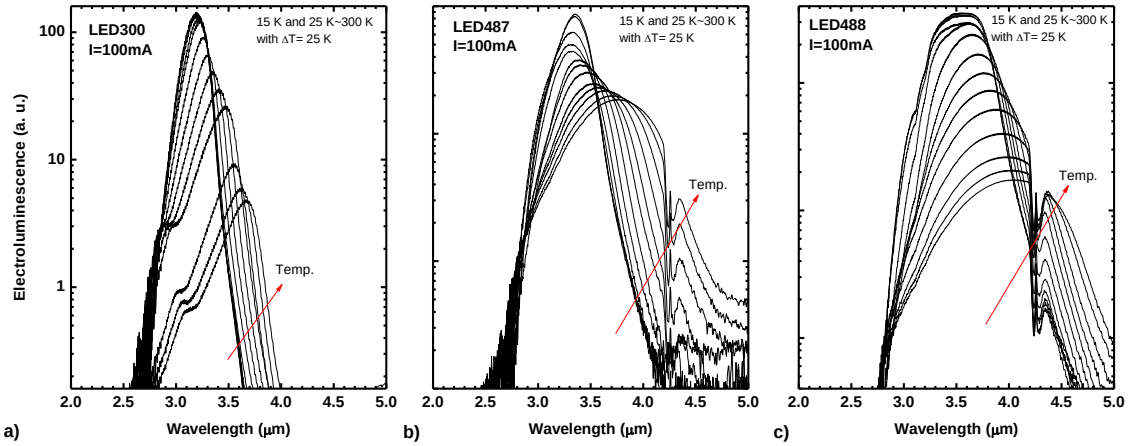

Figure 2.31 Electroluminescence of the QW LED300 (a), DH LED487 with In 50% (b), and DH LED 488 with In 54% (c), measured at 15 K and from 25 K to 300 K with a 25 K step at fixed CW current of 100 mA.

The electroluminescence of both DH LEDs as well as the QW LED measured at fixed current is presented in Figure 2.31. Heterostructure design of the QW LED is described in the previous section. The luminescence spectra of the bulk active region is determined by the product of the joint density of states and Boltzmann distribution of carriers, expressed as, $I(E)\sim\sqrt{E-E_g}exp\,(-E/kT)$. The peak wavelength can be found by taking derivative of $I(E)$, and thus,$E_{peak}=E_g+kT/q$. The peak wavelengths of 3.75 μm and 4.05 μm at 300 K are in good agreement with the calculated bandgap energy. The wavelength slope on the higher energy side was converged to near 2.7 μm for all three LEDs, which ensures that the injected carriers are well confined in the active region so that no recombination occurs in the cladding layer. By decreasing the temperature, the peak wavelength of all LEDs shows blue shift with the rate of ~2

nm/K within the temperature range from 300 K to 100 K. Below 100 K, the wavelength nearly unchanged (Figure 2.32 (a)). FWHM of each LED becomes narrower as temperature decreases (Figure 2.32 (b)). The QW LED shows the notably narrow long wavelength tail compared to LED487 emitting at the similar wavelength. The feature is essentially originated from the quantized density of states of the thin active region.

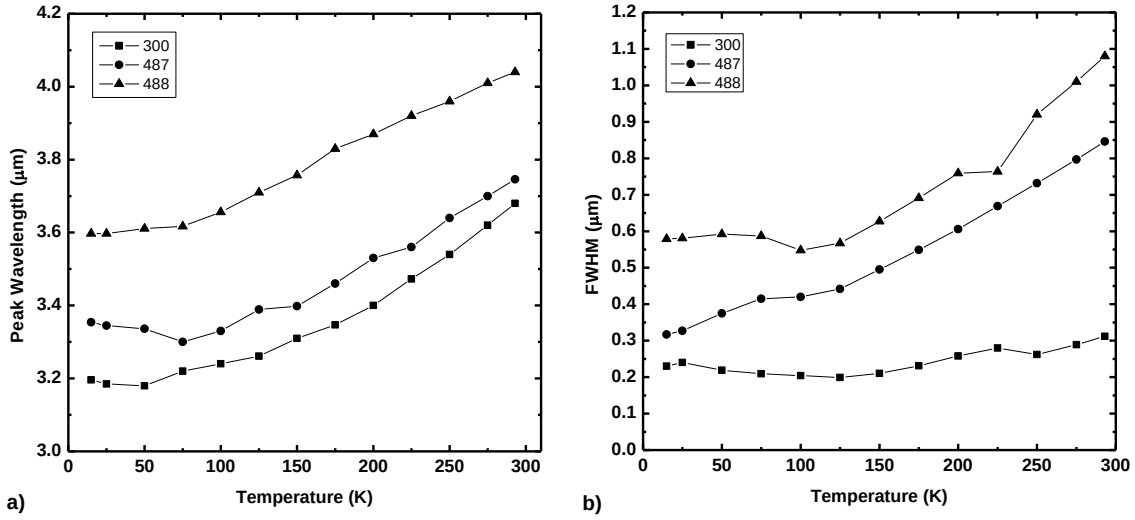

Figure 2.32 The peak wavelength (a) and FWHM (b) as a function of temperature: square – QW LED300, circle – DH LED487 with In 50%, and triangle – DH LED488 with In 54%.

Figure 2.33 shows optical power as a function of current at 20 ˚C under qCW mode (3 kHz, 50%). Both bulk LEDs generated similar optical power at room temperature, corresponding to 80 μW. The external efficiency, defined as the ratio of the output photon number to the input electron number, is estimated to be about 0.03% at 0.9 A. For comparison, a DH LED operating at 4.2 μm grown by LED produced the external efficiency of about 0.02% under CW mode [15]. The internal efficiency decreases from 2.8% to 1% as current increases due to the combined effects of joule heating and the increased Auger recombination rate.

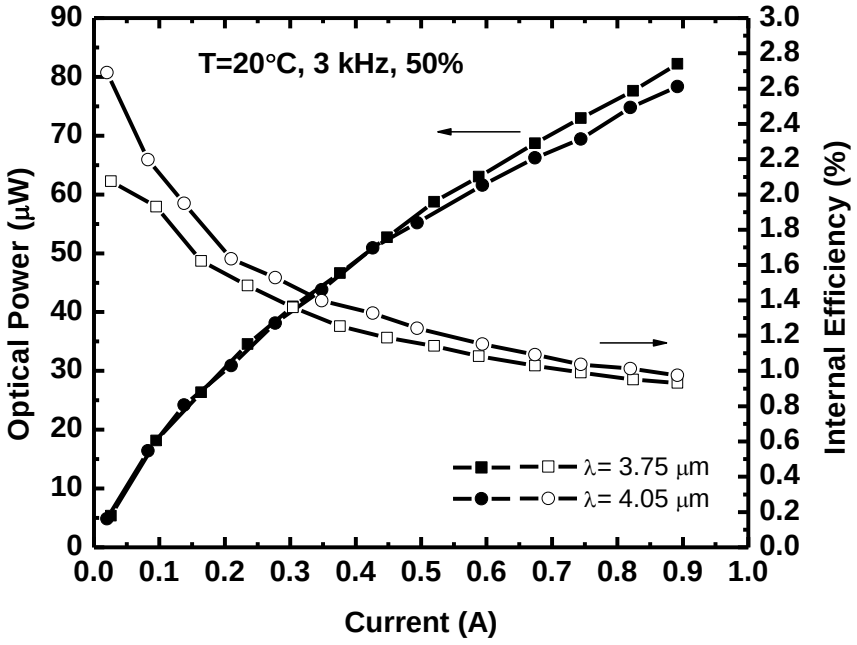

Figure 2.33 Optical power and the internal efficiency as a function of current for λ=3.75 μm LED (square) and for λ=4.05 μm LED (circle) at room temperature under qCW mode (3 kHz, 50%).

Light-current-voltage (L-I-V) characteristics of three LEDs measured at 293 K and 80 K are presented in Figure 2.34. QW LED300 produced 2.5 times higher optical power and 0.3 V higher bias voltage than DH LEDs at 0.3 A. The total thickness of 4-QWs in LED300 is 56 nm that is about 5 times smaller active region volume than that of the DH LEDs. Thus, high carrier density in the QWs enhances the radiative recombination rate, resulting in high optical power. In fact, the high carrier concentration could be detrimental at high current where the Auger recombination rate becomes dominant recombination process. This situation can be supported by low temperature performance. The QW LED shows one order of magnitude power increase at 80 K, while the DH LEDs about 5 factors, indicating that the QW LED has low value of characteristic temperature compared to the DH LEDs. The additional voltage on the QW LED probably comes from the voltage across the undoped barrier layer that seems to have high resistance causing carrier injection issue [48] and it becomes more dominant at low temperature.

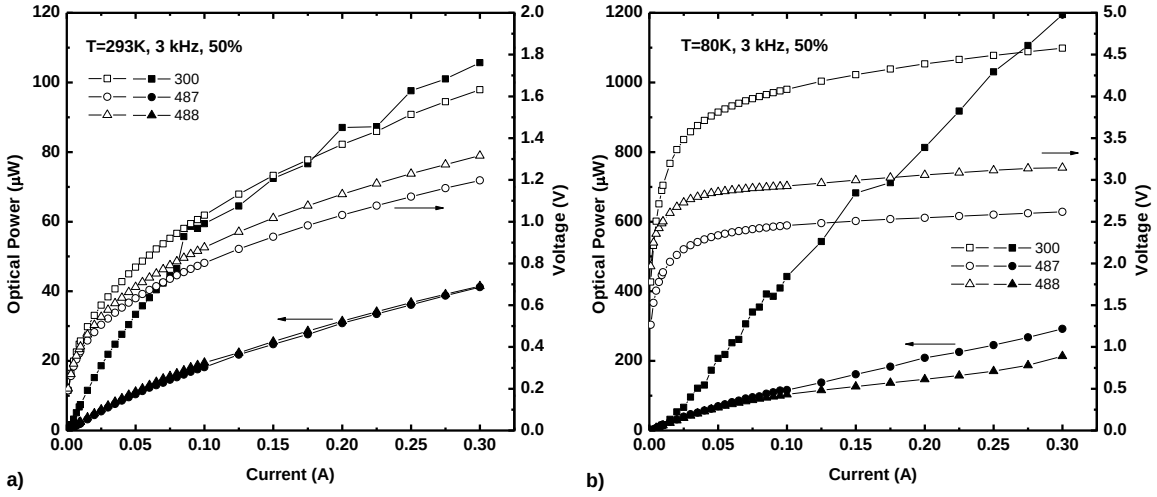

Figure 2.34 L-I-V of QW LED300, DH LED487, and DH LED488 at room temperature (a) and 80 K (b) under qCW (3 kHz, 50%) mode.

2.5.4 Type II superlattice LEDs at 4 μm ~ 10 μm

2.5.4.1 Type II InAs/GaSb superlattice vs. Type I double heterostructures LED at 4 μm

Type II broken gap superlattice (SL) has been suggested for the active region of the MIR LEDs and lasers due to the wavelength controllability from MWIR to LWIR, and suppression of the Auger recombination rate by modifying the density of states in valence bands [49]. In the sense, the type II active region LED may perform superior temperature characteristics than a LED with the type I active region since the Auger coefficient, C is a strong function of the temperature. The advantages of the SL LED, however, are not apparent because the spatial separation of electrons and holes in the type II interface may reduce the radiative recombination, thus the less output power compared to the type I LED. In this section, we shall compare the performance of the type I InGaAsSb bulk and type II InAs/GaSb SL LED grown by MBE for the wavelength near 4 μm.

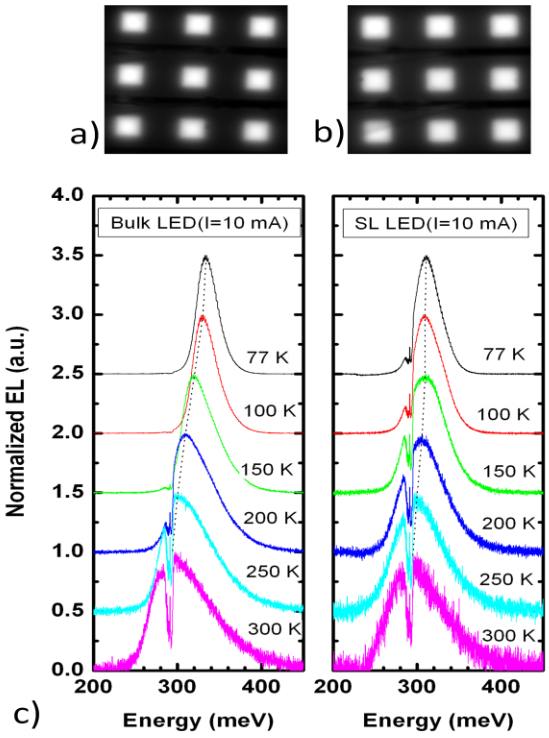

Figure 2.35 The IR image of Bulk (a) and SL (b) LED at RT under 100 mA and electroluminescence of Bulk (left) and SL (right) LED, measured from 77 K to 300 K under 10 mA CW current (c).

As we discussed in the material survey section, the wavelength of SL can be controlled by changing the thickness of the constituent materials, InAs and GaSb. For example, as increase the thickness of InAs from 20 Å to 140 Å with the fixed GaSb thickness of 20 Å, the wavelength of the superlattice can be varied from 4 μm to 14 μm. To emit the wavelength close to 4 μm, InAs/GaSb type II active region is designed with the 75 periods of 17 Å InAs/20 Å GaSb layer: total active region thickness of ~300 nm. Except for the SL active region, all other layers are identical to those of LED 488 bulk LED. We assume that the wave function of electrons in this SL is fully overlapped, while that of holes is likely localized in GaSb valence bands.

The IR images of the bulk and SL LED, shown in Figure 2.35 (a-b), were taken by a focal plane array IR camera. Uniform light distribution on each pixel confirmed high quality of material growth and device processing. Electroluminescence spectra of the bulk and SL LED were measured from 77 K to 300 K using FTIR and InSb photovoltaic detector (Figure 2.35(c)). Both samples were excited by CW current of 10 mA. The peak wavelengths of 4.05 μm (3.7 μm) and 4.25 μm (4 μm) at 300 K (77 K) were obtained from the bulk and SL LED, respectively.

Such long wavelength of the SL LED neither from InAs (λ = 3.4 μm) nor from GaSb (λ = 1.7 μm) is the direct evidence of the type II SL property. The SL LED shows smaller wavelength shift than that of the bulk LED, indicating a different recombination mechanism between the type I and type II structure since the bandgap of the type II SL is not directly governed by that of constituent materials [35].

The observed full width half maximum (FWHM) at 77 K is about 28 and 38 meV for the bulk and SL LED, respectively, which is larger than the thermal broadening effect of ~2kT (13 meV). This wide FWHM, especially for SL LED that forms many interfaces in the active region, may be contributed from the inhomogeneous line broadening process such as compositional fluctuation and interface roughness [50]. The band filling effect is observed as bias current (CW) increases from 10 mA to 600 mA at a fixed temperature, 293 K (Figure 2.36).

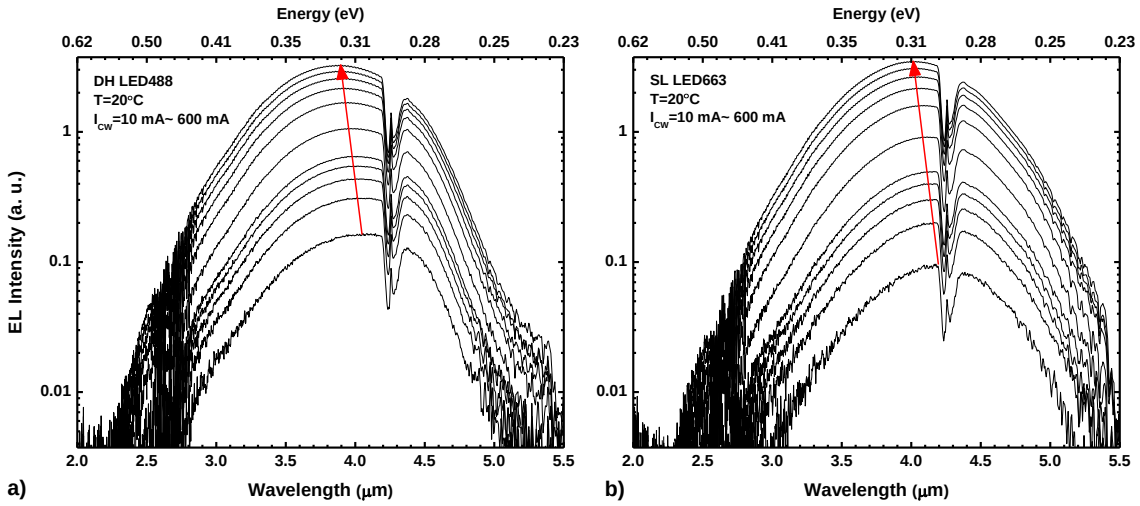

Figure 2.36 Electroluminescence as a function of current for DH LED (a) and SL LED (b) measured at room temperature under CW bias current. Current range is from 10 mA to 50 mA with 10 mA step and from 100 mA to 600 mA with 100 mA step.

Figure 2.37 shows qCW (3 kHz, 50%) optical power as a function of current at different temperatures. Optical powers of 80 μW (0.72 mW) and 65 μW (0.55 mW) were obtained at 300 K (77 K) from the bulk and SL LED, respectively. Although each device was derived up to the limit of the pulse generator, the obvious saturation was not observed. The bulk LED generated about 20% more power than that of the SL LED throughout the whole temperature range. Since

both LEDs consisted of the same structure and similar peak wavelength, the power difference mainly comes from the internal efficiency difference. The characteristic temperature T_1 can be estimated using the relation, $P \sim P_0 exp\,(-\frac{T}{T_1})$. Figure 2.38 shows optical power dependent on temperature at a fixed current. Both LEDs show the similar value of T_1 of ~100 K that is independent on bias current.

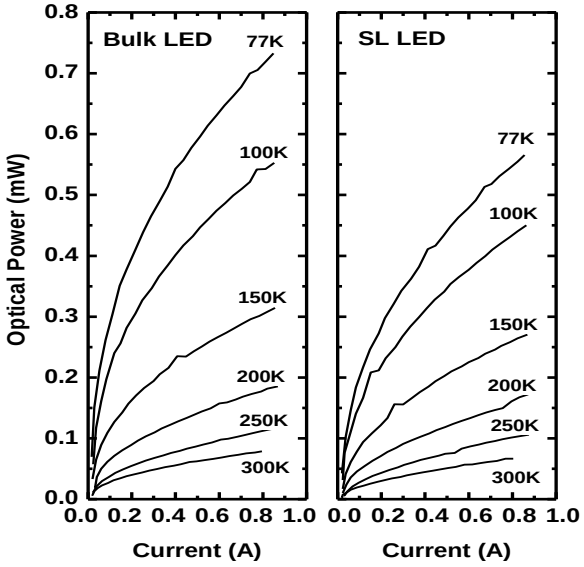

Figure 2.37 Optical power of the InGaAsSb bulk (left) and SL (right) LED as a function of current under qCW (3 kHz, 50%) mode with different temperatures.

To investigate the material quality, the minority carrier lifetime of each LED was measured using the optical modulation response technique. Detail of the technique is described in [51]. Since our study is only concerned with the relative value of the lifetime at the same pumping level, the limitation of the lifetime was not fully investigated but assumed Shockley-Read-Hall recombination under the moderate excess carrier pumping level of $\Delta n \approx 10^{15} \sim 10^{16} cm^{-3}$ [51]. The samples were excited at RT using a 1.55-μm distributed feedback laser with the excitation area of 7×10^{-4} cm^2. Figure 2.39 shows the frequency response of each LED under the same excitation power of 250 mW. The excess carrier density was estimated as $1.5 \times 10^{17} cm^{-3}$ (Bulk) and $5.6 \times 10^{16} cm^{-3}$ (SL) assuming the absorption coefficient about 10^4 cm^{-1} for both samples. Fitting a curve with pumping power density, we can find the 3 dB frequency corresponding to the inverse lifetime. The lifetime of SL and Bulk active region is 25 ns and 65

ns, respectively. About twofold shorter lifetime of the SL LED seems to be responsible for the low internal efficiency compared to that of the DH LED.

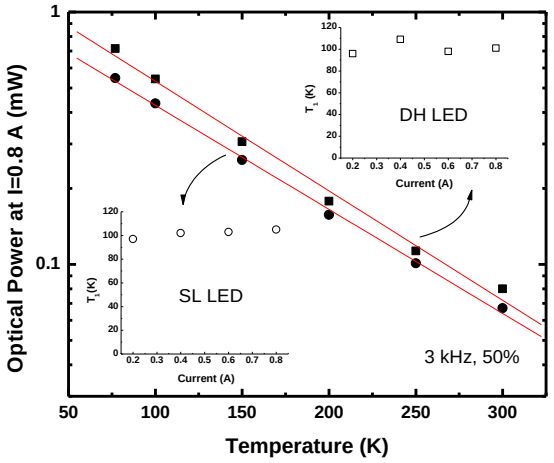

Figure 2.38 The characteristic temperature T_1 at different bias currents for DH and SL LED.

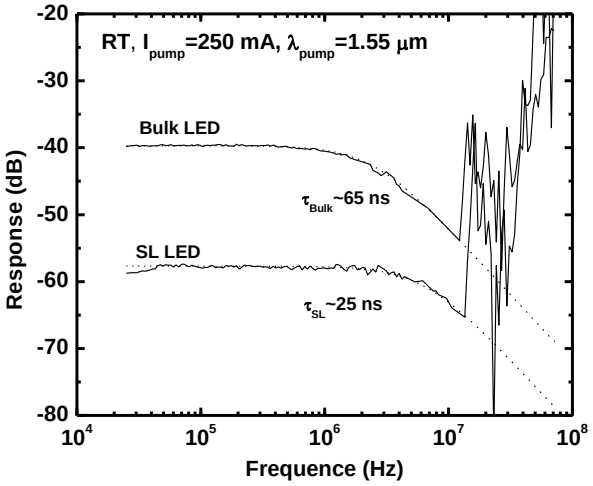

Figure 2.39 The optical modulation frequency response for each LED at RT. The minority lifetime for the bulk (τ_{Bulk}~65 ns) and SL (τ_{SL}~65 ns) LED was obtained by fitting the measured graph (solid) with the transfer function (dot) from [51].

We have demonstrated GaSb based MIR LEDs using Bulk InGaAsSb and type II InAs/GaSb SL active region. The grown LEDs, composed of the same double heterostructures except for the active region, emitted at 4.05 μm from Bulk and 4.25 μm from SL at 300 K. Bulk LED generated optical power of 80 μW (0.72 mW) and SL LED generated that of 65 μW (0.55

mW) at 300 K (77 K). The twenty percent smaller internal efficiency of the SL LED was attributed to the twofold shorter lifetime limited by the SRH recombination. No distinguishable difference on temperature dependence of optical power was observed between them according to the similar value of T_1 of 100 K. Similar optical power and temperature dependence of both LEDs proved that application of SL active region would be suitable for long wavelength high power LEDs.

2.5.4.2 Type II InAs/GaInSb superlattice LED emitting near 8 μm

Interband LEDs based on the type II interface showed promising performance that can be utilized for the IRSP applications. Das *et al.* demonstrated InAs/GaInSb/AlSb based interband cascade LEDs emitting at 7 μm with optical power of 22 μW at 77K [52]. Koerperick *et al.* recently demonstrated type II GaSb/InAs SL LEDs emitting at 8.4 μm [25]. Impressive qCW power of 600 μW at 77 K emitted from the mesa area of 520×520 μm^2 has been achieved using active region cascading of 16-stages without substrate thinning and polishing.

As we discussed in Section 2.5.1, active region cascading is a desired strategy to achieve high optical power at a given bias current. However, to exploit full advantages of the cascading scheme, several important parameters have to be optimized:

1) Thickness of a stage concerning carrier transport along the SL interface
2) Tunnel junction that can minimize voltage consumption
3) Total number of cascading concerning trade-off between carrier diffusion and emitting volume.

Table 2-2 The list of superlattice active regions to investigate hole transport.

<table>
<tr><th rowspan="2">LED</th><th colspan="2">InAs/$Ga_{0.75}$InSb SL active</th><th rowspan="2">n-clad</th><th rowspan="2">p-clad</th></tr>
<tr><th>(Å/Å × period)</th><th>(cm^{-3})</th></tr>
<tr><td>1</td><td>27/18 × 25</td><td>undoped</td><td rowspan="5">GaSb (500 nm)
Te:5×17 cm^{-3}</td><td rowspan="5">$In_{0.1}GaAs_{0.09}Sb$ (200 nm)
Be: 1×18 cm^{-3}
$In_{0.1}GaAs_{0.09}Sb$ (200 nm)
Be: 2×19 cm^{-3}</td></tr>
<tr><td>2</td><td>27/18 × 25</td><td>1×10^{17}</td></tr>
<tr><td rowspan="2">3</td><td>21/18 × 10</td><td rowspan="2">undoped</td></tr>
<tr><td>27/18 × 15</td></tr>
<tr><td rowspan="2">4</td><td>18/18 × 10</td><td rowspan="2">undoped</td></tr>
<tr><td>29/18 × 15</td></tr>
</table>

To optimize the thickness of one stage, i.e. the numbers of SL periods, four SL LEDs were compared with heterostructures summarized in Table 2-2. All SL LEDs nominally have the

same n- and p- cladding layers except for the SL active region. The wavelength of InAs/$Ga_{0.75}$InSb SL has been controlled by changing the InAs thickness while the GaInSb was fixed at 18 Å for all LEDs, resulting in consistent energy level quantization of heavy holes along the SL. The narrower the InAs thickness is, the shorter the wavelength can be expected. Application of the GaInSb instead of GaSb over the SL active region can be beneficial with respect to strain compensation so that thicker active region may be achievable compared to InAs/GaSb active region. Note that the opposite strain polarity of InAs for the tensile strain of 0.6% and $Ga_{0.75}$InSb for the compressive strain of 1.6% against to GaSb. The bandgap of InAs/$Ga_{1-x}In_xSb$ SL significantly decreases as the indium content increases. This is due to the increased strain that decreases the conduction band edge of InAs and increases the heavy hole band of $Ga_{1-x}In_xSb$ [35].

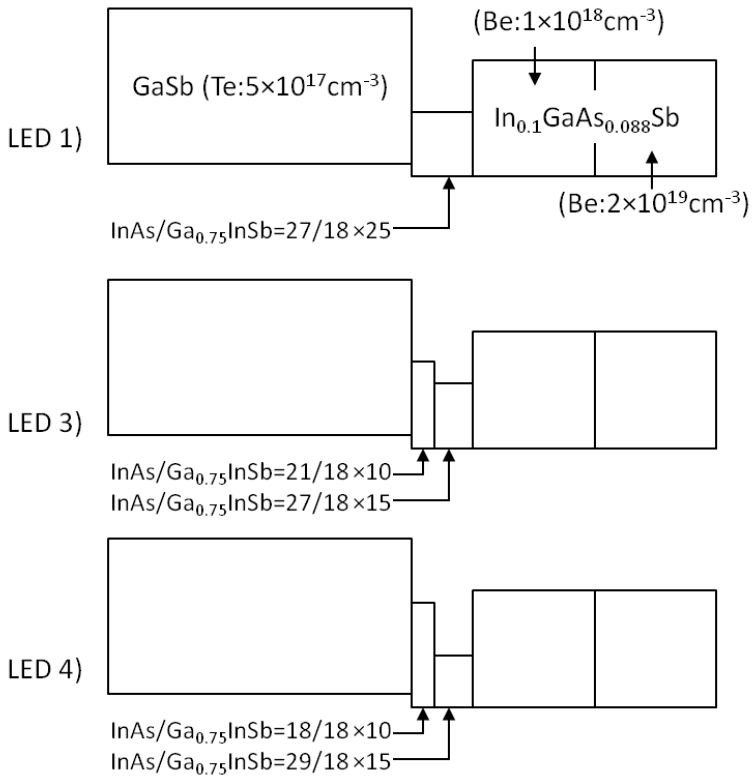

Figure 2.40 Schematic band diagram of LED 1, 3, and 4. Only bandgap energy of the SL is shown.

Assuming the holes are localized in the GaSb wells, one can consider p-type doping on the active region to improve hole conduction. In comparison between LED 1 and 2, the effect of the p-type doping on the LED performance can be checked. SL with the narrow InAs layer was

inserted in the active regions of LED 3 and 4 to investigate the hole transport. If holes are injected close to the narrow InAs SL, we may observe two different peaks from the LEDs. Thus, presence or intensity strength of the shorter wavelength peak can provide a reference to justify the hole transport. We estimate the peak of 4–5 μm from the 21Å thick InAs and the peak of 7–8 μm from the 27 Å thick InAs. To facilitate the hole injection, the final layer of the SL was terminated with GaSb at the interface between SL and p-cladding for all LEDs. Band diagrams that only display superlattice bandgaps, the minimum at the conduction mini-bands and maximum at the heavy hole mini-bands, are illustrated in Figure 2.40.

All LEDs were fabricated with the same manner. Light was emitted through the n-type GaSb substrate, which was thinned down to 200 μm. Electroluminescence (EL) of each device having 9-pixels with the pixel size of 120×120 μm^2 was measured at 80 K under qCW (10 kHz, 50%) bias current.

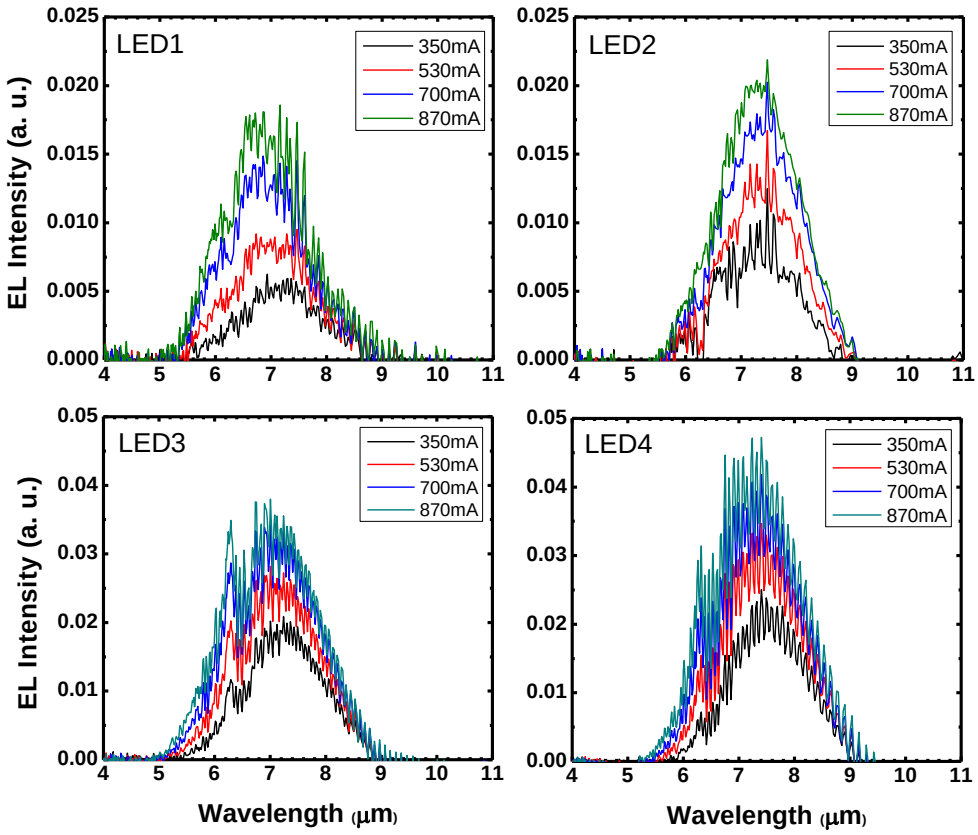

Figure 2.41 Electroluminescence of all LEDs measured at 77 K under qCW (10 kHz, 50%) mode.

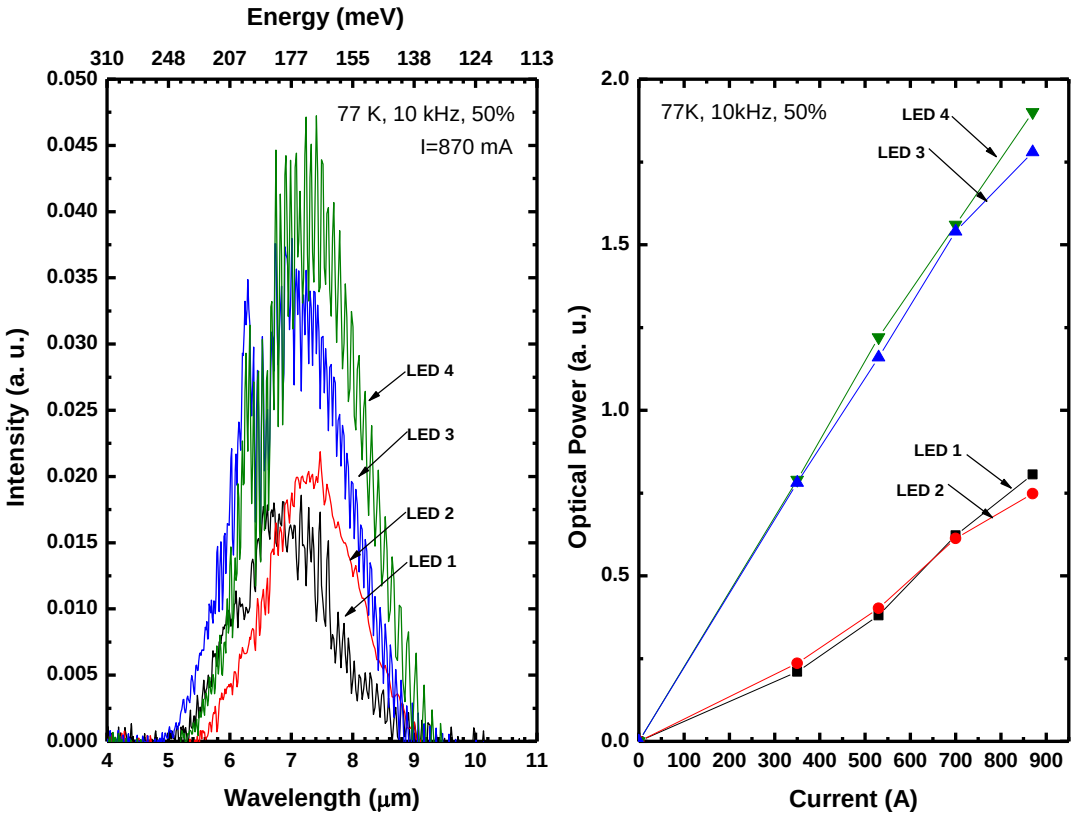

Figure 2.42 Electroluminescence of all LEDs measured at 870 mA and relative optical power.

Figure 2.41 shows the EL of all LEDs measured at the same bias condition and temperature. LED 1 and 2 emitted at the peak wavelength of ~7.5 μm. EL intensity of LED 2 is about 10 % higher than that of LED 1 but within a range of device and measurement variation. Thus, we may conclude that the p-doping in the active region does not introduce any pronounced change on LED performance. Most significant result of this experiment is presented in the bottom two graphs of Figure 2.41. The short wavelength peaks were not observed from any of LED 3 or 4. The long wavelength peaks are corresponding to LED 1 and 2 but nearly twice higher intensity compared to LED 1 and 2 though LED 3 and 4 have smaller active region volume than those of LED 1 and 2. Concerning the enhanced Auger recombination rate in long wavelength, the fact that smaller active region volume generated higher intensity is counterintuitive unless the hole injection is significantly non-uniform. Further analysis shown in Figure 2.42 demonstrates the EL of all LEDs measured at 870 mA and relative optical power

obtained by integrating the EL intensity. LED 3 and 4 generated about 2.5 times higher optical power than LED 1 and 2. These results suggest following conclusions. First, valence band holes seem to have a bottleneck near the interface between SL and p-cladding layer or limited transport through the narrow gap SL so that the short wavelength 2nd peak was not observed from LED 3 and 4. Second, twice-higher optical power of LED 3 and 4 than that of LED 1 and 2 is possibly due to better electron confinement in the narrow gap SL region since the mini-band gap of the wide gap SL will act as a potential barrier of the narrow gap SL. From the fact that optical power of the LED 3 and 4 was not saturated, we can consider even less number of periods of the narrow bandgap SL to increase the radiative efficiency.

2.5.5 High dimensional addressable LED arrays

Infrared scene projection (IRSP) is a technique to generate images that are used in the characterization of IR detection systems. Stringent specifications, such as high apparent temperature, high resolution, and high modulation speed, are required from the IR emitter array to fulfill effective scene projection. Various approaches have been utilized in IRSPs including IR resistor arrays [53] and digital micro mirror devices (DMDs) [54]. They, however, seem to suffer from either limited modulation speed or apparent temperature, which severely limits frame rate and dynamic range of the IRSP system. For a next generation IRSP application, great attention has been paid to MIR LED arrays since they can offer high radiance, high modulation speed, and the potential for spectrum control. This section presents the novel pixel design that can be effectively employed in low to high dimensional addressable LED arrays, together with detail of fabrication procedure and characterization results.

We utilize the flip-chip bonding scheme that essentially requires both n- and p- contact placed at the same epi-side to be bonded with a read in integrated circuit (RIIC). To form the separate contacts, each LED pixel has to be isolated by etching grooves between them. In demonstration of the prototype 6×6 array, as illustrated in Figure 2.43(b), the conventional non-etched LEDs were compared to investigate the effect of current spreading on the array performance. The heterostructure for LED arrays emitting near 3.3 μm - 3.7 μm is based on the type I QW active region with the quinternary barrier layers.

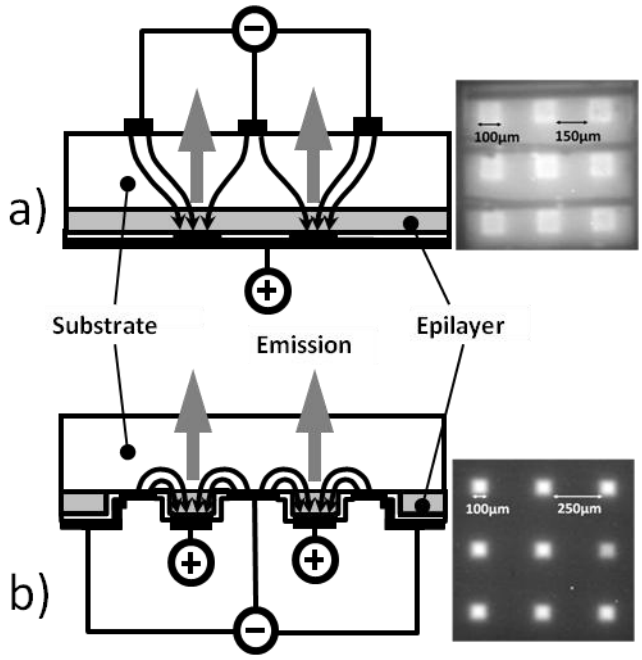

Figure 2.43 Schemes and MIR images of non-addressable (a) and addressable (b) LED arrays.

Figure 2.43(a) shows an array with the pixels formed by 100 μm ×100 μm rectangular windows in the dielectric that separated the metal contact from the epi-layer of the structure without etching grooves. In spite that we used a common metallization for all the array pixels, this design can be easily transformed to the addressable arrays by depositing a separate contact for each pixel. The addressable array pixels with the 100 μm×100 μm rectangular mesas formed by etching 200 μm-wide grooves down to the buffer layer (Figure 2.43(b)). After etching, the structure was covered with silicon nitride. The windows for the contacts were opened on both the top of the mesas and the bottom of the groove. Contact deposition of Ti and Au was followed by a liftoff process. The wafer was thinned down to 150 μm and cleaved. To check the array operation a simple read-in circuit was made by deposition of titanium and gold layers on dielectric coated silicon wafer (Figure 2.44(a)). The read-in circuit geometry allowed individual addressing to all 36 pixels of the prototype array. Electroplating was used to deposit 3 μm thick indium bumps onto the contact pads of the read-in circuit. The array die was flip-chip bonded onto the read-in circuit (Figure 2.44(b)).

MIR pictures of some of the working LEDs are shown in right side of Figure 2.43. Better contrast between the pixels and the background is observed from the etched array. In the array with no etched grooves, current spreading leads to emission from the area between the pixels. The effect of current spreading in a diode structure is qualitatively described within a simplified

model that includes an infinite plane metal contact at the substrate side and a half-plane metal contact at the epi-layer side. Current is injected into the half-plane epi-layer contact, while the upper cladding layer works as a current spreading layer. Under the metal contact, the current density is J_0 and the current flows normal to the p-n junction plane. Away from the contact edge, the current density in the normal direction decreases and an in-plane current component appears in the structure. The current density as a function of lateral distance to the contact edge, *x*, is given by [55],

$$J(x) = \frac{2J_0}{(x/L_c + \sqrt{2})^2}, (x>0) \qquad 2\text{-}19$$

, where

$$L_c = \sqrt{\frac{dn_i kT}{\rho J_0 e}} \qquad 2\text{-}20$$

Here d is the thickness of the upper clad, ρ is the resistivity of the upper clad and n_i is the diode ideality factor. The voltage drop across the p-n junction increases current spreading and works similarly to current-blocking layers in LED design [56]. The current spreading length L_c depends on the current density J_0. The estimations made for the presented LEDs give L_c ranging from ~ 15 μm (J_0 .= 1000A/cm^2) to 150μm (J_0.= 10A/cm^2). At low current densities, the current spreading length is of the order of distance between the pixels, which leads to the reduction of the contrast between working pixels and the background. In addition, pixels with distance smaller than the current spreading length will suffer from crosstalk between pixels. This effect is eliminated by etching grooves between the pixels.

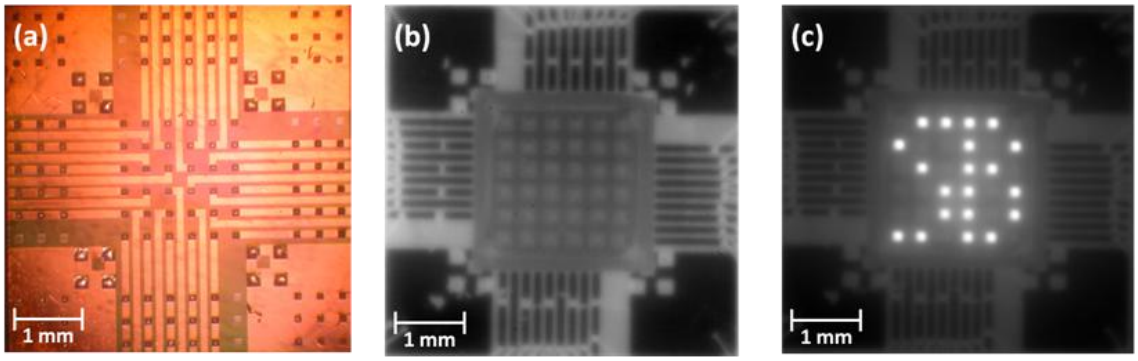

Figure 2.44 Read-in circuit for the prototype 6×6 array (a); MIR images of the operating 6×6 array without bias (b) and under total bias current of 54 mA (c).

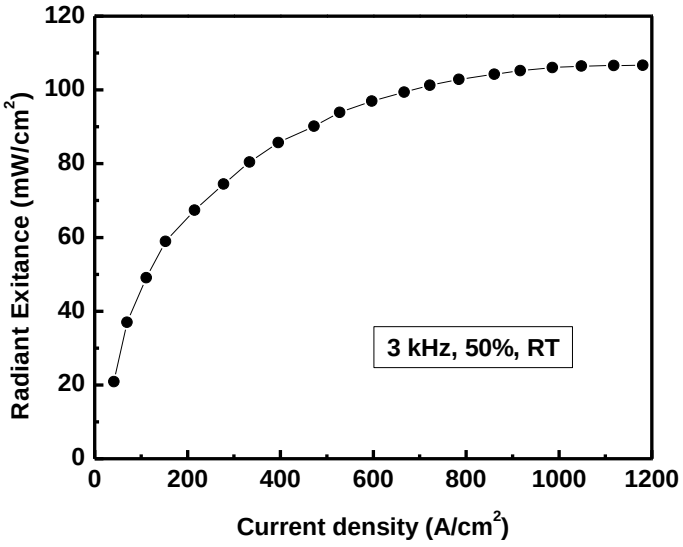

Figure 2.45 The radiant exitance measured on 9 pixels of the 6×6 array as a function of current density under qCW (3 kHz, 50%) mode at room temperature for 3.66 μm LED.

Figure 2.44(c) shows a room temperature MIR image of a working 6×6 addressable LED array. The bias current was ~2 mA per pixel. A radiant exitance of 100 mW/cm^2 was obtained by measuring the emission power of 9 array pixels (Figure 2.45). This is lower than the corresponding value obtained from an individual LED with the same area. A possible reason for this reduction is reduced thermal conductivity of the array due to the improvised silicon read-in circuit.

Similar design principles were applied to 512×512 addressable arrays operating at the wavelength of 3.3 μm. The scheme of the pixel contacts for the addressable LED array is presented in Figure 2.46. The array pitch is 48 μm. To facilitate flip-chip bonding, both the anode and common cathode contacts were placed on the top of each mesa. A smooth mesa sidewall is required to ensure continuity of the deposited metal film that connects the n-contact in the etched groove to the mesa top. To control the shape of the mesa walls, two etching solutions with different selectivity [57] were used to etch the grooves. By adjusting the ratio of etching times, almost vertical mesa walls were obtained (Figure 2.47(b)). The etching is highly uniform and the etched surface is smooth (Figure 2.47(a)). After etching and deposition of the p-contacts and n-contacts, the wafer was coated with dielectric. Final metal was deposited after

opening windows in the dielectric. The array was lapped down to 200 μm, polished, and cleaved out of the wafer. The final size of the 512×512 array is 2.5 cm×2.5 cm (Figure 2.48).

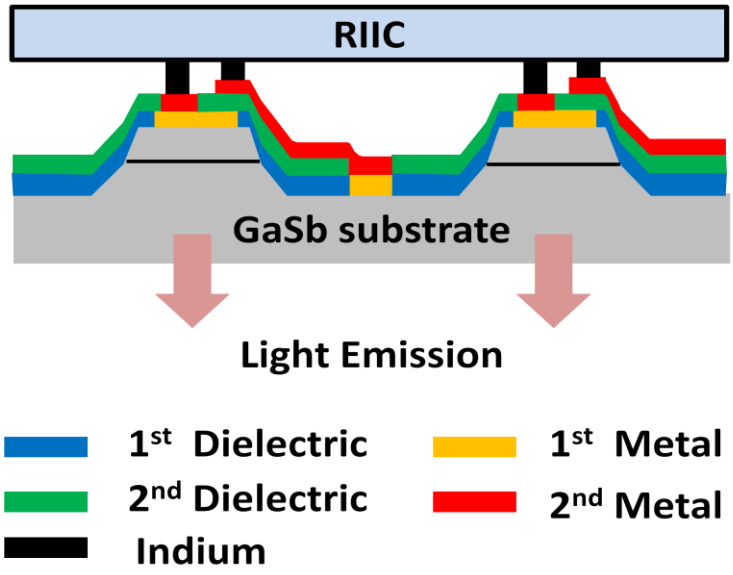

Figure 2.46 The pixel layout for the 512×512 LED array.

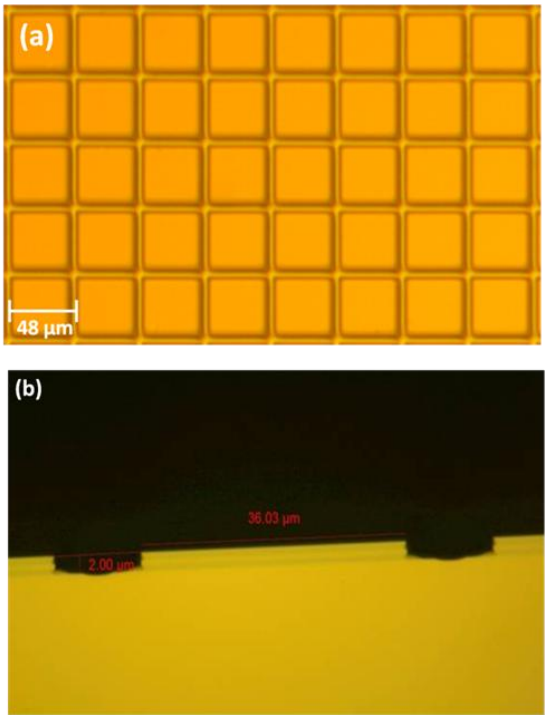

Figure 2.47 Fragment of 512×512 array after groove etching (a) and pixel mesa walls (b).

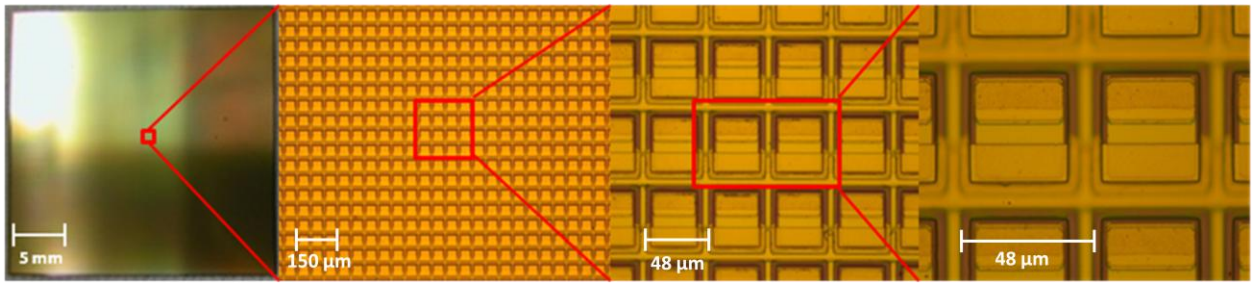

Figure 2.48 Completed 512×512 addressable LED array at several different magnifications. Both anode and cathode contacts are on the top of each mesa.

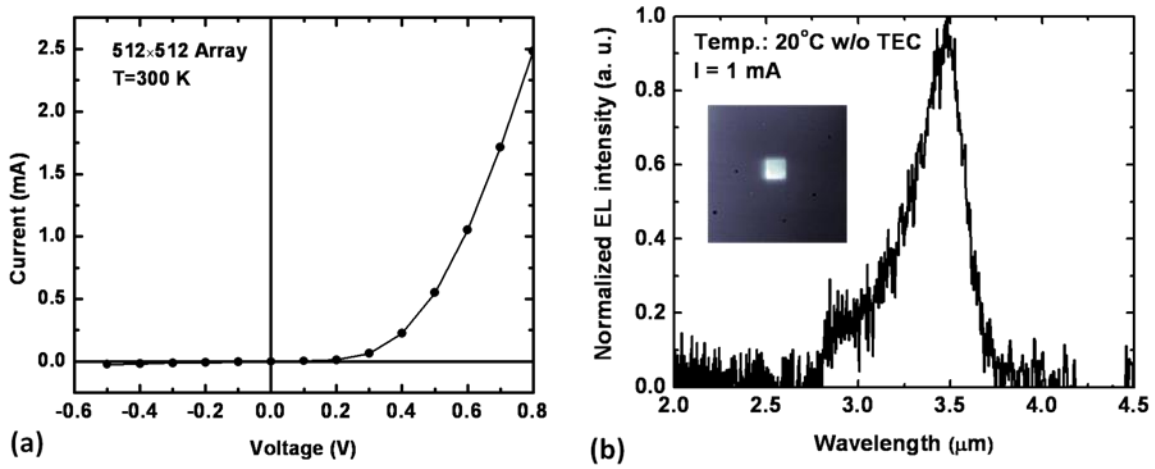

Figure 2.49 Current versus voltage characteristic (a) and emission spectrum (b) of a 512×512 array pixel. The inset of the right panel is the MIR image of a working array pixel.

To check the operation of the array pixels, we used a workstation with tungsten needle probes. One hundred pixels were picked randomly at the corners and center of the array. All measured pixels demonstrated diode current versus voltage characteristics similar to those shown in Figure 2.49(a). The low opening voltage indicates high contact quality. A MIR image of an operating pixel is shown in the inset of Figure 2.49(b). The emitting area has sharp edge, which indicates to the absence of current spreading and crosstalk between the pixels. The emission spectrum of an operating array pixel is shown in Figure 2.49(b).

2.5.6 Dual wavelength LEDs and LED arrays

The LEDs generating a single peak wavelength have been discussed so far. In this section, the LED and LED array that can exhibit two independently controlled wavelengths at 2

μm and 3 μm are resented. Such dual wavelength emitters can be utilized in multi-spectral or hyper-spectral imaging systems as well as a gas sensor requiring both a sensing and reference channel within one device.

The development of dual wavelength LEDs has mostly been demonstrated in the visible spectral range. Ozden *et al.* [58] have reported a dual wavelength LED emitting at 470 nm and 535 nm using an InGaN multiple quantum well (MQW) structure. Dual wavelength lasers have been fabricated and demonstrated by D. Sun *et al* [59]. The wavelengths for red (670 nm) and infrared (840 nm) emission were obtained from InAlGaAs/AlGaAs QWs grown on GaAs substrates using an etching and selective re-growth technique. In the MIR range M. Aidaraliev *et al.* demonstrated liquid phase epitaxy grown LEDs which emit simultaneously at 2.1 μm and 3.6 μm at 300 K with p-GaInPAsSb/p-InAs/n-InAs material system [60].

A dual wavelength LED structure was designed to independently control the intensities of each color. The band diagram of the dual wavelength LED structure is presented in Figure 2.50(a). The device comprises two LED sections grown on the same wafer and separated by a p-doped GaSb contact layer so that the grown structure is essentially same as the n-i-p-i-n configuration. The "color" intensities are controlled separately through the application of bias voltages between the top layer and the substrate with respect to the middle contact layer. Each active region is corresponding to those of the type I QW LEDs introduced in the previous section.

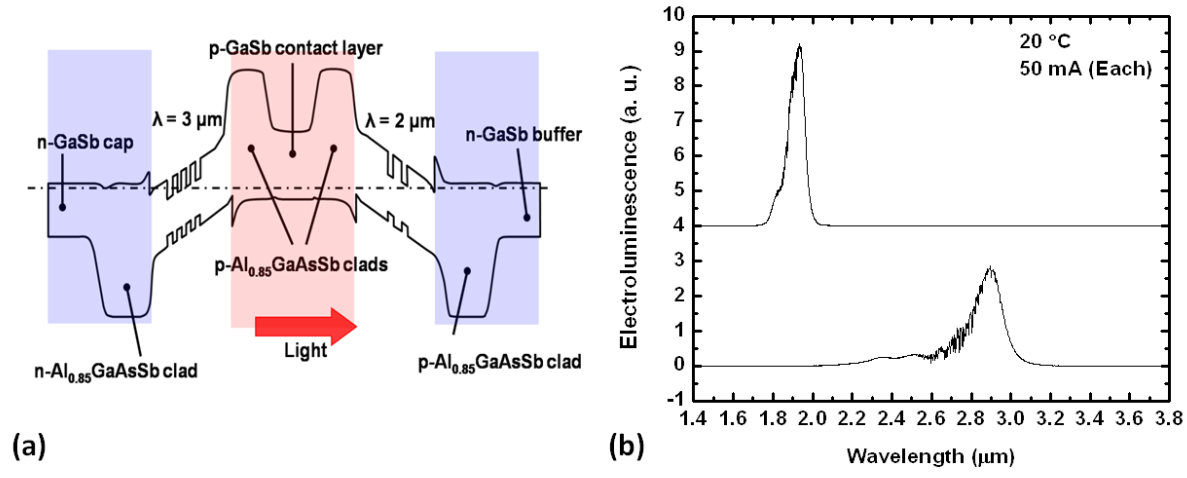

Figure 2.50 The band diagram of the dual wavelength LED and (b) EL spectra.

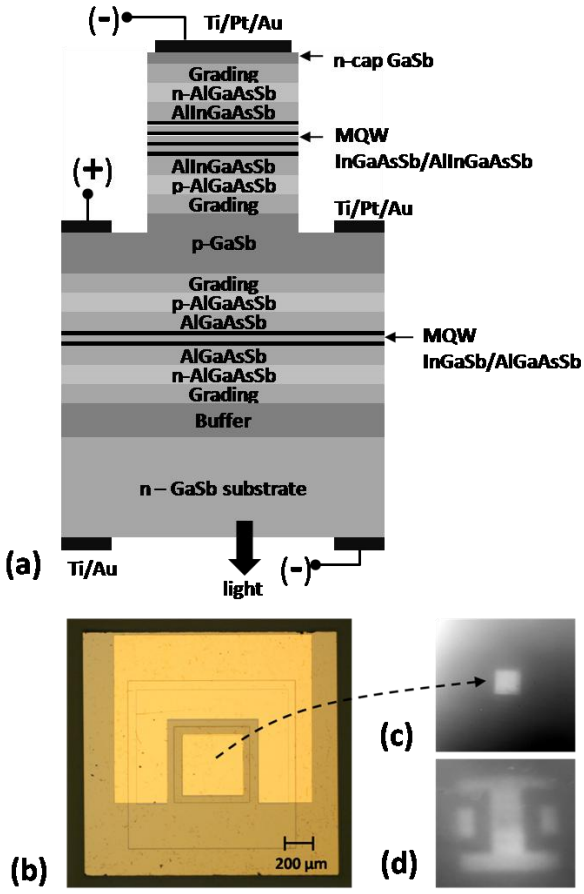

Figure 2.51(a) The structure of the dual wavelength LED. (b) The completed dual wavelength LED device. Infrared images for (c) the top LED ($\lambda = 3$ µm) and (d) bottom LED ($\lambda = 2$ µm).

A schematic of the LED structure is shown in Figure 2.51(a). Since we intended to collect light through the substrate, the longer wavelength active region was grown top of the shorter wavelength structure that will be nearly transparent for the long wavelength. The bottom LED structure was grown on a 5000 Å thick GaSb buffer layer. Tellurium (Beryllium) doped AlGaAsSb n (p)-cladding layer with the thickness of 2000 Å enclosed the active region. InGaSb QW and AlGaAsSb barrier layer with the thickness of 120 Å and 200 Å were designed to emit at 2 µm. A 15000 Å thick Beryllium doped GaSb layer in the middle of the structure was grown to form the electrical contact for the bottom LED. The top LED was designed to emit at 3 µm from an active region composed of compressively strained (~0.9 %) four InGaAsSb QWs (130 Å) and AlInGaAsSb (500 Å) barriers. Conventional lithography and wet etching were used to define the 500×500 µm^2 square mesa. The etching was stopped after removing the p-cladding layer of the top LED. The metal contact for the bottom and top LED structure was formed by Ti (200 Å) / Pt

(1000 Å) / Au (2000 Å), while the contact for the substrate was formed by Ti (200 Å) / Au (2000 Å) after thinning the substrate to the thickness of 200 μm. The LED sample was cleaved as 1.5×1.5 mm^2 devices and those were flip-chip bonded (the top LED is close to the sub-mount.) onto silicon sub-mounts using indium foil.

Figure 2.52 shows the current-voltage characteristic for each top and bottom LED. Each curve has been measured independently by applying quasi-continuous wave (qCW) current mode at room temperature. The p-contact was connected to the common ground and two n-contacts were connected to the negative terminals of two different power sources. The higher series resistance of the top LED is possibly due to the smaller contact area compared to the bottom LED (Figure 2.51 (b)).

The electroluminescence (EL) of the dual wavelength single LED was measured at room temperature (Figure 2.50(b)). The intensities of two emission peaks positioned at 2 μm and 3 μm can be controlled independently. The wider emission peak of the top LED (λ=3 μm) may be due to higher non-uniformity of the longer wavelength material. The distortion of the emission pattern near 2.7 μm is due to water absorption. The peak near 2.35 μm is the light emission from the second quantized level in the conduction band to the valence band, regarding the energy separation about 100 meV from the QW thickness of 13 nm. Infrared images for each LED are shown in Figure 2.50(c)-(d). Since no additional etching was done to define the light emitting area of the bottom LED, the emitting area of the bottom LED corresponds to the die size with a "c" shape dark area created by the metal contact of the substrate.

The dependence of optical power of each LED vs. bias current is shown in Figure 2.52. The bottom LED (λ=2 μm) produced the optical power as high as 2.8 mW under qCW (3 kHz, 50%) and 8.5 mW under pulsed (3 kHz, 1%) mode at room temperature. For the top LED (λ=3 μm), powers of 0.14 mW and 0.32 mW were obtained under qCW and pulsed mode, respectively. A possible reason for saturation of the power is device heating due to limited thermal conductivity of the silicon sub-mount. This effect is more pronounced for the bottom LED since a heat sink is farther from the bottom LED (λ=2 μm) than the top LED (λ=3 μm). Hole hetero-barrier leakage can also contribute to the rollover of the output power at high current injection. However, it is expected that this effect is suppressed in LEDs with AlInGaAsSb barriers.

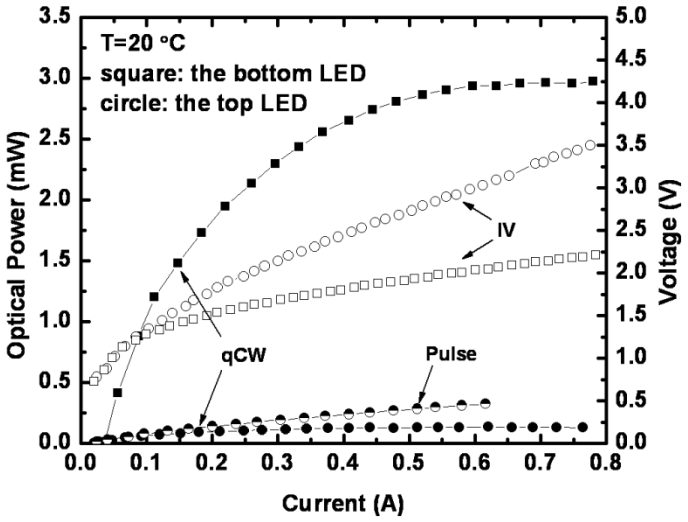

Figure 2.52 LIV characteristic for the dual wavelength LED. Closed and half closed symbol for the optical power versus current under qCW (3 kHz, 50%) and pulsed (3 kHz, 1%) mode operation, respectively. Open symbol for the voltage versus current.

Slight crosstalk between two wavelengths was observed as the two sections of the dual color LED were driven at the same time. Possible explanation for this phenomenon includes cross-heating between the device sections as well as current leakage and corresponding cross-injection of the charge carriers from one section to the other section. The effect is minor and does not affect the independent control of the wavelength intensities.

One of the advantages of the present dual wavelength LED structure is that it allows monolithic integration of LEDs operated at different wavelengths. We can consider two possible approaches to fabricate dual color arrays. The true dual color array can be realized by forming three terminals for each pixel, which can be realized by etching twice for middle and substrate contact. However, it was not compatible with an existing read in integrated circuit so that we rather fabricated two different kinds of LED pixels on one substrate (Figure 2.53(a)) by sacrificing half resolution for each wavelength. One type of pixel emitted at 2 μm, and the other operated at 3.4 μm. The device structure used for this LED pixel is the same as the above structure except for a reduced As content in the InGaAsSb QWs, resulting in the compressive strain of ~1.5 %. The device is presented schematically in Figure 2.53(a). To fabricate the pixels emitting at 2 μm we etched the "3.4 μm" section down and stopped the etching at the GaSb contact layer. For the pixels emitting at 3.4 μm we deposited the metal layer (Ti/Au) to shunt the

"2 μm" section. MIR images and EL spectra of working pixels for each wavelength are presented in Figure 2.53(b).

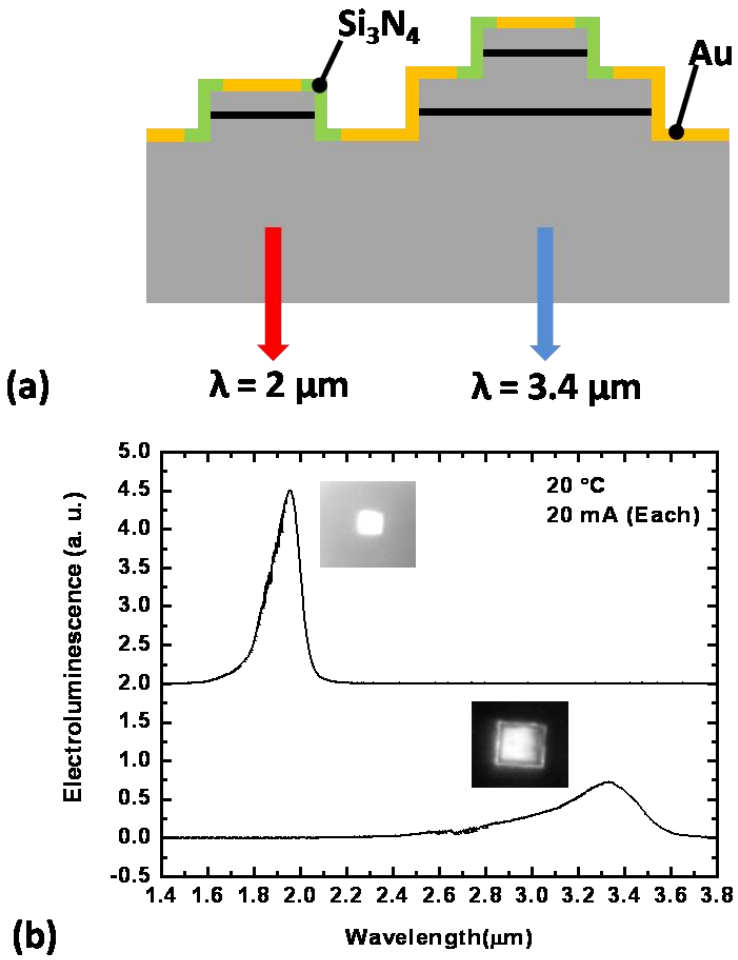

Figure 2.53 (a) Scheme of dual wavelength LED arrays and (b) EL spectra of 2 μm and 3.4 μm LED pixels with infrared images.

We have designed and fabricated the dual wavelength LEDs with the independent control over wavelength intensities. The optical output power for the qCW operation at room temperature was 2.8 mW and 0.14 mW for the wavelength of 2 μm and 3 μm, respectively. We also demonstrated the possibility of the monolithically integrating LED arrays with different wavelengths, which opens the way for the fabrication of addressable LED arrays for multi-spectral and hyper-spectral imaging applications.

2.5.7 Light extraction

The light obtained from the demonstrated LEDs is below 3% of light generated in the active region. Most of the light is merely trapped inside the LED structure where total internal reflection and absorption process is dominant. This is the consequence of the high refractive index of semiconductors, geometrical shape of LEDs, and random nature of spontaneous emission. Modification of such factors has been proposed to enhance the extraction efficiency using various approaches: micro-lens [61], substrate removal [62], surface texturing [63], anti-reflection (AR) coating [64], photonic crystal slab [65], and micro-cavity [66]. Concerning mechanical stability and practical simplicity, we have chosen the AR coating and surface patterning method that are applied to the GaSb substrate. Two LEDs were used to test each method: the AR coating for QW LEDs emitting at 3.7 μm and surface patterning for bulk LED emitting at 4.1 μm.

2.5.7.1 AR coating

The AR coating is applied to increase Fresnel transmission in direction of normal to the surface. Assuming that the multi-reflection between the top and bottom LED surface does not contribute to significant light emission, one can expect the maximum power increase of 30% taking into account the refractive index of GaSb of 3.8. The AR coating consisting of 10 nm thick Y_2O_3 and 400 nm thick Al_2O_3 was deposited on the fully processed LED surface using the E-beam deposition system. Then, the coating was partially etched to open window for n-contacts by the diluted hydrogen fluoride etchant (HF:DI=1:2) having the etching rate of ~100 nm/30 s. The reflectance of ~5% at the peak wavelength of the LED (λ=3.7 μm) was measured using the FTIR equipped with a Seagull reflectance accessory. The bandwidth of the AR coating was sufficiently wider than that of the LED, which did not introduce any signal loss.

Figure 2.54 displays the normalized near-field intensity along the lateral direction and IR image taken at room temperature. The near field was measured using nitrogen cooled focal plane array IR camera. As one can see, the clear difference of contrast is observed between the uncoated and coated LED. The contrast, defined as the peak intensity over the background intensity, is estimated 1.25 and 2.85 for the uncoated and coated LED, respectively. The low contrast in the uncoated LED is possibly because effective optical area becomes wider as light experiences scattering through the multi-reflection process. However, such twofold improvement

in the contrast did not make any difference on optical power. Figure 2.55 shows optical power of both LEDs as a function of current measured at the same condition (RT, 3 kHz, 50%). The nearly same power may be attributed to that; the reflected photons do not experience significant absorption through the thin active region so that most of them escape to free space via the multiple reflection process. This situation can be supported by the electroluminescence measurement. As shown in Figure 2.56, the Fabry-Perot fringes in the uncoated LED indicate the presence of multiple reflection between the GaSb surface and metal contact on the epi side. For the coated LED, the decreased finesse shows the increased Fresnel transmission but total emission power, in turn, similar to the uncoated one. Thus, AR coating is not effective in terms of optical power but effective for improvement of contrast.

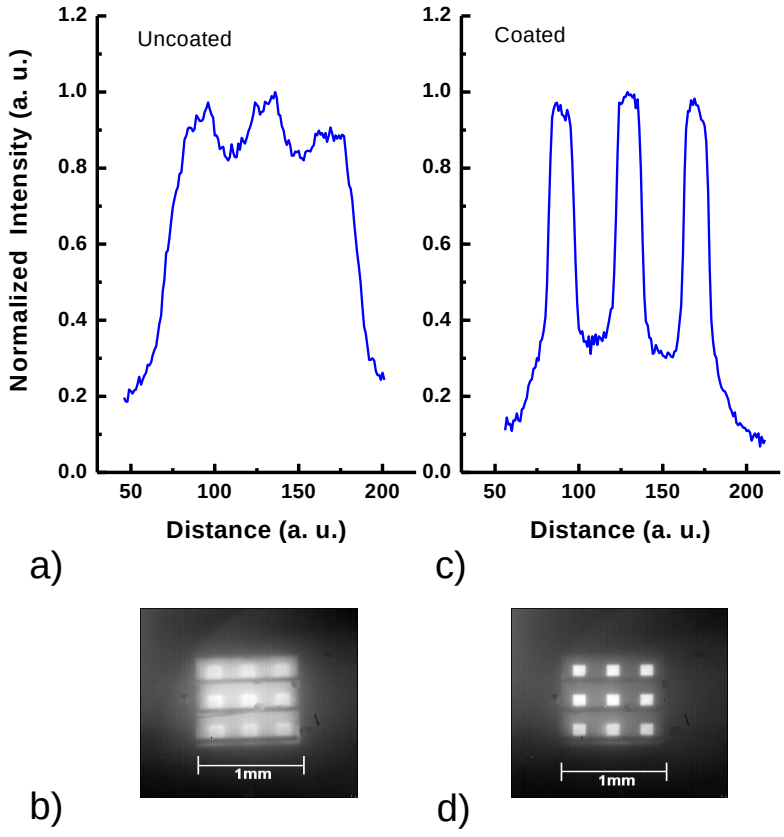

Figure 2.54 Normalized near-field intensity and IR image of the uncoated (a, b) and coated LED (c, d) measured at room temperature under CW current of 20 mA.

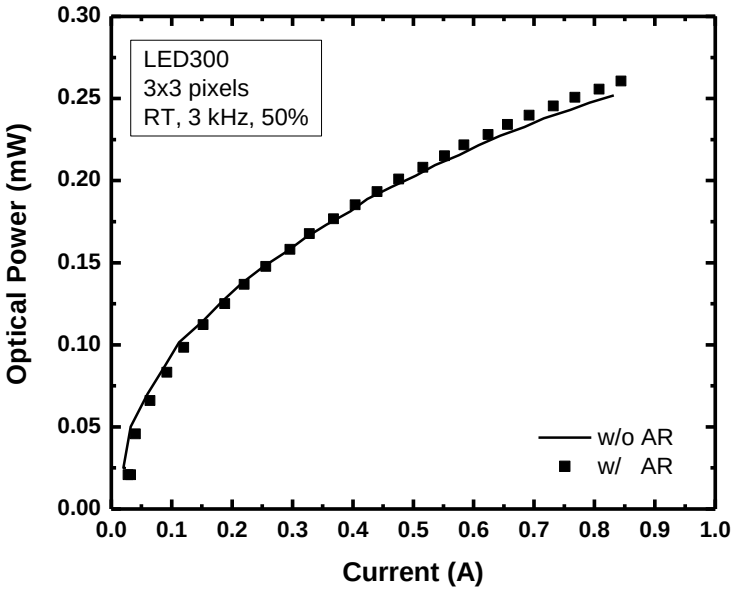

Figure 2.55 Optical power of the uncoated (line) and coated (symbol) under qCW mode (3 kHz, 50%) at room temperature.

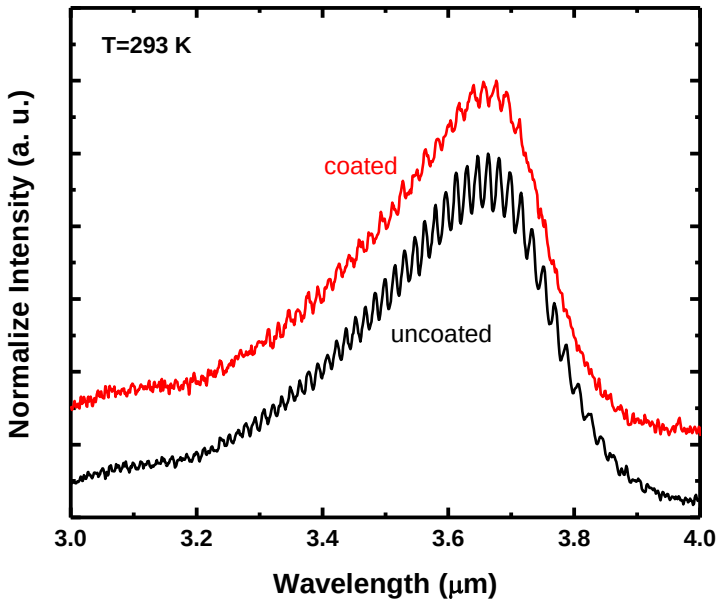

Figure 2.56 Normalized electroluminescence of the uncoated and coated LED.

2.5.7.2 Surface patterning

The surface patterning with small features, compared to the emitting area of a LED, is a convenient method that does not require sophisticate alignment to match optical axis between the emitting area and surface pattern, such as micro-lens. In addition, the cost of fabrication will be inexpensive by using wet etching since the anisotropic profile of dry etching is not necessary. We patterned the GaSb surface using a mask consisting of 49 μm×49 μm squares with 51 μm pitch. Photoresist covered the n-contact stripes to avoid any damage from the etchant. The hydrochloric based solution was used (HCl:DI:H_2O_2 = 50:50:1) to etch the GaSb substrate. Figure 2.57 shows the side and top view of the etched surface with different times: 5 min and 10 min. The images were taken by a microscope with the Nomarski mode. The sidewalls of each pattern became gradual slope due to isotropic characteristic of wet etching and the etching depth was 2.1 μm and 2.8 μm for 5 min and 10 min etching, respectively. The small square top (~20 μm ×20 μm) of the sample etched for 5 min is disappeared in the one for 10 min due to etching in the lateral direction.

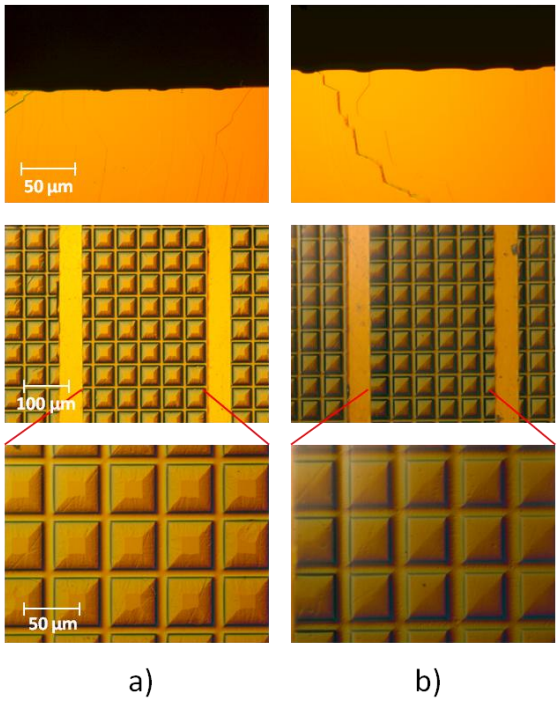

Figure 2.57 The micrographs of surface patterned LEDs with 5 min etching (a) and 10 min etching (b); top- side view; middle and bottom- top view with different magnifications.

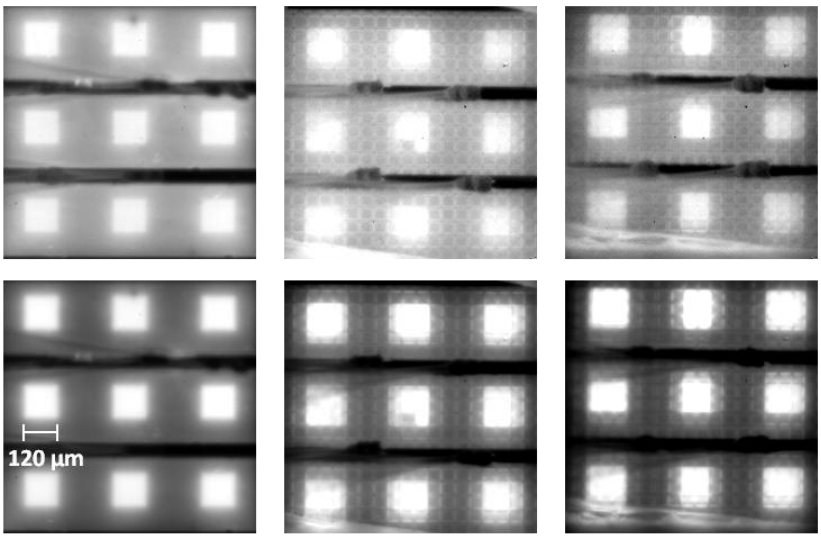

Figure 2.58 The IR images of non-etched (a), etched 5 min (b), and etched 10 min (c) LED under 10 mA (top) and 50 mA (bottom) CW current.

Figure 2.58 shows the IR images taken from the non-etched and etched samples. Each pixel has the size of 120 µm×120 µm and two horizontal black lines in the middle are the metal contacts on the substrate. The top and bottom images were taken under bias current of 10 mA and 50 mA, respectively. Comparing between the top and bottom images, one can observe that the contrast between the background and pixel is improved since current spreading is less pronounced as current increases. For the etched samples, more light emitted through the sidewall of the pixels but not from the groove center where the light experiences the same angle as the non-etched plane.

Optical power of each LED is plotted in Figure 2.59. As the etching time increases, optical power increases as high as 33% compared to the non-etched LED, resulting in 100 µW of qCW power from the LED etched for 10 min. We did not observe any change on I-V characteristics after etching. The surface patterning with etching depth of 2.8 µm did not introduce any difference on far field of the LEDs (Figure 2.60). Nearly identical patterns following the cosine function of the Lambertian source exhibit FWHMs of about 120˚.

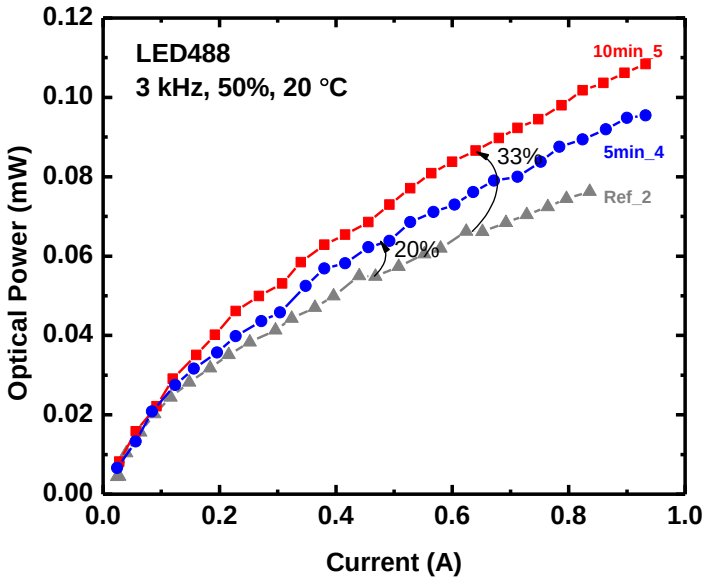

Figure 2.59 Optical power vs. current for non-etched (triangle), 5 min etched (circle), and 10 min etched (square) LED measured at room temperature under qCW mode.

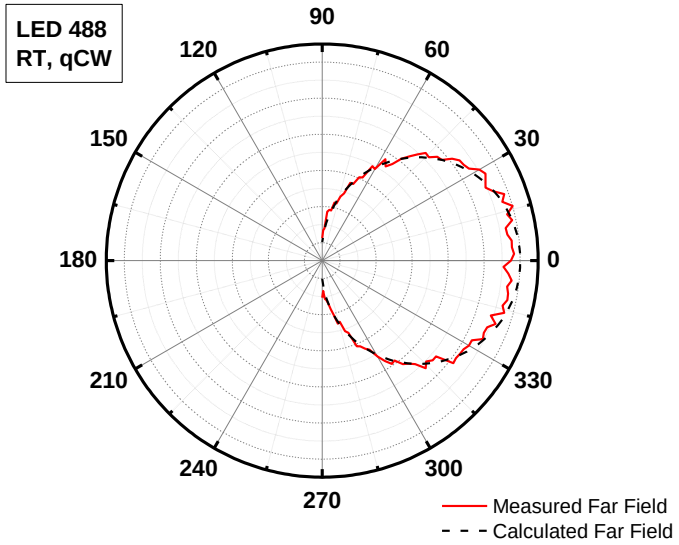

Figure 2.60 Measured (solid) and calculated (dashed) far field of the etched 10 min etched LED under qCW mode at room temperature. Far-field of the non-etched LED is identical to the one etched (not shown).

2.6 Conclusion and future work

We have demonstrated the state of the art GaSb based LEDs covering the spectral range from 2 μm to 8 μm. Application of strain engineering and new quinternary material into the active region of type I QW LEDs allowed for increasing the internal quantum efficiency more than twofold, resulting in the record power of 0.7 mW at λ~3 μm. The λ=2 μm LEDs using the active region cascading scheme generated record qCW power of 10 mW and the internal efficiency of 84% at room temperature. The InAs/Ga(In)Sb type II SL active region was used for the LWIR LEDs. It was experimentally demonstrated that only a few SL periods near the p-cladding contribute to the radiative recombination process, which may conclude that active region cascading with fewer periods will be more effective in the LED design with this type of the SL active region. Novel scalable pixel design and fabrication method realized highly dimensional LED arrays with 512×512 pixels and the independently controlled dual color LED arrays emitting at 2 μm and 3 μm. Application of anti-reflection coating on the LED surface showed the improvement of pixel contrast but with the nearly same output power, suggesting that the reflected light was not suffering from significant absorption but extracted via multi-reflection process. Improvement of 33% on optical power was achieved using the surface patterning on the LED surface. A new precise technique for calibration of LED power has been developed.

Radiant exitance of the GaSb based LEDs (the red color star symbol) presented in this chapter is summarized in Figure 2.61 together with the survey result that was shown at the beginning of this chapter. Again, the presented data shows performance of LEDs without modification for improvement of the extraction efficiency and performance measured at room temperature. Remarkably, one order of magnitude higher radiant exitance has been achieved at the spectral region near 3.0 μm – 3.3 μm, resulting in only LEDs capable to exhibit the apparent temperature of 1000 K under qCW mode. In the spectral region between 3.4 μm – 4.0 μm, threefold or at least 50% higher radiant exitance have been obtained.

To realize high apparent temperature LEDs at longer wavelength, the active region cascading scheme using the type II superlattice active region seems to be one of the best options. Based on the optimization process to determine the effective number of superlattice periods, we are developing cascade active region LEDs that will eventually be formed as high dimensional two-color arrays. In addition, application of the surface patterning on the back surface of the flip

chip boned LED array is expected to increase 50% of light extraction with increased etching depth.

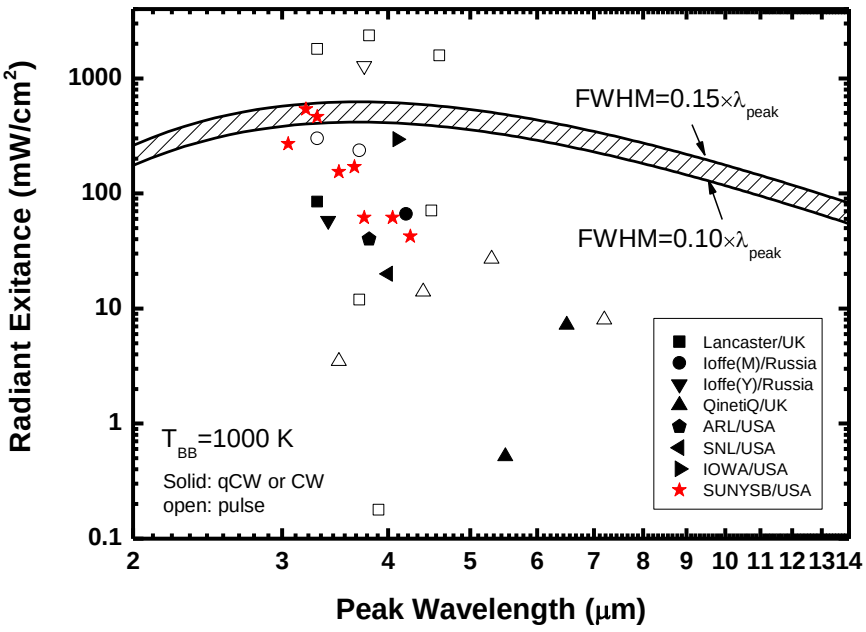

Figure 2.61 The radiant exitance of the MIR LEDs as a function of peak wavelength obtained from several groups. The crosshatched region indicates the corresponding to radiant exitance of a blackbody at 1000 K. The data only present results obtained at room temperautre. Closed symbols indicate qCW or CW mode and open symbols indicate pulse mode.

Chapter 3

Semiconductor lasers

3.1 Introduction

Laser is the abbreviation for light amplification by stimulated emission of radiation. Laser amplifies lights in a gain medium by means of positive feedback along a resonant cavity and emits coherent light out of mirror facets. If a semiconductor is used as the medium, the laser is called semiconductor laser. Depending on the configuration of the resonant cavity, the semiconductor lasers can be further classified as Fabry-Perot (FP) laser, vertical-cavity surface emitting laser (VCSEL), ring laser, etc.

Generation of lights in the gain medium can be achieved either by optical pumping or by electrical injection. In terms of compactness and portable operation, the electrical injection is preferred but additional requirements such as good transport and confinement of carriers in the active region have to be fulfilled. Figure 3.1 shows the energy band diagram of a typical type I QW laser. The laser diode is formed with a pn-junction that is similar to LED. At thermal equilibrium, the stimulated absorption is the dominant process rather than the stimulated emission, since the electron density in the valence band is much higher than that in the conduction band. As carriers are injected, the quasi Fermi level for electrons (E_{fn}) and holes (E_{fv}) moves upward (downward) so that population of electrons in the conduction band becomes higher than that of the valence band (population inversion). At this condition, the positive net gain can be achieved, which allows stimulated emission to be dominant process in a system. Especially, the condition that the optical gain and loss is the same, i.e. zero net gain, is called the transparent condition. When the optical gain reaches to a certain level, threshold gain, relatively sharp and coherent light emits out of the laser mirror with high degree of directivity, which is lasing oscillation or simply lasing.

The threshold current is one of the most important parameters of lasers. The current applied below the threshold current is merely idling current to satisfy lasing condition. Thus, a laser design should be aimed to minimize it. Light oscillating between two mirrors will be

amplified as propagating the gain media and simultaneously be absorbed, transmitted, and reflected. Competition between the modal gain and cavity loss is continued until the modal gain reaches the threshold gain. The threshold modal gain is expressed as,

$$g_{th} = \Gamma_c g = \alpha_i + \alpha_m \quad 3\text{-}1$$

, where g is the material gain, Γ_c is the confinement factor, α_i is the internal loss, and α_m is the mirror loss. The internal loss α_i is contributed by 1) free carrier absorption in the active and cladding layers, 2) inter-valence band absorption by transferring the photon energy into the electrons occupied in the light hole or split off band, and 3) scattering loss due to roughness of heterostructure and surface. The mirror loss is introduced by the transmission loss at the interface between mirror facet and air. Assuming that the cavity length is L and reflectivity at each mirror is R_1 and R_2, α_m is expressed as,

$$\alpha_m = \frac{1}{2L} ln\left(\frac{1}{R_1 R_2}\right) \quad 3\text{-}2$$

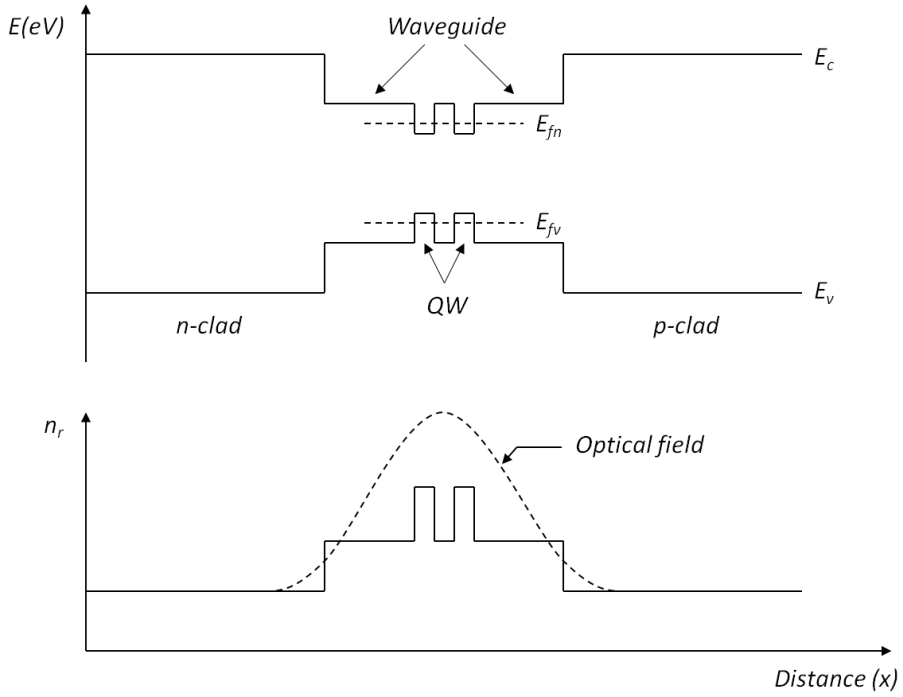

Figure 3.1 The schematic band diagram of the type I QW laser and associated refractive indexes with optical field.

The optical confinement factor is defined as the ratio of the integrated light intensity over the relevant layer to the total integrated intensity, expressed as,

$$\Gamma_c = \frac{\int_{x_1}^{x_2}|E(x)|^2 dx}{\int_{-\infty}^{\infty}|E(x)|^2 dx} \quad 3\text{-}3$$

, where x_1 and x_2 are the boundary positions of the relevant layer and E(x) is the electric field. The modal gain below threshold is typically characterized by using the Hakki Paoli method. Due to nature of spontaneous emission, random phase and broad spectral emission, only a small fraction of spontaneous emission that belongs to optical gain spectrum contributes to the lasing mode. Power spectrum of the amplified spontaneous emission manifests modulation of intensity in fringes caused by the Fabri-Perot resonance in the cavity. The modal gain can be estimated by taking the ratio of two nearby peak and valley as a function of energy.

Typical light-current characteristic of a laser shows a kink at the threshold current I_{th} and above the current, output power linearly increases in an ideal case. Laser power above the threshold current can be expressed as, concerning both mirror facets,

$$P_{out} = \eta_s(I - I_{th}) = \eta_{inj}\frac{h\upsilon}{q}\frac{\alpha_m}{\alpha_m + \alpha_i}(I - I_{th}) \quad 3\text{-}4$$

, where η_s is the slope efficiency in units of W/A, η_{inj} is the injection (or internal quantum) efficiency, $h\upsilon$ is the photon energy, q is the elementary charge. The injection efficiency η_{inj} is defined as the ratio of injected electrons and holes into the active region to total carriers injected into the system. Although it is also called as the internal efficiency, we shall not to use this term to avoid confusion with the internal efficiency of the LEDs. The differential (or external quantum) efficiency η_d can be expressed as,

$$\eta_d = \eta_s\frac{q}{h\nu} = \eta_{inj}\frac{\alpha_i}{\alpha_m + \alpha_i} \quad 3\text{-}5$$

. The laser performances mentioned above are governed by device temperature. As the temperature increases, the threshold current increases and the slope efficiency decreases. Empirical characteristic temperature T_0 for the threshold current and T_1 for the slope efficiency are expressed as,

$$I_{th} = I_{th0}\,exp\left(\frac{T - T_{th0}}{T_0}\right) \quad 3\text{-}6$$

$$\eta_s = \eta_{s0}\,exp\left(-\frac{T - T_{s0}}{T_1}\right) \quad 3\text{-}7$$

, where I_{th0} is the threshold current at the temperature T_{th0} and η_{s0} is the slope efficiency at the temperature T_{s0}. Thus, the higher the T_0 and T_1, the less the temperature dependence.

3.2 GaSb based single spatial mode lasers at 2.0 μm ~ 2.2 μm

Diode lasers operating in 2 to 2.2 μm spectral region are critical components for the development of systems for laser detection and ranging, spectroscopy, illumination, gas detection, medical diagnosis, etc [67-70]. High power GaSb-based type-I QW diode lasers operating in this spectral region generate watt level CW outputs at room temperature [71, 72]. However, the requirement of high power trade-offs the spectral purity and spatial beam quality that can be considered more important than the power for many applications.

Fabrication of the narrow ridge waveguide is a critical step to achieve single mode operation. Most of the narrow ridge lasers were fabricated using dry etching since it can provide precise control of etching depth and anisotropic non-selective etching directivity [57]. Wet etching has important advantages as an industrial process, such as simple implementation, low cost and high throughput. However, the lack of established and well-documented technology of anisotropic non-selective etching for the AlGaAsSb/InGaAsSb system makes application of wet etching into the narrow ridge fabrication unreliable [73]. One of the main challenges of the wet etching technique is precise control over the etching depth and ridge width: two parameters that are crucial for fabrication of single mode lasers. High material selectivity of most etchants used for GaSb based structures is an additional complication for the mesa geometry control. In this section, GaSb based spatial single mode lasers fabricated by a selective wet etching will be presented.

3.2.1 Waveguide design

The design of a lateral single mode ridge waveguide (Figure 3.2) includes optimization of the ridge width (W) and etching depth (D). In order to obtain lateral single mode, a small refractive index difference Δn between the ridge and etched area is crucial to confine only the fundamental mode along the lateral direction. The typical value of Δn is about 10^{-3} [74-76]. However, the difference should be large enough to enforce index guiding rather than gain guiding [75]. It should be taken into account that increase of bias current will decrease Δn, thus making the index guiding weaker as the bias current increases. Calculation results of Δn and the maximum ridge width for single mode operation are shown in Figure 3.3. The calculation is

performed based on the effective refractive index method [74]. The refractive indexes of AlGaAsSb layers lattice matched to GaSb were estimated using the interpolation method [77]. As the lower p-cladding thickness increases, the index step decreases and the maximum width increases.

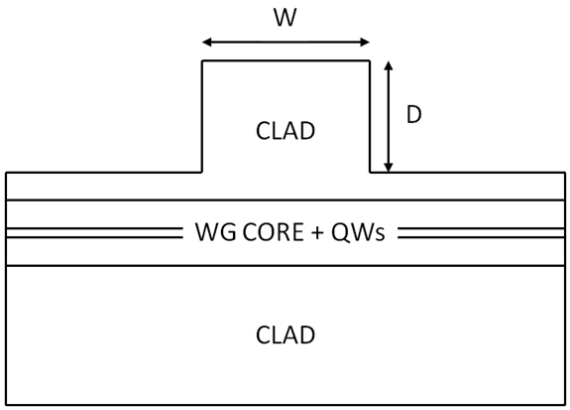

Figure 3.2 The cross-section of a generic ridge waveguide laser.

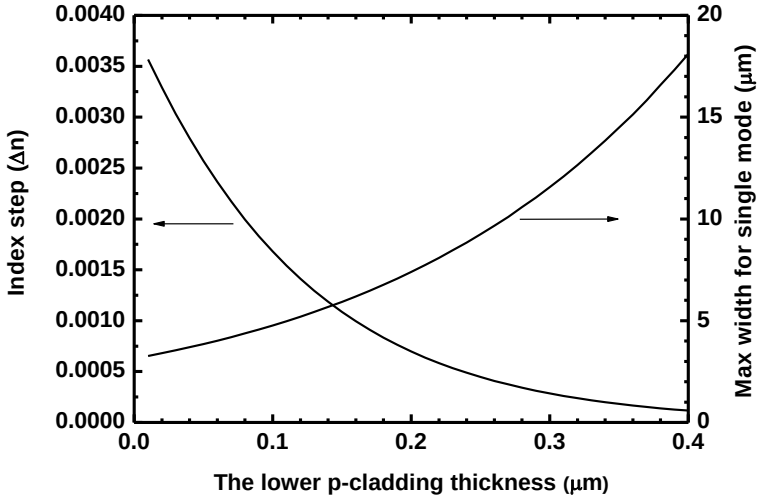

Figure 3.3 The refractive index difference and the maximum ridge width for single mode operation as a function of the lower p-cladding thickness.

3.2.2 Selective wet etching

The selective wet etching technique utilizes two etchants, tartrate based solution and hydrochloric acid (HCl) based solution. To prepare the tartrate etchant, sodium hydrogen-tartrate of 5 g was dissolved in de-ionized (DI) water with the ratio of 5 g : 90 ml. Hydrogen peroxide

(H_2O_2) of 30 ml and phosphoric acid (H_3PO_4) of 30 ml were added into the mixture and the solution was kept under stirring for 2 days. For the HCl etchant, the ratio of HCl : DI : H_2O_2 = 50 ml : 50 ml : 1 ml was used. To avoid outgasing, H_2O_2 was added just before etching.

The etching rate and selectivity for each etchant were estimated using test samples consisting of only the p-cladding side of the laser structure, corresponding to GaSb/ $Al_{0.85}GaAs_{0.07}Sb$/ $Al_{0.2}In_{0.25}GaAs_{0.235}Sb$. After formation of stripes with a photo-resist, the tartrate solution etched the GaSb layer. Subsequently, the HCl solution was used to etch the $Al_{0.85}GaAs_{0.07}Sb$ layer. Table 3-1 shows the etching rate of each etchant for the target materials. The tartrate etchant shows fast etching rate for low aluminum (Al<30%) containing layers, while the HCl etchant shows fast etching rate for Al-rich (Al>50%) layers. High degree of selectivity (1:30) between the $Al_{0.85}GaAs_{0.07}Sb$ and $Al_{0.2}In_{0.25}GaAs_{0.235}Sb$ layer confirmed that the $Al_{0.2}In_{0.25}GaAs_{0.235}Sb$ alloy could be suitable for the etch stop layer. Figure 3.4 shows the cross section of the etching result.

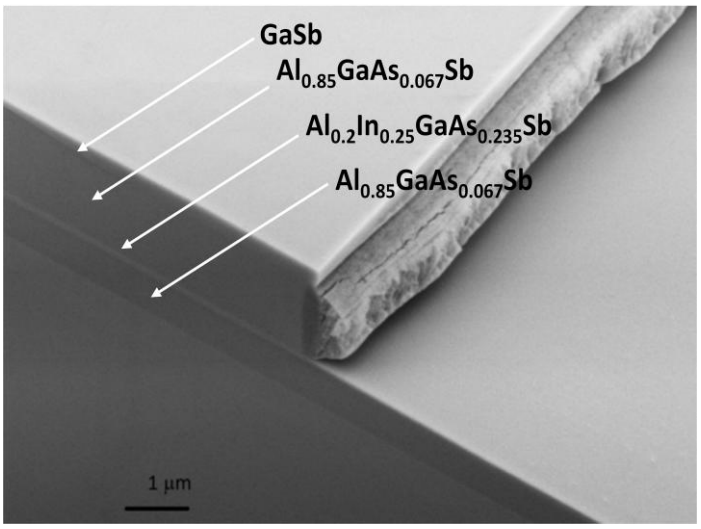

Figure 3.4 The cross-section of the test sample representing the p-side of the laser structure. The etched surface is the $Al_{0.2}In_{0.25}GaAs_{0.235}Sb$ etch stop layer. The uniformly etched surface is comparable with the non-etched GaSb surface. The projection near the sidewall is aluminum oxide.

Vertical sidewall of the ridge and uniformly etched surface on the etch stop layer were obtained. The layer next to the ridge wall is aluminum oxide characterized by x-ray photoelectron spectroscopy. Since the ridge (top p-cladding layer) contained the high aluminum content (Al=85%), most of the oxidation process occurred near the sidewall in the direction

parallel to the epi-layers with a random profile. Other etched regions did not exhibit the noticeable oxidation through the examination.

Table 3-1 Etching rate of the tartrate etchant and HCl etchant.

Etchant	GaSb (nm/s)	$Al_{0.85}GaAs_{0.067}Sb$ (nm/s)	$Al_{0.2}In_{0.25}GaAs_{0.235}Sb$ (nm/s)
Tartrate based	16.6	5	-
HCl based	3.2	30	1.1

3.2.3 Laser heterostructure growth and fabrication

Laser heterostructures with or without the AlGaInAsSb etch stop layer have been prepared to compare the laser performance with respect to the ridge width and depth as well as the presence of the etch stop layer (Figure 3.5). Etching will be stopped at the interface between the p-cladding and top $Al_{0.3}GaAs_{0.027}Sb$ waveguide for the wafers without the etch stopper since the waveguide composed of low Al content can be also used as an alternative etch stop layer using the HCl etchant.

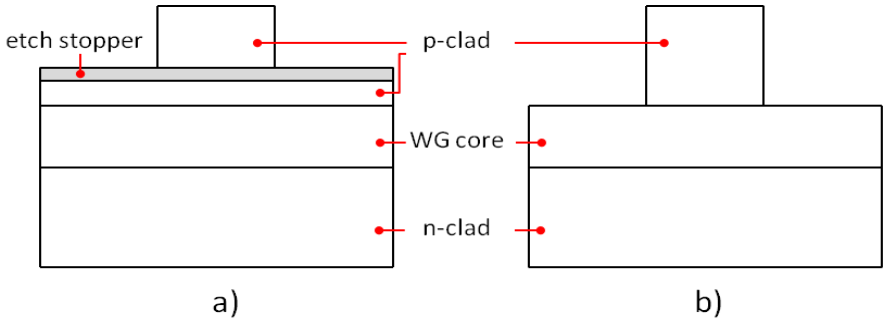

Figure 3.5 The cross-section of the lasers with (a) or without (b) an etch stop layer.

Laser heterostructures that are designed to emit the wavelength at 2.0 – 2.2 μm are illustrated in Figure 3.6. The symmetric broad waveguide design is applied into all structures with the compressive strain of QWs of ~1.2 – 1.5% to ensure strong carrier confinement and minimize threshold current density [78]. The laser structures were grown on Te doped GaSb substrates using a Veeco Gen-930 solid source MBE. The $Al_{0.85}GaAs_{0.07}Sb$ n-cladding layer doped with Te (1×10^{18} cm^{-3}) was grown on the compositional grading layer. The high refractive index $Al_{0.3}GaAs_{0.027}Sb$ waveguide layers enclosed the QW active region. The active regions consisted of InGa(As)Sb QWs and $Al_{0.3}GaAs_{0.027}Sb$ barriers. For the wafer 1, the 200 nm Be

(1×10^{17} cm^{-3}) doped $Al_{0.85}GaAs_{0.067}Sb$ lower p-cladding layer was followed by the 50-nm-thick $Al_{0.2}In_{0.25}GaAs_{0.235}Sb$ etch stop layer. On top of that, the $Al_{0.85}GaAs_{0.067}Sb$ top p-cladding layer was grown with the thickness of 800 nm. The low doping level in the p-cladding close to the waveguide side was intended to reduce optical loss enhanced by free holes. The-200-nm-thick compositional grading layer from $Al_{0.85}GaAs_{0.067}Sb$ to GaSb and the GaSb cap layer finalized the growth. Except for the QW layers, all layers were lattice matched to GaSb. The performance parameters of 100-μm-wide deep etched ridge waveguide multimode lasers emitting at 2.2 μm [72] are used as a reference for the narrow ridge lasers. It is assumed that edge effects are negligible in the 100-μm-wide stripe devices and thus they can be used as a reference to identify the effect of the narrow ridge waveguide structure on laser performance.

1 (λ=2.0 μm)	2 (λ=2.0 μm)	3 (λ=2.2 μm)
GaSb: 100 nm (Be:2e19)	GaSb: 50 nm (Be:2e19)	GaSb: 100 nm (Be:2e19)
Grading: 200 nm (Be:1e18)	Grading: 200 nm (Be:1e18)	Grading: 200 nm (Be:1e18)
$Al_{0.85}GaAsSb$: 600 nm (Be:1e18)	$Al_{0.85}GaAsSb$: 1000 nm (Be:1e18)	$Al_{0.85}GaAsSb$: 1000 nm (Be:1e18)
$Al_{0.85}GaAsSb$: 200 nm (Be:1e17)		
$Al_{0.2}In_{0.25}GaAs_{0.24}Sb$: 50 nm (Be:1e17)	$Al_{0.85}GaAsSb$: 500 nm (Be:1e17)	$Al_{0.85}GaAsSb$: 500 nm (Be:1e17)
$Al_{0.85}GaAsSb$: 200 nm (Be:1e17)		
$Al_{0.3}GaAsSb$: 400 nm	$Al_{0.3}GaAsSb$: 440 nm	$Al_{0.3}GaAsSb$: 400 nm
$In_{0.23}GaSb$: 10 nm ×3 $Al_{0.3}GaAsSb$: 30 nm ×2	$In_{0.23}GaSb$: 12 nm ×2 $Al_{0.3}GaAsSb$: 44 nm	$In_{0.28}GaAs_{0.03}Sb$: 11 nm ×2 $Al_{0.3}GaAsSb$: 20 nm
$Al_{0.3}GaAsSb$: 400 nm	$Al_{0.3}GaAsSb$: 440 nm	$Al_{0.3}GaAsSb$: 400 nm
$Al_{0.85}GaAsSb$: 1000 nm (Te:1e18)	$Al_{0.85}GaAsSb$: 1500 nm (Te:1e18)	$Al_{0.85}GaAsSb$: 1500 nm (Te:1e18)
Grading: 200 nm (Te:1e18)	Grading: 200 nm (Te:1e18)	Grading: 200 nm (Te:1e18)
Buffer: 500 nm (Te:1e18)	Buffer: 500 nm (Te:1e18)	Buffer: 500 nm (Te:1e18)
n-GaSb	n-GaSb	n-GaSb

Figure 3.6 Laser heterostructure with the AlInGaAsSb etch stopper (wafer 1: λ=2.0 μm) and without the etch stopper (wafer 2: λ=2.0 μm, wafer 3: λ=2.2 μm).

All three samples were processed in the following manner with different etching times dependent on the required etching depth and width. Fabrication was started from deposition of 3 – 4 μm wide Ti/Pt/Au p-contact stripes (Figure 3.7). First, the GaSb cap and compositional grading layer were etched by the tartrate etchant. The p-contact itself was used as an etching mask since the tartrate etchant does not damage metal contacts. The purpose of the first etching step is to remove low-Al-containing materials on the top of the device since they act as an etch stopper for the solution used next. Without this step the selective undercut of the p-cladding

material would result in an undesired mushroom-like etch profile. After the first etching, the wafer was immediately covered with a photo-resist to prevent unnecessary oxidation. To optimize the ridge width and etching procedure, we used different stripe widths varying from 8 µm to 14 µm. Second, to etch the p-cladding layer, the HCl etchant was used. Fast oxidation due to chemical reaction between the $Al_{0.85}GaAs_{0.067}Sb$ layer and H_2O_2 introduced dark color and rough surface, which provided good indication of etching progress. Etching was stopped when the oxidized Al layer was completely removed. The wafer was washed with DI water and inspected under a microscope to measure the lateral ridge width. If narrower ridges are required, the wafer can be returned to the solution and etched until a desired ridge width is formed. After defining the ridge, a 200-nm-thick silicon nitride covered the wafer. A 2-µm-wide dielectric window was opened for the Ti/Au overlay of the p-contact. The wafers were thinned to 120 µm for cleaving and ohmic contacts (Ni/Au/Ge/Ni/Au) on the n-side were formed by e-beam deposition. Laser devices with a 1-mm- or 2-mm-long cavity were mounted on gold-coated copper blocks for characterization. For CW output power measurements high reflectivity (>95%) and anti-reflective (<5%) mirror coatings were deposited on the laser facets and the devices were mounted epi-side down.

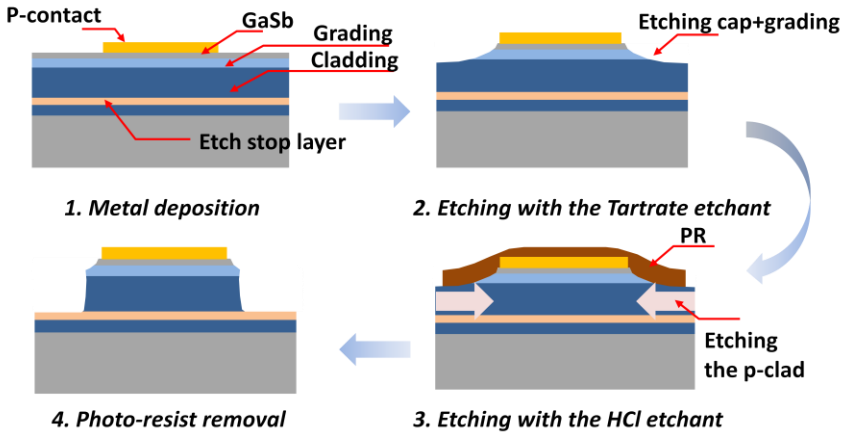

Figure 3.7 Fabrication procedure using the selective wet etching technique in clockwise order.

Figure 3.8 shows scanning electron microscope (SEM) images of the fully processed laser mirrors. The SEM images show that the demonstrated wet etching methodology is capable of yielding ridge widths below 4 µm and relatively vertical sidewalls. The ridge width of each laser is estimated at the bottom of the ridge and corresponding to 3.0 µm, 3.5 µm, and 6.0 µm for

Figure 3.8(a), (b), and (c), respectively. For the laser from the wafer 1 (Figure 3.8(a)), the second etching using the HCl solution was well stopped at the AlInGaAsSb etch stop layer, resulting in total etching depth of 1.1 μm. For the deep etched lasers, the etching depths are the same as the p-cladding thicknesses of them. The cap and grading projection with the length of ~1 μm in Figure 3.8(a) was created on each side owing to over etching by the HCl etchant. Similar situation is observed in the deeply etched lasers at the interface between the p-AlGaAsSb graded layer and the p-cladding layer (the dashed arrows in Figure (b, c)). It can be avoided by balancing time of the first and second etching. In order to check the dependence of the mesa profile on crystal orientation, the laser stripes were formed in the direction of the primary [011] and secondary [0-11] flat of the GaSb wafer and the similar profiles from both directions were obtained. The silicon nitride layer smoothly covered the sidewall, which ensured continuity of the p-contacts.

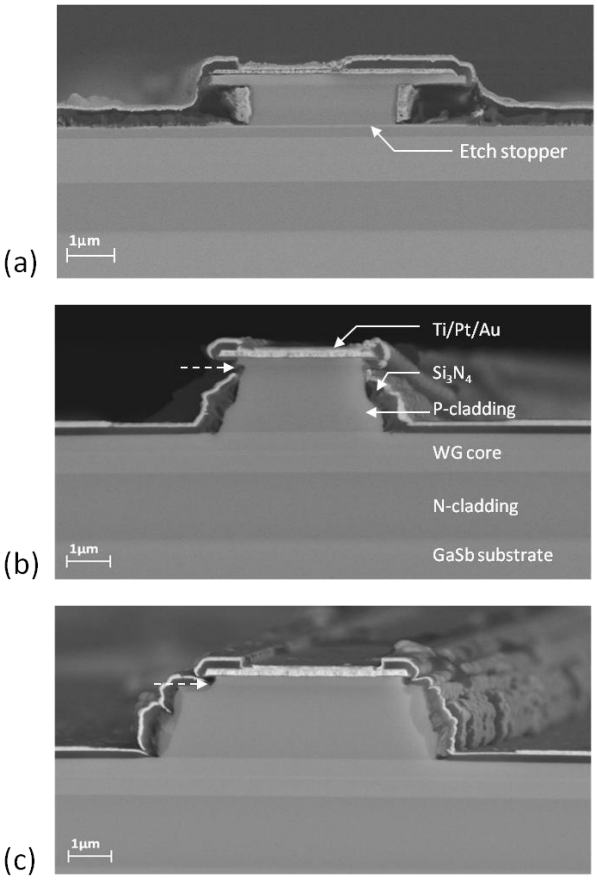

Figure 3.8 SEM images of the completed narrow ridge lasers: (a) from the wafer 1, (b) from the wafer 2, (c) from the wafer 3.

3.2.4 Laser characteristics

3.2.4.1 Lasers with the AlInGaAsSb etch stop layer

For characterization of the laser with the etch stop layer, the 90-μm-wide broad area (BA) laser processed from the same wafer was compared to the 6-μm-wide narrow (NR) laser. Figure 3.9 shows Light-Current-Voltage characteristic of 1-mm-long uncoated lasers under pulsed (100 kHz, 200 ns) current at 20 ˚C. The threshold currents of 25 mA and 160 mA are obtained from the NR and BA laser, respectively. The emission wavelength of the laser is 2.03 μm. The enhanced voltage on both lasers is predominantly due to carrier transport issues at the interface between the p-cladding and etch stop layer since the top of the valence band edge of $Al_{0.2}In_{0.25}GaAs_{0.235}Sb$ is about 140 meV higher than that of $Al_{0.85}GaAs_{0.07}Sb$ [79]. More precise matching between valence band tops of the p-cladding and etch stop layer will reduce the voltage loss. A laser without the etch stop layer showed 2 V less voltage at the same current density compared to the laser with the etch stop layer.

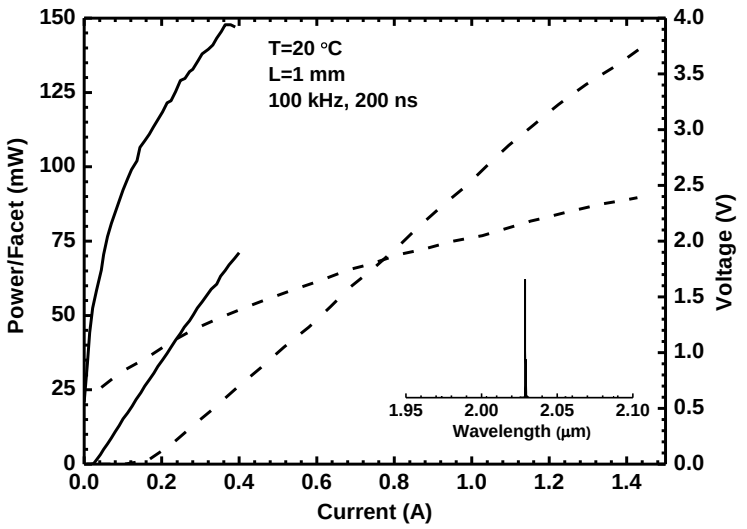

Figure 3.9 L-I-V of the 6-μm-wide NR (solid) and 90-μm-wide BA (dash) laser under pulsed current at 20˚C. Inset shows the emission wavelength of the laser. The cavity length for both lasers is 1 mm.

CW measurements were performed for the NR lasers, shown in Figure 3.10. Optical power of 70 mW was obtained at 20 ˚C from the 6-μm-wide 2-mm-long laser coated as AR/HR=5%/95%. The threshold current is 50 mA and the slope efficiency is as high as 211

mW/A, resulting in the differential quantum efficiency of 34%. This result is comparable with the recent result demonstrating the quantum efficiency of 40% from a 100-μm-wide 3-mm-long laser emitting at 2 μm [80]. The 4.5-μm-wide NR laser generated 45 mW of power with the threshold current of 70 mA and slope efficiency of 165 mW/A. The increased threshold current for the 4.5-μm-wide NR laser is presumably due to the increased overlap of the lateral optical field with the metal contact, thus increasing the optical loss.

Lateral far field divergences of the coated NR and BA laser are shown in Figure 3.11. The NR laser showed single lateral mode operation compared to the multiple peak far field of the BA laser. The single peak fundamental mode was maintained up to the current of 400 mA ($=8\times I_{th}$) above which the first mode became pronounced (Arrows in Fig. 7). Full width at half maximum (FWHM) of the far field increased from 7 to 9 degrees as the bias current increased. The FWHM along the fast axis is 66 degrees for the both lasers as expected.

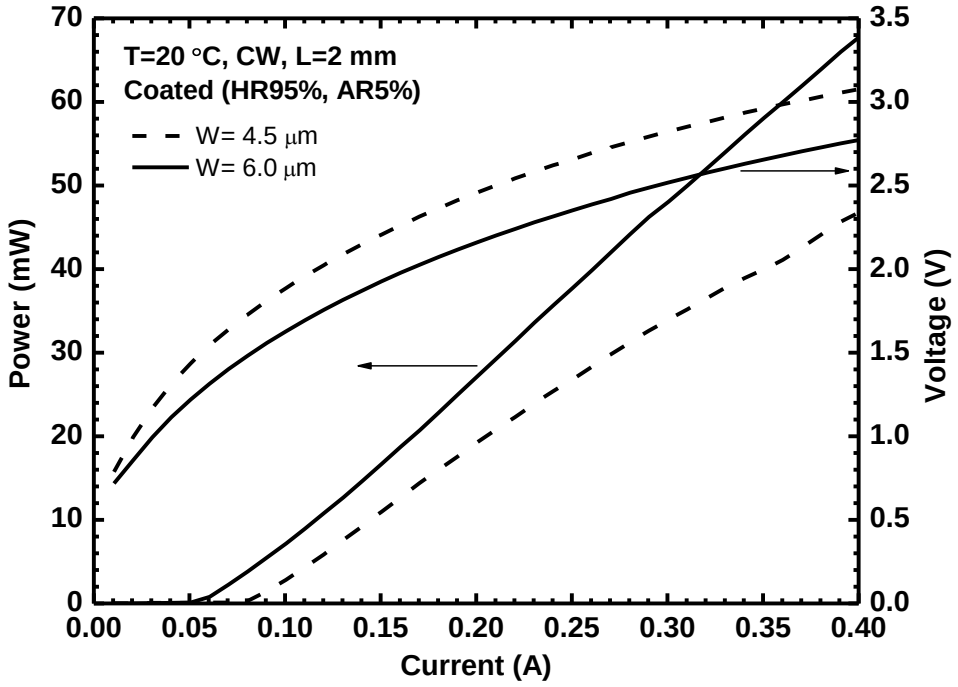

Figure 3.10 CW room temperature power and voltage of the 4.5-μm-wide (dash) and 6-μm-wide (solid) 2-mm-long AR/HR (5%/95%) coated NR lasers.

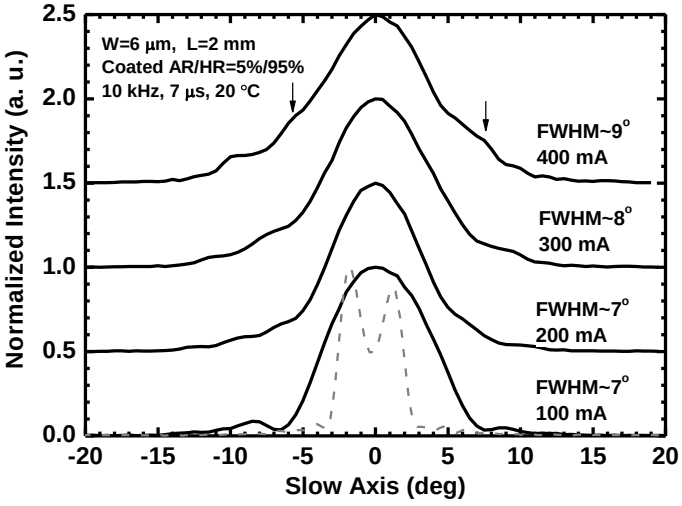

Figure 3.11 Far field divergence of the 6-μm-wide NR (solid) and 90-μm-wide BA (dash) laser along the slow axis. Both lasers are measured under pulsed (10 kHz, 7 μs) current at 20 ˚C. The arrows indicate the presence of the first mode at 400 mA.

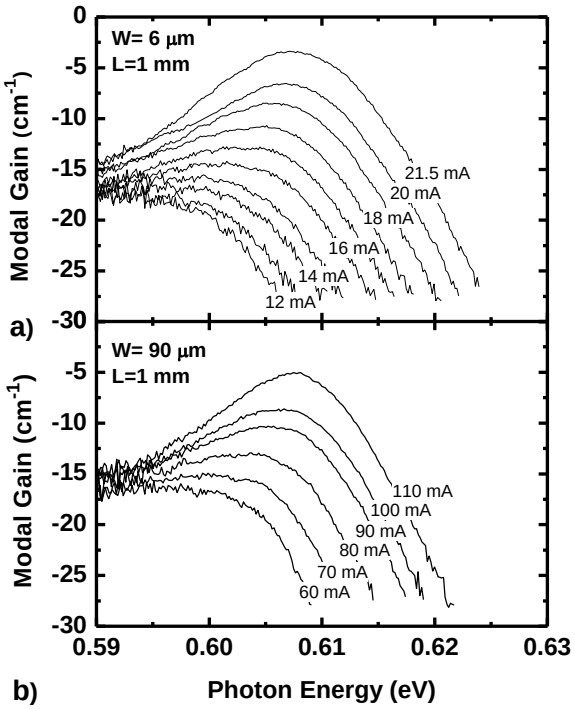

Figure 3.12 Modal gain spectra of the 1-mm-long 6-μm-wide NR (a) and 90-μm-wide BA (b) laser measured with 1 MHz, 200 ns at 20 ˚C. The current applied below threshold is indicated for each curve.

Modal gains of the BA and NR laser were measured using the Hakki-Paoli method [81] (Figure 3.12). Total losses of 18 cm^{-1} and 17 cm^{-1} were obtained from the 6-μm-wide NR and BA laser, respectively. Considering the mirror loss of 12 cm^{-1}, the internal losses are 6 cm^{-1} and 5 cm^{-1}. The similar internal losses of the NR and BA laser show that reducing the ridge width up to 6 μm does not change the optical loss significantly. The transparency currents (current density/well) for the NR and BA laser are 13 mA (72 A/cm^2/well) and 60 mA (25 A/cm^2/well), as shown in Figure 3.13. The differential gains, dg/dI, of the NR and BA laser are respectively 1.98 cm^{-1}/mA and 0.26 cm^{-1}/mA. Appropriate comparison can be made in the peak modal gains as a function of current density which are corresponding to 0.118 cm/A and 0.235 cm/A for the NR and BA laser, respectively. The threshold current density is twice higher and the differential gain is twice lower than that we expected in the 6-μm-wide NR laser. This indicates that the effective pumping area is twice larger than the etched stripe due to current spreading [82, 83]. The measurements of the far field and modal gain of the 6-μm-wide NR laser indicate that the current spreading contributes essentially to the enhanced threshold current density and to the onset of multimode operation at high current.

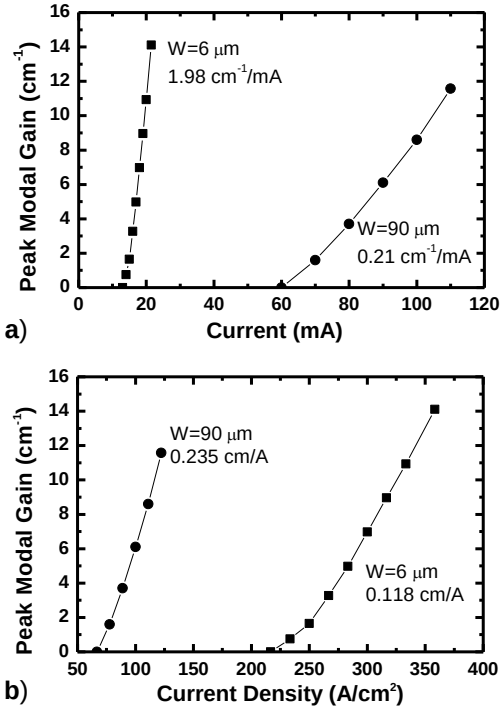

Figure 3.13 The peak modal gain vs. current (a) and current density (b) of the 6-μm-wide NR (square) and 90-μm-wide BA (circle) laser.

3.2.4.2 Lasers without the AlInGaAsSb etch stop layer

Figure 3.14 shows pulsed (100 kHz, 200 ns) power-current characteristics measured at 20 ˚C for uncoated 1-mm-long lasers emitting near 2.2 μm. Figure 3.14 plots power per unit width of the ridge versus nominal current density. The power-current characteristics of the 100-μm-wide multimode laser from the reference [72] are plotted together with those of the 6-μm-wide ridge devices (Figure 3.8(c)). Both the 100-μm-wide and 6-μm-wide lasers were fabricated from the same laser heterostructure wafer 3. The nominal threshold current density (current divided by the ridge area at the interface between the p-cladding and the waveguide core as measured by SEM) of the 6-μm-wide devices is about 200 A/cm^2, which is a twofold increase from that of the wide ridge lasers. The slope efficiency of the 6-μm-wide lasers is estimated to be ~0.15 W/A/facet, which is about a 25% reduction as compared to the wide ridge devices. For $\lambda = 2$ μm emitters with ridge width of about 3.5 μm (Figure 3.8(b)), the nominal threshold current densities were about 450 A/cm^2.

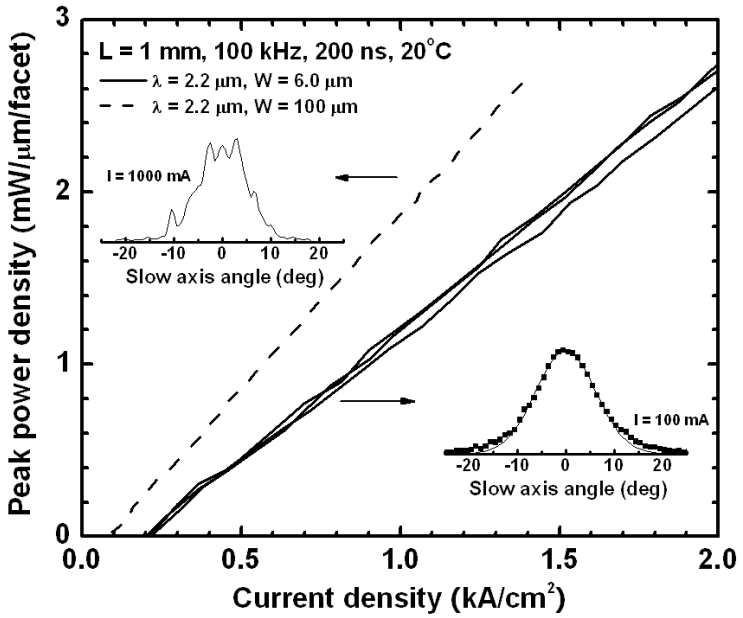

Figure 3.14 Peak power density (power per unit width per facet) vs. current density of the $\lambda = 2.2$ μm 6-μm-wide (solid) and 100-μm-wide (dashed) lasers with 1-mm-long uncoated cavities under pulse mode (100 kHz, 200 ns) at 20 ˚C. Three 6-μm-wide lasers from the same heterostructure wafer are plotted to show their uniformity. The inset is the measured far field divergence of each laser along the slow axis at the given current. The solid line in the far field of the 6-μm-wide laser is the Gaussian fitting.

The insets of Figure 3.14 show the measured slow axis far field patterns of the 100-µm-wide and 6-µm-wide ridge lasers emitting near 2.2 µm. The laser beam was scanned by a single photo-detector placed 30 cm away from the lasers. The multimode nature of the slow axis beam of the wide ridge device is apparent. A single lobe beam profile was observed from the narrow ridge lasers.

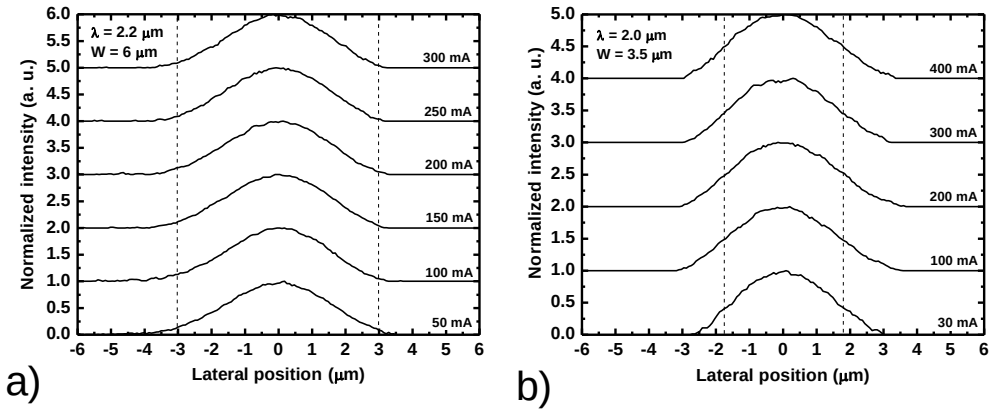

Figure 3.15 Current dependence of the lateral beam waist intensity patterns measured at 20 ˚C under pulsed (5 – 30 kHz, 200 ns) current for the 1-mm-long uncoated 6-µm-wide λ = 2.2 µm lasers (a) and 3.5-µm-wide λ = 2.0 µm lasers (b).

Magnified near field patterns of the laser beams were measured by an infrared camera (Figure 3.15). The ridge walls are denoted by two vertical lines to draw attention to the mismatch between ridge width and modal size. The near field patterns are current independent with about 4 µm FWHM for the 6-µm-wide λ = 2.2 µm lasers and 3.5 µm FWHM for the 3.5-µm-wide λ = 2 µm lasers. It should be noted that these are images of the beam waist but not of the laser mirror. The beam waist can be observed only above threshold and is located several microns in front of the laser mirror [84]. These images correspond to the far field patterns and are not affected by possible light scattering, current spreading or interference effects. The measurement of the lateral beam waist confirms stable single spatial mode operation of the deep etched ridge lasers.

The CW power-current-voltage characteristics of the 2-mm-long coated (AR/HR = 5%/95%) lasers measured at 20˚C are shown in Figure 3.16. The inset shows the spectra of the lasers measured at 100 mA. The λ = 2 µm and 2.2 µm lasers generate output power above 100

mW and 90 mW, respectively. Devices operate at voltage about 2 V at the highest bias current. The differential quantum efficiencies are about 45% for the 6-µm-wide lasers compared to 64% for the 100-µm-wide lasers. Somewhat unstable output power was observed within a certain range of applied CW current but this effect disappeared in pulse mode indicating it is a thermal effect [76].

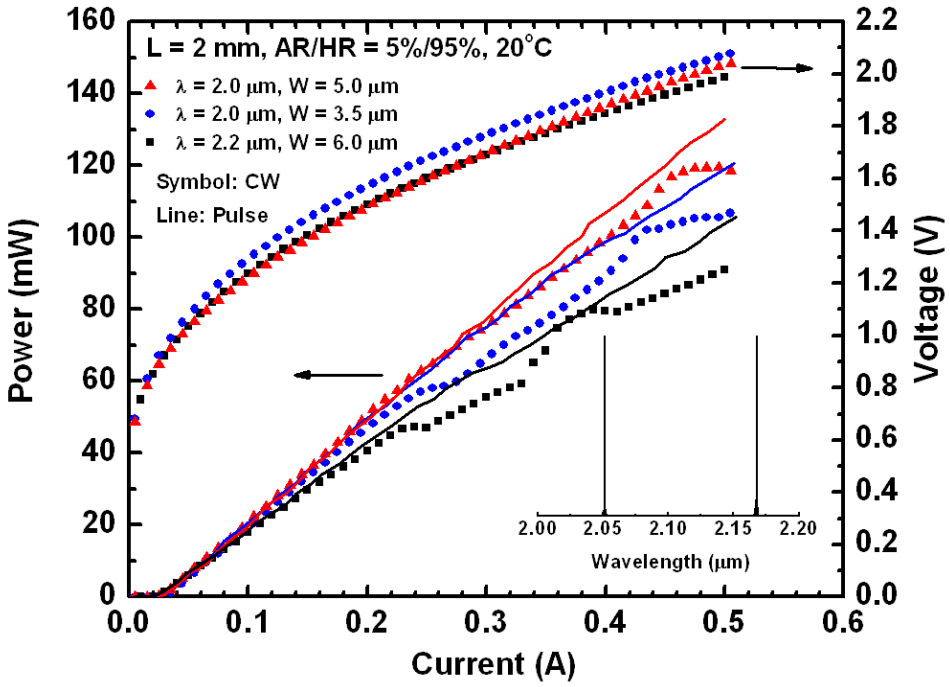

Figure 3.16 L-I-V of the 2-mm-long coated (AR/HR = 5%/95%) narrow ridge lasers under pulse mode (solid line, 100 kHz, 200 ns) and CW mode (symbol) at 20 ˚C. The inset is the wavelength of each laser measured at 100 mA.

Figure 3.17 plots the current dependence of far field patterns measured for the 3.5-µm-wide and 5-µm-wide λ = 2 µm lasers and for the 6-µm-wide λ = 2.2 µm lasers. Stable far field patterns with about 14˚ FWHM were observed for all devices. The measured far field patterns are in accordance with those calculated from the beam waist measurements described above.

Deep etched diode lasers with ridge widths in the range from 3.5 µm to 6 µm generate output power in a stable single spatial mode. A comparison of the narrow ridge device characteristics to those of 100-µm-wide multimode lasers shows a reduction of the slope

efficiency in ridge devices (about 25% for λ = 2.2 μm ridges with W = 6 μm) but their threshold current densities increase strongly. The near field measurements indicate that the lateral mode size is larger than the ridge width, especially for λ = 2 μm ridges with W = 3.5 μm.

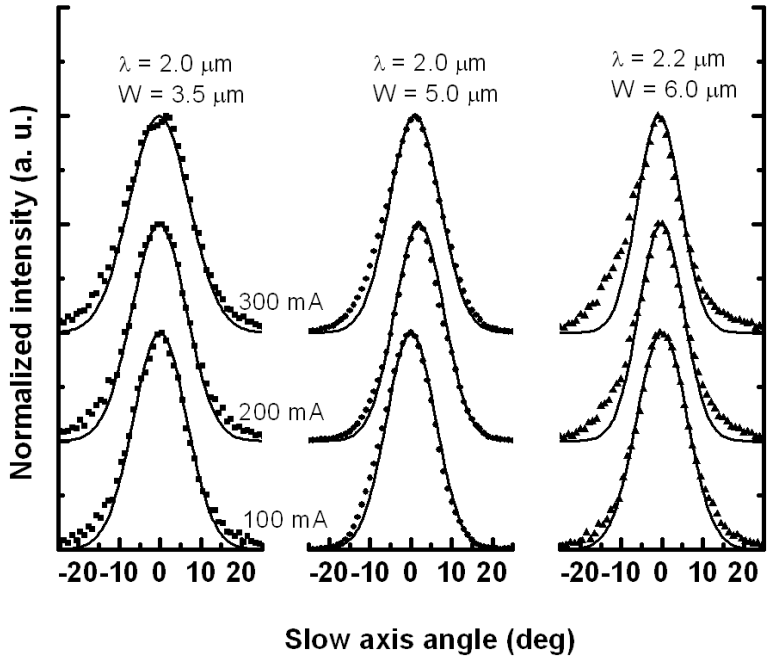

Figure 3.17 The far field divergence (symbols) along the slow axis for all narrow ridge lasers as a function of pulsed bias current (100 kHz, 200 ns) from 100 mA to 300 mA at 20 ˚C. The solid lines are the Gaussian fittings.

An effective refractive index method analysis [74] of the fabricated ridge waveguides demonstrates that they can support two lateral modes. The refractive indexes of the AlGaAsSb layers were estimated following an interpolation approach [77]. An idealized geometry of the ridge waveguide devices was assumed in the calculation (Figure 3.2). Figure 3.18 plots the calculated dependence of the effective lateral index step on the etching depth. It also plots the corresponding maximum width of the ridge waveguide to support only the fundamental mode. In our deep etched ridges the expected lateral effective index step is rather high, about 0.004 and 0.006 for λ = 2.0 μm and λ = 2.2 μm lasers, respectively. Thus both the 6-μm-wide and 3.5-μm-wide ridges can support two modes. However, lasing was observed only in the fundamental mode. Lasing of the second mode is suppressed presumably due to its lower modal gain. Indeed, transfer matrix calculation [85] shows that even for W = 6 μm ridges the optical confinement

factors of the fundamental and the second mode are about 85% and 25%, respectively (Figure 3.19). Thus the second mode is expected to experience higher optical loss due to enhanced interaction with the ridge sidewall and the metal contact, and has threefold lower gain. Figure 8 demonstrates that the calculated near field distribution of the fundamental mode is roughly in agreement with the measured near field pattern.

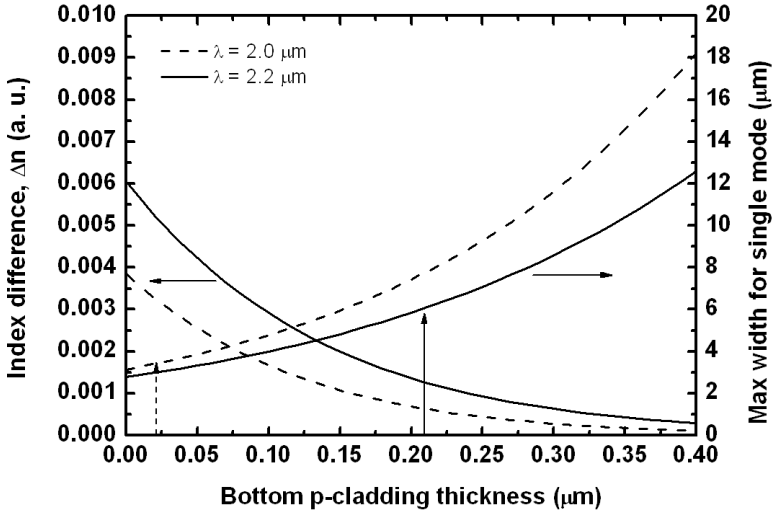

Figure 3.18 The refractive index difference and the corresponding maximum width of the ridge to support only the fundamental mode as a function of the bottom p-cladding thickness. The vertical arrows indicate the ridge widths discussed in this work (dashed - for $\lambda = 2.0$ μm and solid - for $\lambda = 2.2$ μm lasers).

In order to understand the nature of the large increase of the nominal threshold current density in the narrow ridge waveguide devices, modal gain spectra were measured using the Hakki-Paoli method [81]. Figure 3.20 plots the modal gain spectra of $\lambda = 2.2$ μm lasers with 100-μm-wide and ~6-μm-wide ridges, and for $\lambda = 2$ μm lasers with ~3.5 μm-wide ridges. In the long wavelength region the modal gain spectra saturates to the value of the total optical loss experienced by the lasing mode. For the 100-μm-wide ridge $\lambda = 2.2$ μm lasers the total modal loss amounts to about 16 cm^{-1}. For uncoated 1-mm-long devices, the mirror loss can be estimated to be about 12 cm^{-1}, hence the internal optical loss is about 4 cm^{-1}. These are the optical losses associated with light absorption and scattering in the waveguide formed by the epitaxial heterostructure layers. We assume that edge effects are negligible for the 100-μm-wide ridge lasers with guided modes that are well confined within the pumped wide ridge area. For the

narrow ridge lasers the internal losses can be estimated to be 7 – 9 cm^{-1} using the same approach. The internal loss increase in the narrow ridge waveguide lasers is presumably associated with interaction of the optical field at the ridge sidewalls. The measurement of the internal losses allowed estimation of the laser injection efficiencies and values of about 90% were obtained for all devices. The internal loss increase accounted for the decreased slope efficiency when the ridge width was narrowed. It can also be concluded that possible lateral leakage current contribution to the total current of the narrow ridge lasers is either negligible or saturated after threshold.

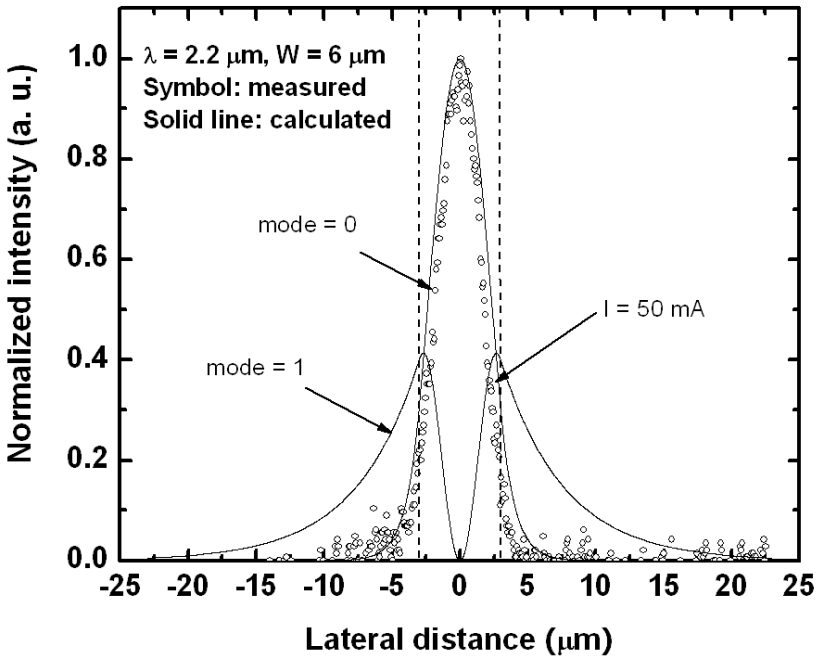

Figure 3.19 The lateral near field pattern at beam waist (circle) at I = 50 mA of the 1-mm-long uncoated 6-μm-wide λ = 2.2 μm lasers measured under pulse mode (100 kHz, 200 ns) at 20 ˚C. The solid lines are the calculated near fields for the guided modes. The vertical dashed lines indicate the ridge width.

Figure 3.20 reveals the differences in the shapes of the modal gain spectra of the wide and narrow ridge devices. For the 100-μm-wide ridge lasers the modal gain spectra were measured for one of the guided lateral modes (most likely the fundamental one) selected by spatial filtering optics. The lateral mode in the wide ridge lasers is well confined within the pumped section of the QWs. Thus the modal gain spectra correspond to the material gain spectra

multiplied by a vertical QW optical confinement factor. The QWs reach transparency condition when the quasi-Fermi levels are separated by the bandgap energy and further pumping is used to compensate for the optical loss. In the case of the narrow ridge lasers, the modal size can be larger than the pumped area (Figure 3.15). For ridges etched down to the p-cladding/waveguide core interface, the current spreading arguably occurs only due to ambipolar carrier diffusion in the waveguide core and active QWs. This is in contrast to shallow ridge waveguide designs where the p-cladding material remaining outside of ridge can lead to a wider current spreading profile as we have discussed in the previous section. The QW material outside the current path acts as an absorber optically pumped by the mode itself. Hence population inversion only under the ridge is insufficient. This scenario can explain distortion that can be noticed in the modal gain spectra of the 6-µm-ridge lasers, and that becomes apparent in the narrow 3.5-µm-ridge lasers. Figure 3.20(c) clearly shows that at low injection currents the modal gain exhibits a peak that is below the waveguide loss. This is not observed in the gain spectra of the wide ridge lasers due to a nearly 100% overlap between the mode and the pumped area. The effective transparency current density for the narrow ridge lasers is expected to increase with the reduction of the ridge width due to a progressively increasing mismatch between the pumped area and the lateral modal profile. Figure 3.21 supports this scenario from the fact that the nominal transparency current density increased without the proportional decrease of the differential gain as the ridge width was narrowed. Based on this analysis, it can be speculated that the mismatch between the modal size and the current path rather than lateral current leakage is responsible for the increased nominal threshold current density of the deep etched narrow ridge waveguide lasers.

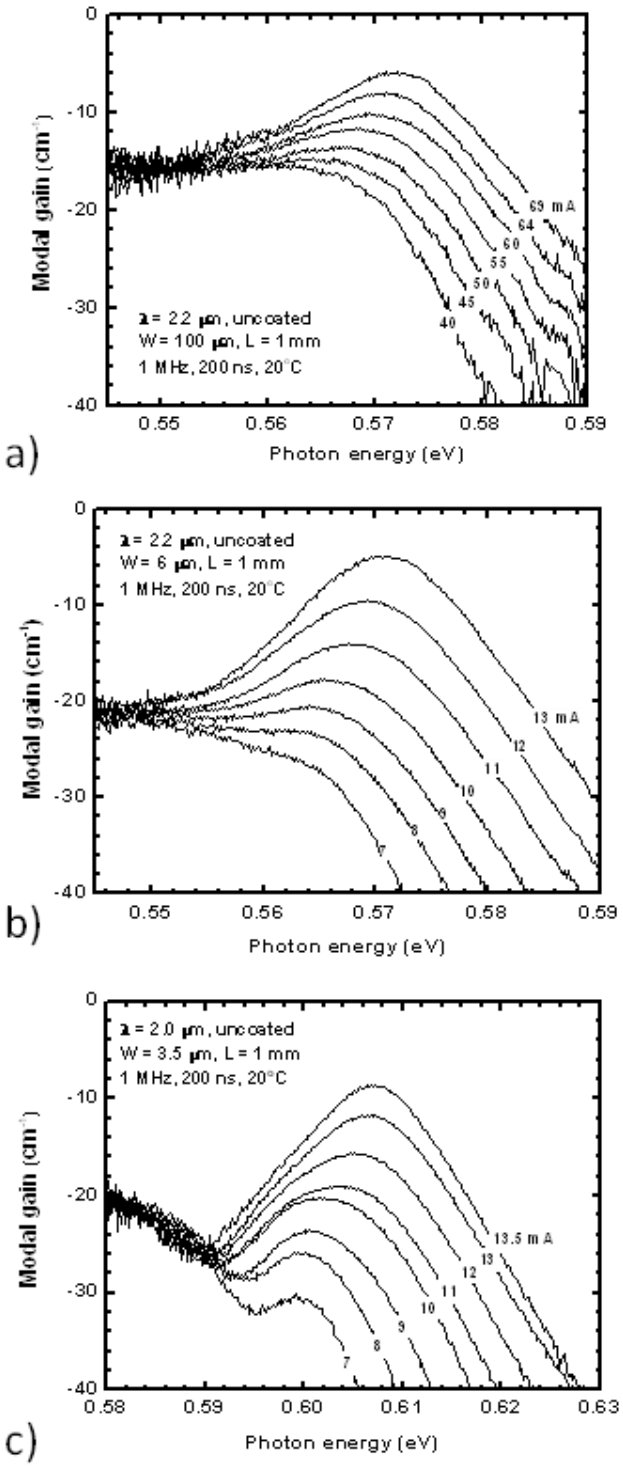

Figure 3.20 Modal gain spectra of 1-mm-long uncoated lasers measured in pulsed regime (1 MHz, 200 ns) at 20 ˚C: (a) the 100-μm-wide λ = 2.2 μm laser, (b) the 6-μm-wide λ = 2.2 μm laser, (c) the 3.5-μm-wide λ = 2.0 μm laser.

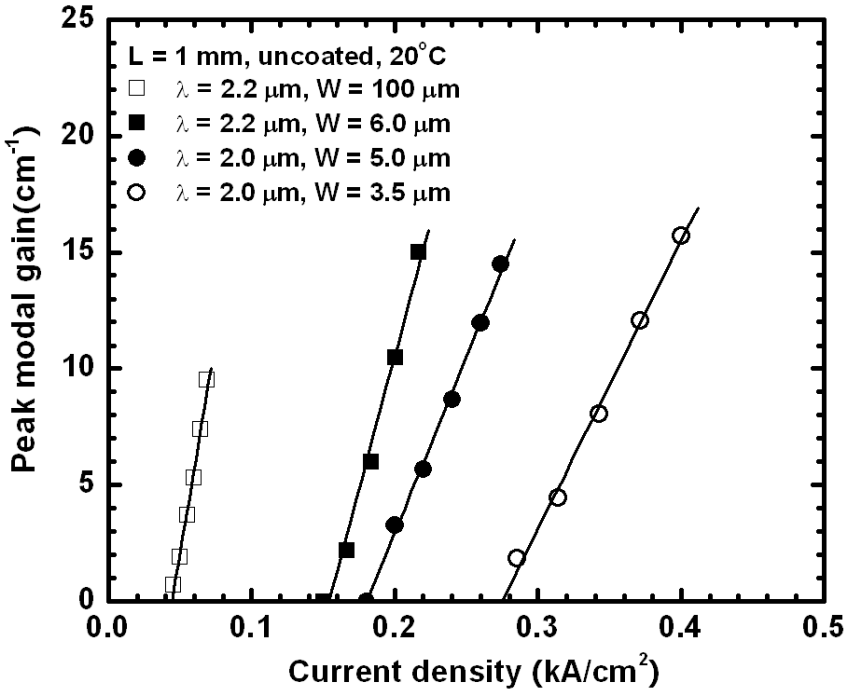

Figure 3.21 The peak modal gain as a function of current density for all lasers.

3.3 Optically tunable quantum cascade lasers

Rapidly-tunable quantum cascade lasers (QCLs) is a key element for the recently proposed long-wavelength infrared (LWIR) frequency modulation (FM) optical data links [86] which can have orders of magnitude higher signal-to-noise ratio compared to the amplitude-modulation (AM) systems. More specifically, the FM advantage is proportional to $(\Delta F/f)^2$, where ΔF is the range of the carrier frequency excursion in FM modulation and f is the signal data bandwidth [86, 87].

QCLs are the only semiconductor lasers that can operate CW mode at room temperature in LWIR. Currently, frequency tuning of the distributed feedback (DFB) QCLs is typically achieved by temperature control over the effective refractive index using pump current modulation [88, 89]. The bandwidth of the current tuning for a room temperature operated device is strictly limited since high-performance CW DFB QCLs must have efficient thermal packaging that prevents excessive heating. The bandwidth is estimated to be well below 25 MHz [89]. A way to tune a QCL emission frequency fast is Stark modulation of the optical transition energy either within the laser active region [90-92] or in a separate passive section optically coupled with the laser waveguide [93]. Used the latter approach it was possible to achieve over 10 GHz of continuous tuning of the laser emission line [93]. However, this approach results in a large increase in waveguide loss that prevents CW room-temperature operation of these lasers. Strong accompanying AM modulation of the laser emission is also an undesirable effect for FM data links.

Optical excitation of electron-hole pairs in a QCL is a direct way to tune the laser wavelength through control over the effective refractive index of a laser mode. It combines advantages of continuous single mode tuning and high wavelength modulation speed. Chen et al. [94] demonstrated 0.375 nm wavelength modulation (≈2 GHz frequency modulation) amplitude of a MIR QCL operated at 77 K by illuminating the QCL facet from 820 nm emission of a Ti:sapphire laser. The bandwidth of the wavelength modulation was estimated experimentally as 1.67 GHz.

In this section, we demonstrate the continuous tuning range of ~0.3 cm^{-1} (~10 GHz) with little change in the laser threshold current. We also provide direct measurements of QCL spectra and light output-current characteristics under optical excitation. To increase both tuning

efficiency and pumping uniformity, we use the pumping wavelength of 1064 nm. The bandgap energy of the pumping source belongs to the transparency region of InP substrate and cladding layers. But it is well matched to the absorption edge of the GaInAs inner waveguide core and the active region. The optical excitation of electron-hole pairs is achieved by illuminating the device along the whole laser waveguide through the substrate using the epilayer-side-down mounted QCLs.

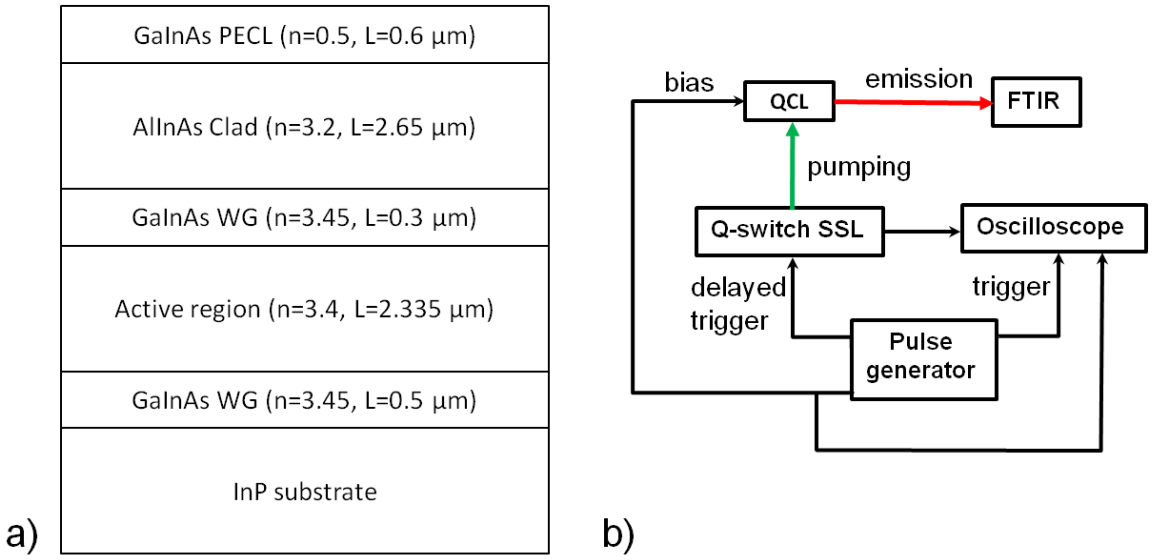

Figure 3.22 (a) The layout of QCL waveguide layer sequence. (b) The schematic of the experimental setup.

The InGaAs/AlGaAs QCLs used in the experiments are based on the double phonon depopulation scheme [95] and emitted near 9 μm at room temperature. The QCL heterostructure is shown in Figure 3.22(a). The lasers were processed as deep etched mesas with dimension of 2 mm length and 16 μm width. Thick (~6 μm) SU-8 2005 photoresist (MicroChem Corp.) was used as an insulation layer. The schematic of the experimental setup and the pumping geometry are presented in Figure 3.22(b) and Figure 3.23(a). The lasers were mounted using the epilayer-side down scheme onto copper blocks. Nd:YVO_3 Q-switch laser emitting at 1064 nm was used as a pumping source. Since both InP and AlInAs are transparent for this wavelength, the excitation emission was absorbed only in the active region and GaInAs inner waveguide core layers (Figure 3.23(b)). The excitation emission was coupled into the QCL through 250 μm wide stripe window in the back contact using cylindrical optics (Figure 3.23(d)). High resolution QCL emission spectra were obtained using a FTIR spectrometer with a photovoltaic MCT detector. A cylindrical lens was used to focus 1064 nm radiation into an approximately 400 μm by 2 mm

spot on the laser backside. Interband photoluminescence of the QCL structure at 0.75 eV collected from the QCL front facet was used to adjust the position of the pumping beam and obtain maximum overlap between the pumping beam footprint and the QCL ridge waveguide. The Nd:YVO_3 laser produced 80 ns light pulses at 50 kHz repetition frequency. The QCLs were operated with 50 ns current pulses synchronized with the Nd:YVO_3 pulses.

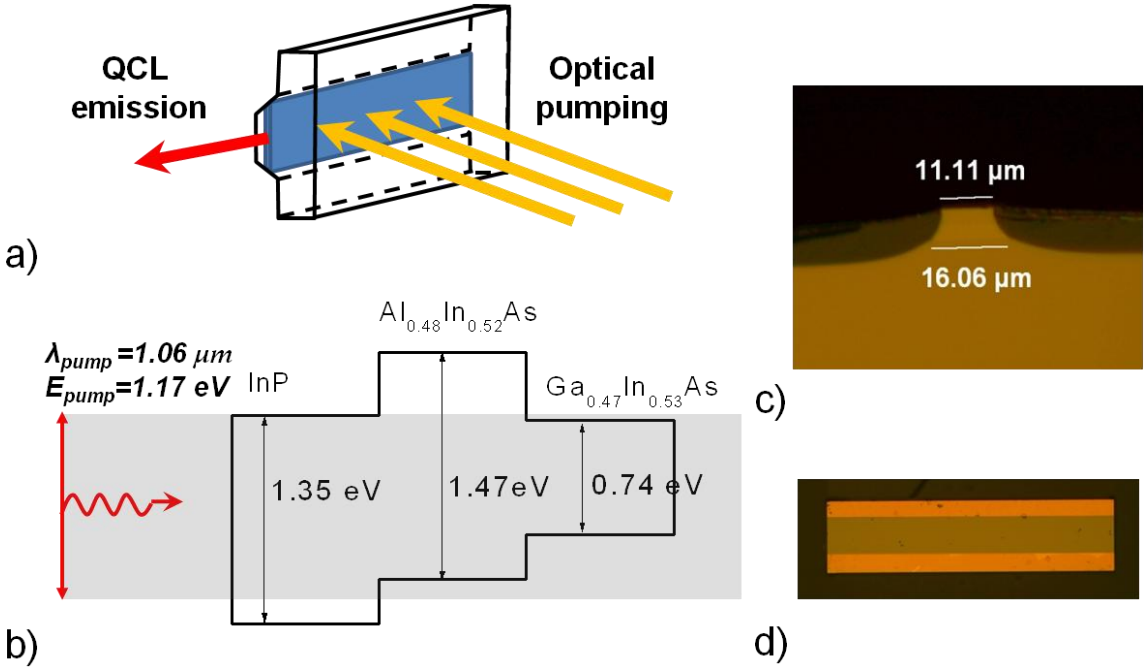

Figure 3.23 (a) Optical pumping geometry used in our experiments. (b) Bandgaps of the semiconductor materials used in our device compared to the optical pumping photon energy. (c) The image of the device facet. (d) The image of the 250 μm window at the backside of our devices for optical pumping.

The QCL spectrum consists of a comb of sharp peaks (laser fringes) corresponding to the different longitudinal Fabry-Perot modes. Spectral position of the peaks is determined by the effective refractive index and the cavity geometry. Due to unipolar nature of the QCL, generation of electron-hole pairs in the laser's active area does not contribute directly to the population inversion but has strong effect on the effective refractive index and, hence, on the spectral position of the laser modes.

A blue shift of the laser mode wavelength under the pumping emission was observed (Figure 3.24(a)). The magnitude of the shift continuously depended on the pumping power (Figure 3.24(b)) and reached over 0.3 cm^{-1} (~10 GHz) at the pumping power density of only 93

W/cm^2. The frequency of one of the fringes as a function of time delay between the QCL bias and optical excitation pulses is presented in Figure 3.25(a). As the optical pulse of the Nd:YVO_3 laser is synchronized with the QCL bias pulse, a spectral shift of the QCL modes is observed. The modal frequency shifts to the higher energy side that indicates reduction of the effective refractive index. The change in the effective refractive index can be calculated from the spectral shift data as $\Delta n_{eff} = n_{eff}\frac{\Delta\lambda}{\lambda}$. This expression gives $\Delta n_{eff} = 1.1 \cdot 10^{-3}$ at the pumping density of 93 W/cm^2, using n_{eff}≈3.3 calculated using the waveguide geometry of the presented QCL.

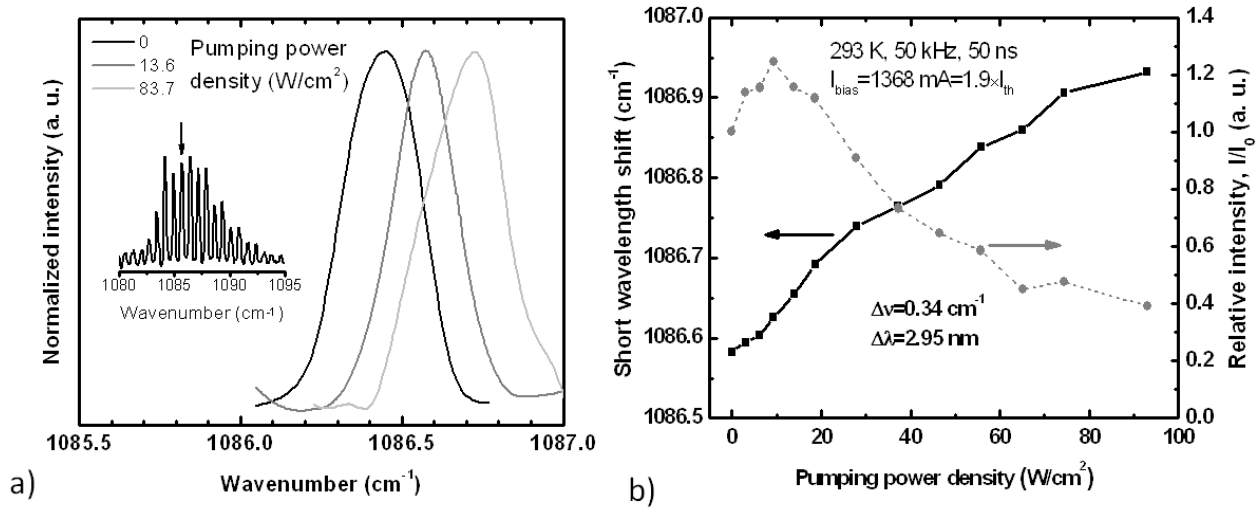

Figure 3.24 (a) Zoom-in of the quantum cascade laser emission spectrum under different optical pumping intensities. A frequency shift of a single longitudinal mode is clearly seen. Inset: emission spectrum of the device. (b) Spectral position of a longitudinal mode in the QCL emission spectrum (left axis) and QCL power output (right axis) as a function of optical pump intensity.

The spectral shift was accompanied by a decrease in QCL emission power (Figure 3.24(b)). Since we are working in a constant bias current mode, the drop of the laser intensity can be explained by the increase of the laser threshold due to additional optical loss caused by photo-generated carriers. The light output-current characteristics of the QCL taken at different Nd:YVO_3 pumping power densities are shown in Figure 3.26(a). Laser threshold increase of ~9% was observed at the pumping density of 93 W/cm^2.

The change of the refractive index and increase of optical losses in our devices are resultant from electron-hole plasma created by 1064 nm pumping on both the active region and

the GaInAs inner waveguide layers. Using the results of direct measurements of the QCL structure transmission and GaInAs absorption coefficient of 1.2x10^4 cm^{-1} at 1064 nm [96], we can estimate that ~40% of the pump power transmitted into the substrate is absorbed by the bottom InGaAs inner waveguide layer, ~30% is absorbed by the QCL active region and ~8% is absorbed by the top InGaAs inner waveguide layer. The contributions of the bottom InGaAs waveguide cladding layer and the QCL active region to the change of the effective refractive index of the laser mode are commensurable. Considering significantly smaller absorption in the top InGaAs cladding layer, we may neglect the contribution of this layer to the effective index change. Concentration of photo excited carriers in the active area can be roughly estimated from relative change of the current $\Delta I/I_0$ through the QCL structure under the illumination at a fixed voltage and the average doping level N_{av} of the structure: $\Delta N \approx N_{av} \frac{\Delta I}{I_0}\Big|_{U=const}$. To do that we used the current-voltage characteristics presented in Figure 3.25(b). We assumed that the major contribution to the change in the structure conductivity is given by the electrons since the transport of holes in the growth direction is almost completely blocked by the barriers. The estimation gives photo excited electron concentration of $\Delta N \approx 5 \cdot 10^{15}\ cm^{-3}$ for the pumping power of 93 W/cm^2. The contribution of photo-excited carriers to the effective refractive index can be estimated using Drude model as [97]:

$$\Delta n_{eff} \approx -n_0 \left(\Gamma_c \frac{\Delta \omega_{pc}^2}{2\omega^2} + \Gamma_a \frac{\Delta \omega_{pa}^2}{2\omega^2} \right) \qquad 3\text{-}8$$

, where $\Delta\omega_{pc,pa}^2 = \frac{\Delta N_{c,a} e^2}{\varepsilon_0 \varepsilon m_e^*}$ is the change in the plasma frequency due to additional carrier concentrations $\Delta N_{c,a}$ in the lower inner waveguide layer and active area, Γ_a ~0.53 and Γ_c ~0.09 are the confinement factors of the laser mode within the active region and within the lower InGaAs inner cladding layer, respectively, (Figure 3.26(a)), ω is the lasing frequency and $n_0 \approx 3.3$ is the effective refractive index of the laser mode at zero pumping intensity. For simplicity, we further neglect the contribution to the change in n_{eff} from the lower cladding layer and focus on the contribution to Δn_{eff} from the active region only. Equation 3-8 is valid if $\omega_p \ll \omega$, which is the case of our experiment where $\omega \approx 2.1 \times 10^{14}$ Hz and $\omega_p \approx 1.39 \times 10^{13}$ Hz for the average doping concentration per period of $N_0 \approx 4 \cdot 10^{16}\ cm^{-3}$. We then obtain an additional photo-excited electron concentration of $\Delta N \approx 5 \times 10^{15}\ cm^{-3}$ in the active region

produces the change of the effective refractive index of $\Delta n_{eff} \approx 0.65 \times 10^{-3}$. This value is close to the experimentally observed index variation of $\Delta n_{eff} \approx 1.1 \times 10^{-3}$ for the pumping power of 93 W/cm^2. Though the contribution of free holes to the effective refractive index change it is expected to be relatively small [98], it may be a source for the discrepancy between experimental and theoretical values of the refractive index modulation amplitude. It should also be noted that we have omitted contributions of the cladding layers to the effective refractive index change in equation 3-8. Since the QCL lasing mode is TM polarized, to calculate free carrier contribution to the effective refractive index we have to consider polarization in the growth direction. For the first approximation, it can be done by substituting the free electron effective mass in the plasma frequency expression for corresponding parameter of the transverse motion in the injector subband. In a simple model, we can consider injector under the threshold bias as a superlattice whose subband has a significant region of a quadratic spectrum near the bottom. This region is characterized by weighted average of the bulk effective masses [99] in GaInAs and AlInAs layers:

$$m_{inj}^{*} = \frac{\tilde{d}_{GaInAs} m_{GaInAs}^{*} + \tilde{d}_{AlInAs} m_{AlInAs}^{*}}{\tilde{d}_{GaInAs} + \tilde{d}_{AlInAs}} \approx 0.054 m_0 \qquad 3\text{-}9$$

, where $\tilde{d}_{GaInAs}$ and $\tilde{d}_{AlInAs}$ are average thicknesses GaInAs and AlInAs layers in the injector.

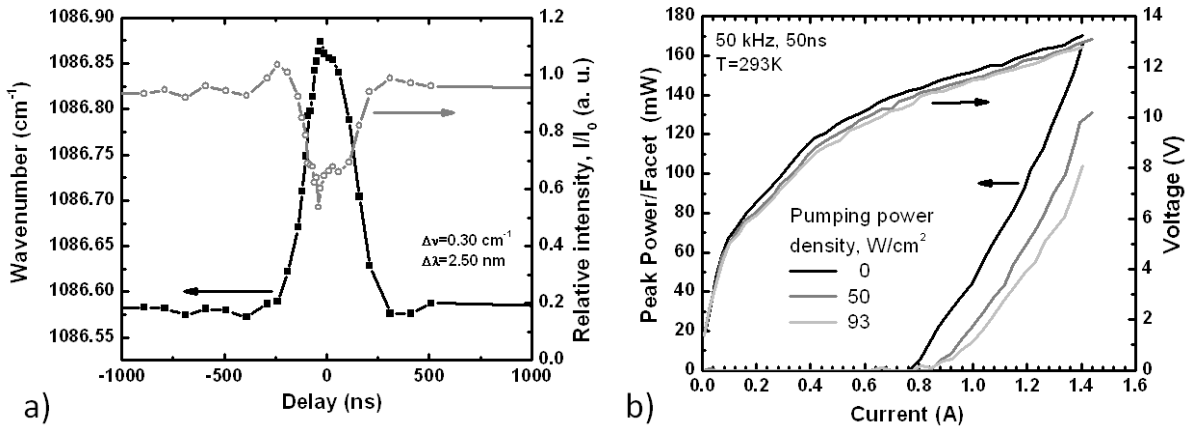

Figure 3.25 (a) Spectral position of the laser mode and the power output from our device as a function of the delay of the optical pumping pulse with respect to the QCL bias pulse. (b) Light output-current (L-I) and current-voltage (I-V) characteristics of the tested device for different optical pumping intensities.

The additional optical loss due to the photo-generated carriers can be estimated using the relative change of the laser threshold and value of the waveguide loss in our devices $\alpha_{0I}\approx$ 12.2 cm^{-1} obtained from the experimental dependence of the reciprocal efficiency on the laser cavity length (Figure 3.26(b)). The main component of the waveguide loss in long wave infrared QCLs is free carrier absorption [100] whose magnitude is proportional to the carrier concentration [97]. So additional loss $\Delta\alpha_I$ due to photo-generated carriers can be estimated as:

$$\Delta\alpha_I \approx \alpha_{0I}\frac{\Delta N}{N_0} = 1.5\ cm^{-1} \qquad 3\text{-}10$$

This value of $\Delta\alpha_I$ results in an approximately 8% increase of the total optical loss $\alpha_{tot} \approx 18.2\ cm^{-1}$ in our devices (which includes mirror loss α_m ~6 cm^{-1}). This number is in good agreement with the observed approximately 9% increase of the threshold current.

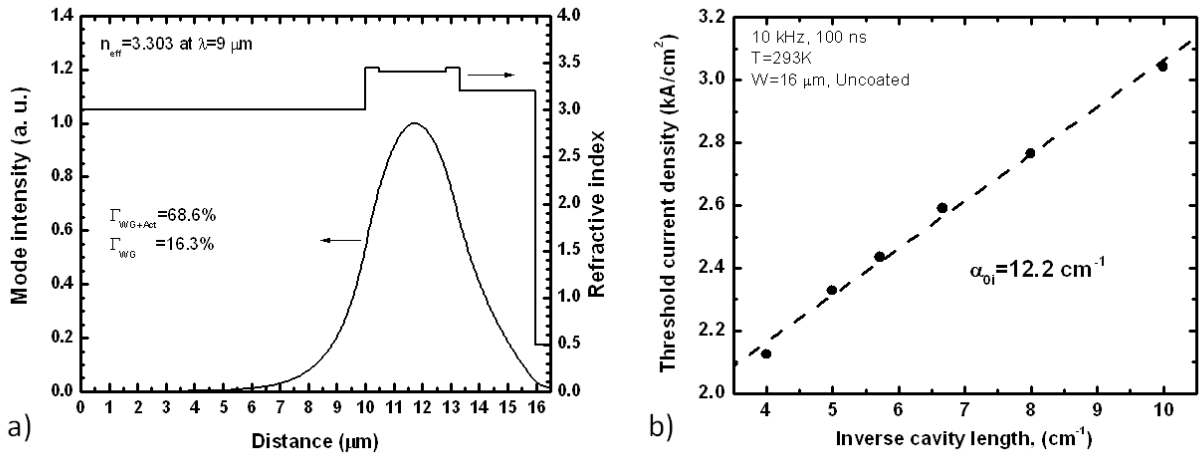

Figure 3.26 (a) TM_{00} waveguide mode and waveguide refractive index profiles in our devices. (b) Dependence of the threshold current density in our devices on the reciprocal cavity length. The value of waveguide loss of α_{0I}~12.2 cm^{-1} is obtained assuming $J_{th}(1/L)\propto\alpha_{tot}=ln(R_m)/L+\alpha_{0i}$, where R_m~0.28 is the uncoated facet reflectivity and L is the laser cavity length.

Estimation of the lifetime of photo excited carries at pumping power of 93 W/cm^2 from $\Delta N\approx 5\times10^{15}\ cm^{-3}$ and absorbed pumping power (~65 W/cm^2) gives $\tau\approx$2.9 ns. This relatively short lifetime can be explained by contribution of the surface recombination at the edge of a narrow stripe whose width is much less than the typical carrier diffusion length (~10 μm). Since the carrier lifetime provides fundamental limitation to the optical tuning speed, the optical modulation bandwidth of the QCL wavelength is expected to be in the above 0.3 GHz, which is

in agreement with the results presented in the reference [94]. Sub-10-ns carrier lifetime is also supported by the data presented in Figure 3.25(a), although temporal resolution of these measurements is not sufficient to determine τ more accurately.

3.4 Conclusion and future work

GaSb based interband type I QW lasers fabricated by the selective wet etching showed spatial single mode with optical power as high as 100 mW at room temperature. The transverse and lateral mode measured from the 3.5 μm deep etched laser is plotted in Figure 3.27. The laser with the AlInGaAsSb etch stop layer was able to provide controlled etching depth by inserting the stopper layer at desired location. Additional voltage across the layer can be further improved by facilitating carrier transport with less resistive alloy but selective to the HCl etchant such as AlGaAsSb with 30% of Al content. The deep etched laser showed better performance than the laser with the etch stopper in terms of stability of lateral mode and optical power. Although the wide shape of the fundamental mode introduced increase of transparency current, the effect was not significant to deteriorate the laser operation.

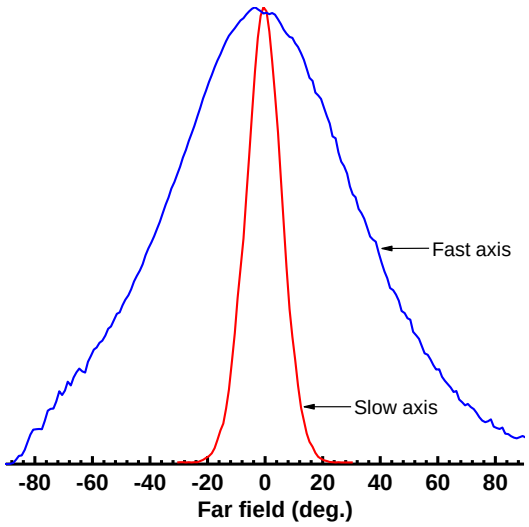

Figure 3.27 GaSb based type I QW laser fabricated by the selective wet etching with 3.5 μm of the ridge width. Far field was measured at room temperuature under pulse (10 kHz, 7 μs) current of 300 mA.

A novel optical tuning method has been developed for QCLs emitting near 9 μm. Using a Nd:YVO_3 Q-switch laser emitting at 1064 nm as a pumping source, we have exclusively excited

carriers in the active region and demonstrated continuous QCL frequency tuning over 0.3 cm^{-1} (10 GHz or 3 nm). Given the carrier lifetime of $\tau \approx 2.9$ ns, we estimate the wavelength modulation bandwidth at above 0.3 GHz. The index change and additional absorption induced by optically generated free carriers are described well within the Drude model.

Selection of the lasing mode by using the distributed feedback grating along the laser cavity can increase the range of wavelength tuning by placing the mode near the peak of laser gain. This will demonstrate fast and continuous tuning of single frequency QC lasers for FM free space communication.

Chapter 4

Photodetectors

4.1 Introduction

Photodetectors operating in the MIR region are indispensable components to realize the application systems mentioned in the previous sections. Especially, since energy in infrared region cannot be perceived by human sensors, detection of unperceivable substances that generate infrared energy makes the stance of infrared detectors more important. For instance, methane gas, which is highly explosive (low explosive level of 5% in the air), odorless, and colorless as well as a source of a greenhouse effect, can be detected with accuracy of part-per-billion (ppb) level using a laser diode and detector optopair [6, 67]. In this chapter, we will cover the fundamental operation of photodetectors and experimental results of the nBn type of detectors specifically for the methane gas sensing application.

4.2 Figures of merits

4.2.1 Quantum efficiency and responsivity

Semiconductor photodetectors generate electron hole pairs in the semiconductor material via light absorption process. In the device point of view, the photodetectors are a transducer that converts optical signal to electric signal. When light with energy higher than the bandgap energy of an active region is incident on a photodetector, photons absorbed in the active region will generate electron hole pairs. The ratio of the number of generated electron-hole pairs to the number of incident photons is defined as the internal quantum efficiency, written as,

$$\eta_{int} = \frac{\#\ of\ photo-carriers\ generated\ in\ the\ active\ region}{\#\ of\ incident\ photons\ in\ the\ active\ region} \qquad 4\text{-}1$$

. The internal efficiency of 100% means one photon can generate one pair of electron and hole. To estimate the internal quantum efficiency the light absorption occurred through layers adjacent to the active region has to be found. Photocurrent is contributed by the photo-generated electron

hole pairs that reach to the contact without recombination. Thus, the external quantum efficiency is usually used to characterize the conversion efficiency from photon energy to generated photocurrent, defined as,

$$\eta_{ext} = \frac{\#\ of\ photo-carriers\ measured}{\#\ of\ incident\ photons\ per\ unit\ time} = \frac{I_{ph}/q}{\Phi/h\nu} \quad 4\text{-}2$$

, where I_{ph} is the photocurrent ($I_{total} - I_{dark}$), q is the elementary charge, Φ is the incident radiant flux (W), and $h\nu$ is the photon energy (J). In practice, Φ is often obtained from the product of the incident radiant exitance $M(W/cm^2)$ and effective optical area of the detector $A_o(cm^2)$. The responsivity is the ratio of photo-current (photo-voltage) to the incident power (A/W or V/W), written as,

$$R = \frac{I_{ph}}{\Phi} = \frac{V_{ph}}{\Phi} = \frac{\eta_{ext} q}{h\nu} \quad 4\text{-}3$$

. Since the photocurrent proportionally increases as a function of the incident radiant flux, the responsivity is independent to the optical area of the detector under assumption that the optical area uniformly absorbs light along the detection plane.

4.2.2 Noise equivalent power

Noise equivalent power (NEP) is the power that can produce photocurrent signal equal to root mean square (rms) noise current of a detector, in other words, the minimum power that can be measured. It is defined as the ratio of the noise current to the responsivity,

$$NEP = \frac{I_n}{R} = \frac{\Phi}{I_s/I_n} = \frac{\Phi}{SNR} \quad 4\text{-}4$$

, where I_n is the noise current.

Several noise sources can be categorized based on nature of random fluctuation including shot, thermal, generation-recombination, and 1/f noise [101]. The effect of each noise source would be differently attributed as a limiting factor depending on the type of a detector. Thermal noise and shot noise are major noise sources affecting photodetector. Thermal Johnson noise is caused by the thermal fluctuation of charged carriers in a semiconductor regardless of application of an external bias. The shot noise is originated from the discrete (quantum) nature of photons in association with absorption process of electrons. The generation-recombination noise is due to random generation and recombination of charge carriers. 1/f noise is related to the

Schottky barriers at the metal-semiconductor interface. Including both shot and thermal noise sources, we can express the noise current as,

$$I_n = \sqrt{2q\left(I_{ph} + I_d\right)\Delta f + \frac{4kT\Delta f}{R_d}} \quad \text{4-5}$$

, where I_d is the dark current, Δf is the signal bandwidth, R_d is the dynamic resistance of a detector, and kT is the thermal energy. The first term of the right hand side is for the shot noise and the second term is for the thermal noise.

4.2.3 Detectivity

The detectivity D is defined from NEP as,

$$D = \frac{1}{NEP} \quad \text{4-6}$$

. Photocurrent is proportional to the optical area of a detector, whereas noise current is proportional to the square root of the optical area. Thus, NEP or the detectivity will be increased as a function of detector optical area, indicating they are not suitable metrics to compare sensitivity of detectors having different geometries.

The specific detectivity D^* , defined as the rms signal to noise ratio obtained in square root of a detector area in unit bandwidth per unit radiant flux, is the normalized detectivity taking into account the area and signal bandwidth of a detector. It is described by Jones [102], in unit of $cmHz^{1/2}/W$, expressed as,

$$D^* = \frac{\sqrt{A_d \Delta f}}{NEP} \quad \text{4-7}$$

, where A_d is the detector area or optical area, whichever smaller.

The background temperature is the temperature of any radiating sources seen by a detector except for the signal source. If the photon flux from the background temperature (background photon flux) is higher than the signal flux, the detector is in the condition as the background limited infrared performance (BLIP), meaning that the detector performance is limited by the noise of the background photons not by the noise aroused from the detector itself. The background limited detectivity is given by [103],

$$D^*_{BLIP} = \frac{\lambda}{hc}\sqrt{\frac{\eta}{2Q_B}} \qquad 4\text{-}8$$

. The photon flux Q_B is determined by the background temperature and the solid angle seen by the detector, which is expressed as,

$$Q_B = sin^2\,\theta \int_0^{\lambda_{cut}} Q(\lambda, T_B)d\lambda = sin^2\,\theta \int_0^{\lambda_{cut}} \frac{2\pi c}{\lambda^4[exp\,(hc/\lambda k T_B) - 1\,]}d\lambda \qquad 4\text{-}9$$

, where $\theta$is the field of view (FOV), and $Q(\lambda, T_B)$ (photon/cm^2/s/μm) is the photon emittance of a blackbody at a given temperature T_B. Figure 4.1 shows the calculated BLIP specific detectivity as a function of the peak wavelength. The calculation assumed the quantum efficiency of 100% and FOV of 90˚ (2π sr). As the background temperature decreases, D* increases due to decreased background photon flux at lower temperature. The minimum D* is located near 10 μm that is corresponding to the peak wavelength of 9.7 μm of the blackbody at 300 K.

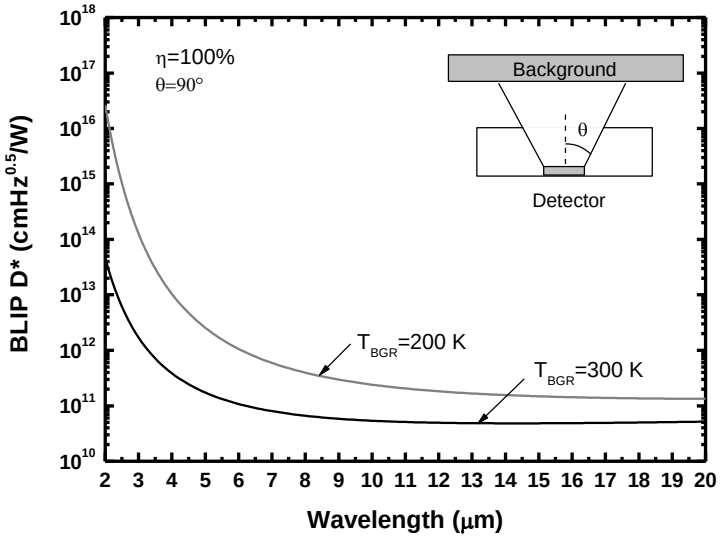

Figure 4.1 Calculated BLIP specific detectivity as a function of the peak wavelength at different background temperatures.

4.3 Characterization

The detectivity is the most important parameter of detector performance. To estimate the detectivity, several parameters have to be characterized (Figure 4.2). The resistance-area product can be estimated by taking derivative of dark current density vs. voltage curve. Spectral response

is usually measured using a FTIR with a calibrated light source. Noise current can be either calculated using the equation 4-5 or measured using a spectrum analyzer [104].

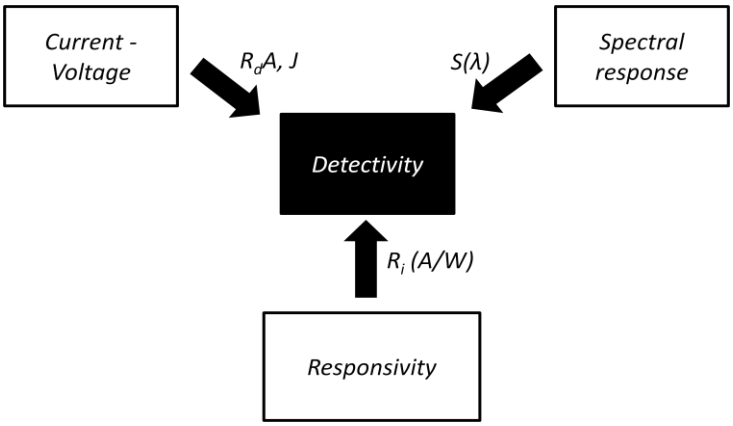

Figure 4.2 Related parameters for characterization of the specific detectivity.

Figure 4.3(a) illustrates the system diagram of the responsivity measurement. A blackbody radiator is the useful reference source that can provide an absolute value of radiance ($W/cm^2/sr$), defined as radiant flux density per unit solid angle,

$$L = \frac{\partial^2 \Phi}{\partial \Phi \partial A cos\theta} \qquad 4\text{-}10$$

. A blackbody is a perfect Lambertian source that gives a constant radiance regardless of viewing angle θ. The area of a point source subtended by the viewing angle is a function of cosine so that a Lambertian source follows the so-called cosine law. Thus, the intensity (W/sr) in the direction of the normal to the emitting plane, I_n decreases as $I_n \cos(\theta_s)$, where θ_s is the viewing angle from the normal to the plane. By integrating radiance over solid angle, radiant exitance can be obtained using,

$$M = \frac{d\Phi}{dA} = \int Lcos(\theta) d\Omega = \int_0^{2\pi} d\phi \int_0^{\pi/2} Lcos(\theta_s)\, sin(\theta)\, d\theta = \pi L \qquad 4\text{-}11$$

. It shows that for a Lambertian source, radiant exitance is π multiplied by radiance. If a light source is not Lambertian, radiance L is a function of θ_s so that it cannot be pulled out of integral.

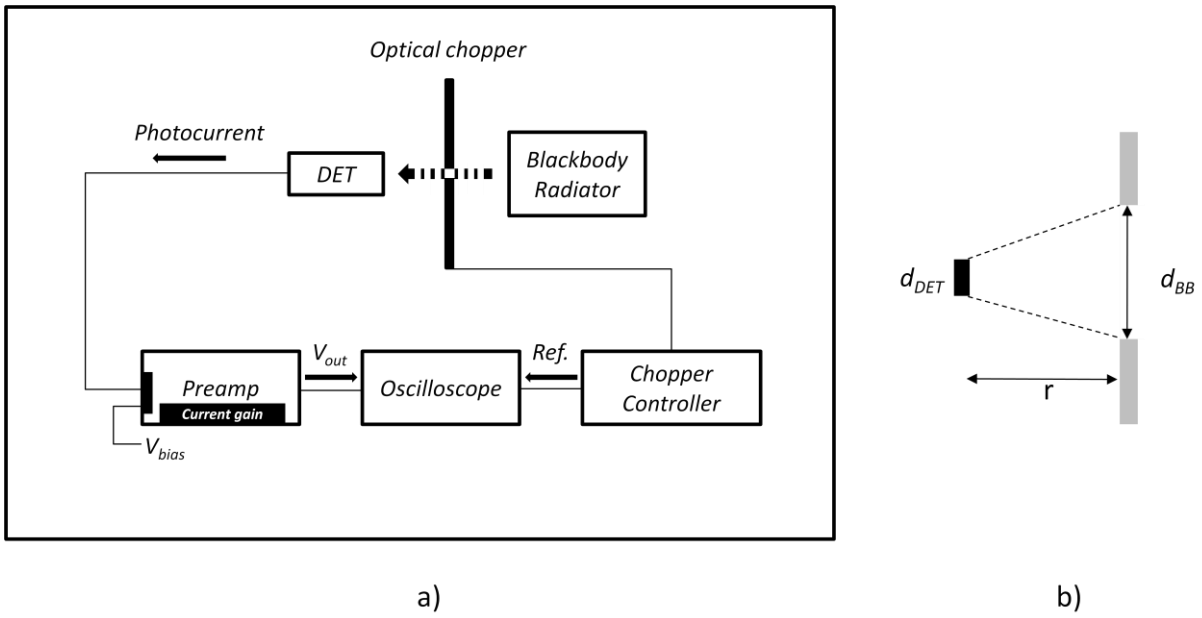

Figure 4.3 (a) The system diagram of the responsivity measurement, (b) configuration of the detector and blackbody.

If a viewing angle is small enough and the distance between the blackbody and photodetector is long enough ($r>>d_{BB}$), the emitting surface projected to the detector can be assumed to be flat within small angle (Figure 4.3(b)). Radiant flux seen by the detector can thus be simplified as,

$$\Phi = L\Omega A_{DET} = L\frac{A_{DET}A_{BB}}{r^2} \qquad 4\text{-}12$$

. Responsivity is the ratio of photocurrent to incident power into a photodetector. Using the small angle approximation, incident power seen by a photodetector from a blackbody can be expressed as,

$$P_{inc} = \frac{A_{DET}A_{BB}}{r^2}\int_0^\infty R_{norm}(\lambda)L(\lambda,T)d\lambda \qquad 4\text{-}13$$

. A_{DET} is a detector area, A_{BB} is a blackbody aperture area, r is the distance between the detector and blackbody, $R_{norm}(\lambda)$ is the normalized photo response of the detector, and $L(\lambda,T)$ is spectral radiance of a blackbody in units of W/cm^2/μm/sr, which is defined using the Planck equation as,

$$L(\lambda,T) = \frac{2hc^2}{\lambda^5}\left[exp\left(\frac{hc}{\lambda kT}\right)-1\right]^{-1} \qquad 4\text{-}14$$

. If one uses spectral radiant exitance, $M(\lambda,T)$ in units of W/cm^2/μm, $M(\lambda,T)=\pi L(\lambda,T)$ for a Lambertian source should be noted. The detector area could be the mesa area or optical opening area depending on the detector geometry. Using the definition of responsivity and equation 4-13, the peak responsivity can be expressed as,

$$R_{peak}=\frac{I_{ph}}{P_{inc}}=\frac{I_{ph}}{\frac{A_{DET}A_{BB}}{r^2}\int_0^\infty R_{norm}(\lambda)L(\lambda,T)d\lambda} \qquad 4\text{-}15$$

, where I_{ph} is the rms photo current; for square output signal, $I_{ph}=0.5I_{pp}$. The spectral responsivity of a photodetector $R(\lambda)$ is $R(\lambda)=R_{peak}R_{norm}(\lambda)$.

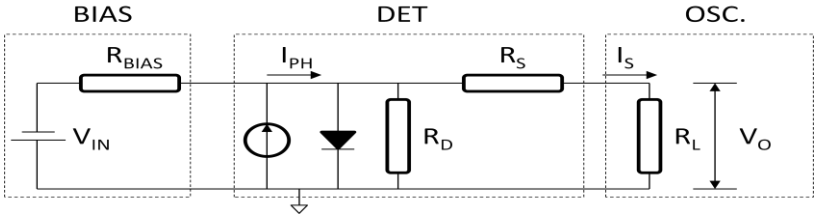

Figure 4.4 The equivalent circuit of the photocurrent measurement system without the preamplifier.

Two measurement systems for the photocurrent characterization are presented. Figure 4.4 shows the equivalent circuit of the photocurrent measurement system without a preamplifier. For the photovoltaic mode, the bias stage can be omitted. V_{IN} is the bias voltage from a power source, R_{BIAS} is a bias resistance, R_D is a shunting resistance, R_S is a series resistance, R_L is a load resistance, V_O is a output voltage from a oscilloscope, I_{ph} is photocurrent, and I_S is signal current. The shunting resistance is originated from current path out of the detector, such as surface current. The series resistance is from resistance of semiconductor neutral region and the Schottky barrier at the metal-semiconductor interface. In an ideal diode or photodetector, R_D is infinite and R_S is zero so that the photocurrent flows mostly through the load resistance. In order not to draw the photocurrent into the power source, R_{BIAS} has to be large enough compared to R_D. Using the Kirchhoff's law, I_{ph} can be expressed as,

$$I_{ph}=I_S\frac{R_D+R_S+R_L}{R_D}=\frac{V_O}{R_L}\frac{R_D+R_S+R_L}{R_D} \qquad 4\text{-}16$$

. If the $R_L>>R_D, R_S$, $I_{ph}\sim\frac{V_O}{R_D}$.

The equivalent circuit of the measurement system with the preamplifier is shown in Figure 4.5. The photocurrent I_{ph} can be found using the equation following,

$$I_{ph} = -\frac{V_O}{R_f}\left(1 + \frac{R_S}{R_D}\right) \qquad 4\text{-}17$$

, and if $R_D >> R_S$, $I_{ph} \sim -\frac{V_O}{R_f}$. Using the preamplifier, one can obtain higher signal to noise ratio so that the measurement system does not suffer from the low signal amplitude of photocurrent that limits the measurement accuracy. Figure 4.6 shows the photocurrent measured with or without the preamplifier. A photodetector was illuminated by a 700 ˚C blackbody placed 2 cm away from the detection plane. The result measured without the preamplifier shows smaller photocurrent at low reverse bias voltage and becomes similar at high bias voltage to the photocurrent measured with the preamplifier. Thus, to obtain accurate value at low photocurrent level, the preamplifier should be used.

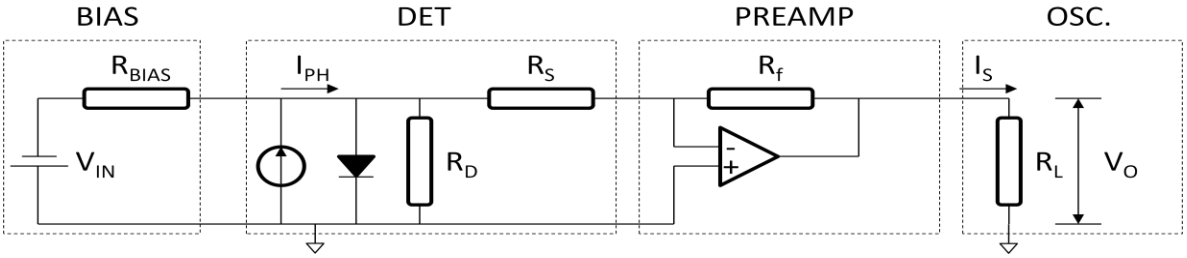

Figure 4.5 The equivalent circuit of the photocurrent measurement system with the preamplifier.

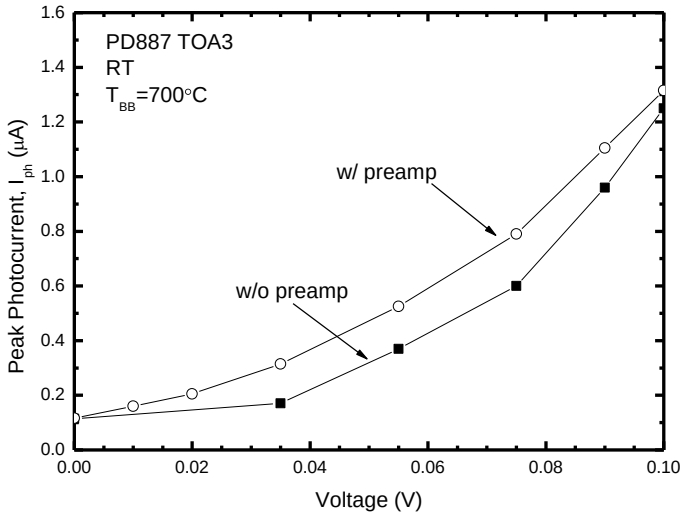

Figure 4.6 Photocurrent as a function of the reverse bias voltage, measured with or without the preamplifier.

4.4 Results and discussion

4.4.1 Introduction

'nBn' detector is a new type of photodetectors recently proposed by Maimon and Wicks [5]. The 'nBn' addresses 'n'-type absorber, Barrier, and 'n'-type contact layer. In simple term, the operation of the nBn detector can be thought of as a photoconductor with a barrier layer. The barrier effectively blocks the majority carrier electrons from the n-contact layer but minority carrier holes can freely move along the structure with the condition of flat valence band offset. Note that the pronounced conduction band offset and zero valence band offset at the barrier interfaces. Applying the same principle, one can readily devise 'xBx' type of photodetectors by carefully choosing conduction type and materials with suitable band offsets. The major advantages of the nBn detector over the conventional p-n or p-i-n photodiode are 1) twofold higher operating temperature due to diffusion limited dark current regime, 2) formation of natural passivation layer that suppresses surface current, and 3) simple heterostructure design.

Many numerical and experimental results on the nBn type photodetectors have been demonstrated. The orginal nBn paper presented the BLIP temperature of ~230 K from the detector with the InAs absorber grown on the InAs substrate. Krishna group in Univ. of New Mexico demonstrated nBn detectors with type II InAs/GaSb superlattice absorbers grown on n-type GaSb substrates. The detectors with 5.2 μm cut off wavelength and detectivity of ~10^9 cm$Hz^{0.5}$/W at 300 K have been reported [105]. The lateral diffusion length of minority carrier holes in the InAsSb absorber was estimated using the variable area detector array, suggesting the lateral diffusion length of 7 μm at 240 K [106] . The numerical models have been demonstrated by Schuster *et al.* [107] with analysis of the effect of barrier layer doping on detector performance.

In this section, we will describe the fabrication procedure to reduce dark current and compare the performance of nBn and nBp detector with various contact geometries to improve the quantum efficiency.

4.4.2 Design, growth and fabrication

Figure 4.7 shows the nBn and nBp band diagram under the thermal equilibrium condition. The Fermi level is corresponding to zero energy level (dashed line). The material

parameters used for the simulation are listed in Table 4-1 and Table 4-2. PADRE was used to solve the Poisson equation. The band bending is mostly occurred across the barrier layer whose electron band offset is high enough to block the thermally excited electrons from the contact layer. This situation especially affects less depletion width on the nBn structure. The depletion width of the absorber is about 50 nm for the nBn and 200 nm for the nBp. The wider depletion region in the nBp detector is due to the thermally excited holes can be injected from the p-contact layer while the negligible hole concentration in the n-contact layer of the nBn detector does not contribute to the significant carrier depletion near the absorber-barrier interface. The absorber thickness can be determined based on the limiting lengths: the diffusion length of minority carrier (for nBn case, hole) and absorption length of a target wavelength. Taking into account the hole diffusion length of ~10 μm at room temperature and the absorption ength of 5 μm we choose the absorber thickness ~2 μm.

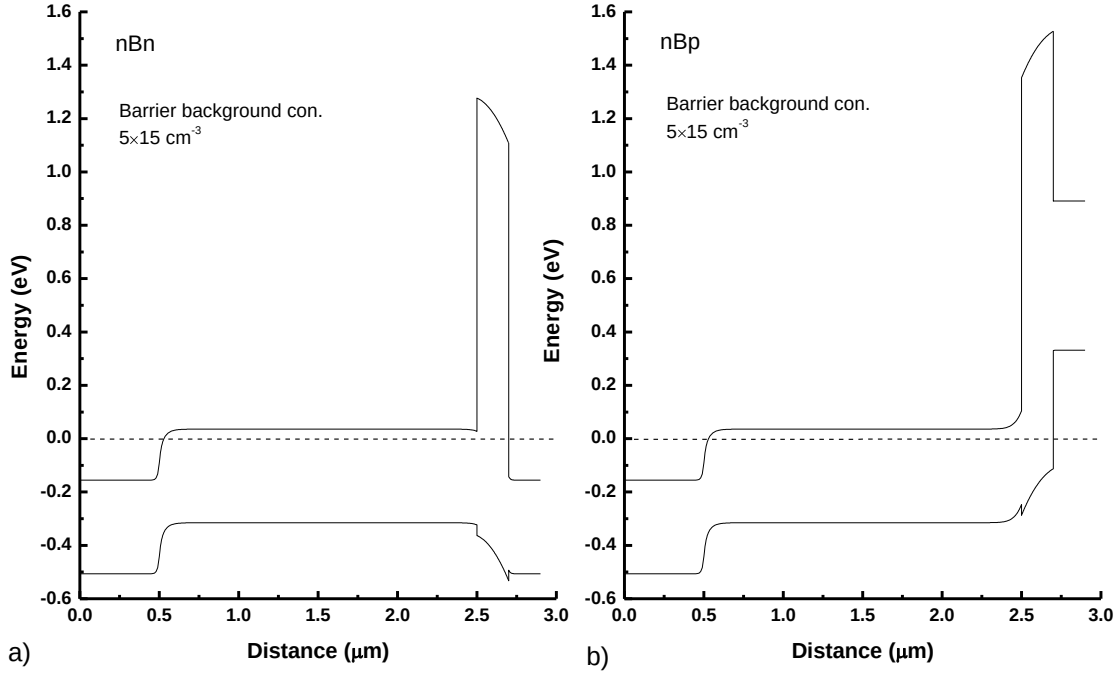

Figure 4.7 Calculated band diagram of the nBn (a) and nBp (a) detector. The horizontal dashed line indicates the Fermi level.

Table 4-1 Heterostructures of the nBn and nBp detector [30, 107].

Sample	Substrate	Absorber		Barrier		Contact	
	(cm^{-3})	t (nm)	(cm^{-3})	t (nm)	(cm^{-3})	t (nm)	(cm^{-3})
nBn	InAs	InAs		$AlAs_{0.16}Sb$		InAs	
	n:1e18	2000	n:2e16	200	p:5e15	200	n:1e18
nBp	InAs	InAs		$AlAs_{0.16}Sb$		$In_{0.2}GaAs_{0.26}Sb$	
	n:1e18	2000	n:2e16	200	p:5e15	200	p:2e19

Table 4-2 Material parameters used for the band structure simulation [108].

Material	E_g (eV)	N_C (cm^{-3})	N_V(cm^{-3})	μ_n (cm^2/V/s)	μ_p (cm^2/V/s)	ε_s
InAs	0.351	8.7e16	6.6e18	3000	900	15.15
$AlAs_{0.16}Sb$	1.640	4.76e16	2.07e17	–	–	–
$In_{0.2}GaAs_{0.26}Sb$	0.560	1.57e17	5.75e17	1000	100	–

The operating bias condition is the negative bias on the contact layer that we define as a reverse bias. Photo-excited electrons and holes generated in the absorber layer move to substrate and contact layer, respectively. Charge neutrality can be maintained when the separated carriers meet each other through the external circuit and contribute to photocurrent. For the nBp structure, we may expect higher photocurrent than that of the nBn structure due to the presence of stronger electric field in the nBp barrier layer that can facilitate the charge separation. As shown in Figure 4.7, the opposite direction of the band bending at the contact layer will affect the collection efficiency. For example, the only photoexicited holes that overcome the barrier energy of ~200 meV will contribute to the photocurrent in the nBn structure while the electric field at the contact-barrier interface of the nBp is in the same direction of the operating bias that will facilitate the carrier collections at the top contact. The valence band offset of the nBn and nBp structure is meant to be zero but there is a uncertainty of the actual band offset that may hinder the carrier transport and if so both nBn and nBp will be affected in the same degree, since we employed the same materials except for the contact layer.

The nBn and nBp photodetector structure was grown on n^+-InAs ($1 \sim 3\times10^{18}$ cm^{-3}) substrates by using a Veeco Gen 930 solid source MBE system. A 2000 nm thick InAs absorber layer was grown on a 500 nm thick Te doped (1×10^{18} cm^{-3}) InAs buffer layer. After the absorber layer, a 200 nm thick $AlAs_{0.16}Sb_{0.84}$ barrier layer and 200 nm thick $In_{0.20}Ga_{0.80}As_{0.26}Sb_{0.74}$ cap layer (Be: 2×10^{19} cm^{-3}) lattice matched to InAs have been grown. For the nBn detector, the InAs

n-contact layer was grown with the same thickness and doping level. The absorber and barrier layer were unintentionally doped.

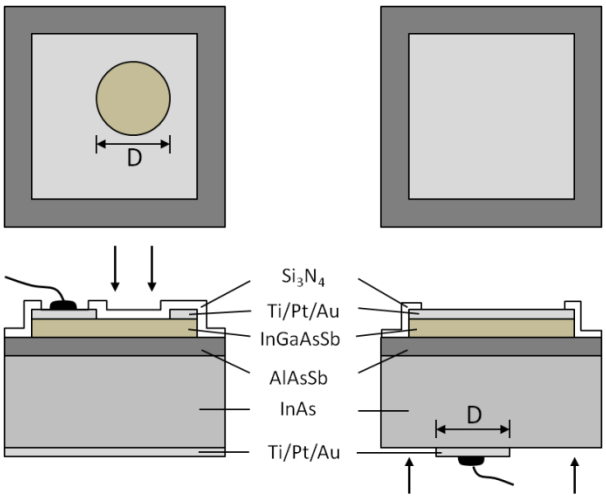

Figure 4.8 Device geometry for the front-illumination (left) and back-illuminated (right) scheme. D is the diameter of the top aperture or back contact varied from 350 μm to 80 μm.

The grown wafers were processed into a single device with the die size of 600×600 μm^2. In order to find the responsivity dependence on optical aperture size, various contact areas with the same mesa size of 520×520 μm^2 have been introduced either on epi- or substrate- contacts (Figure 4.8). For the front-illumination, a circular aperture with the diameter varying from 350 μm to 80 μm was formed in the top contact, while a circular metal contact with the same variation was formed on the substrate side for the back-illumination. Both top and bottom metal contacts consisted of Ti 200 Å /Pt 1000 Å /Au 1000 Å layers. Wet etching with a tartrate-based solution was performed to remove the side of the contact layer. The etching was stopped as soon as the contact layer was removed and Si_3N_4 dielectric passivation layer covered the exposed AlAsSb region to prevent oxidation. As proposed in the initial nBn paper, devices without the passivation were working but only for the short period time: about a month for our case. Thus, we had to introduce the passivation process for long-term device lifetime. The non-passivated devices became like shunting resistors probably due to barrier layer breakage. The wafers were thinned down to the thickness of ~150 μm and cleaved single devices were mounted on TO packaging holders for characterization.

Figure 4.9 shows the current density (current/the top metal area) vs. voltage characteristics of the etched and non-etched detector. The etched device generated about 3 orders of magnitude less dark current density than the non-etched one. Thus, the advantage of low dark

current characteristic from this type of detectors may not be exploited without etching the edge of the contact layer. Non-etched devices did not show any rectifying characteristic but ~20 Ω series resistance.

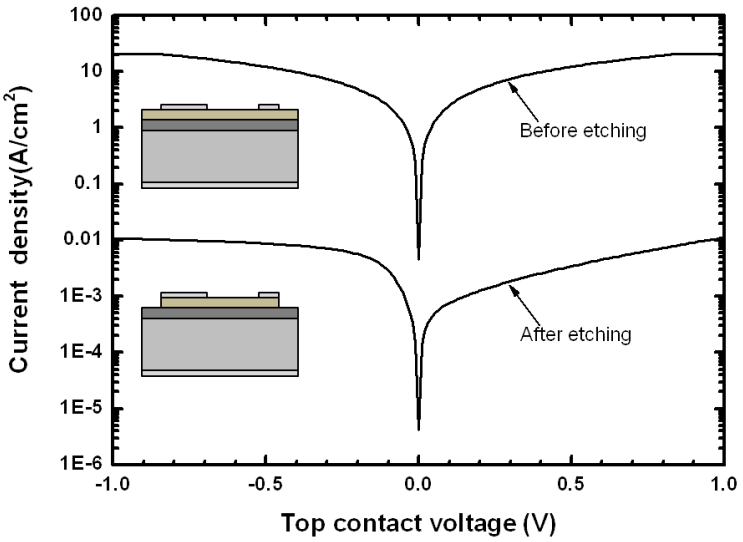

Figure 4.9 Room temperature current density vs. voltage characteristics for the etched and non-etched photodetector.

4.4.3 nBn vs. nBp detector

Figure 4.11 shows the photo-response of the nBn and nBp detectors measured at various temperatures. Both detectors have the mesa area of 520×520 μm^2. To carry out the comparison in a well-controlled system, both detectors mounted in the same cryostat were zero biased and the device temperature was the only control parameter. Thus, any difference in the photoresponse results would be caused by the contact layer difference since both devices were grown and fabricated in the same manner except for the contact layer. Photo-signal was collected using a Nicolet Magna 860 FTIR and installed glow bar of which effective temperature was calibrated using an InSb detector and blackbody radiator. The effective temperature of 1200 ˚C of the glow bar was found. The example calibration procedure is shown in Figure 4.10. For the nBp, the intensity of the peak photoresponse increased from 330 K to 125 K and below 125 K it abruptly decreased. For the nBn, the peak intensity drop occurred at 270 K. As temperature decreases, the cut off wavelengths of both detectors, defined as the long wavelength at 5% of the peak intensity, move toward shorter wavelength with the rate of -4.2 nm/K between 330 K and 225 K and with

the rate of -2.65 nm/K between 225 K and 80 K. The nBn detector was measured up to 125 K due to significant signal drop below the temperature. Distortion near 1.8 μm and 2.7 μm is due to water absorption.

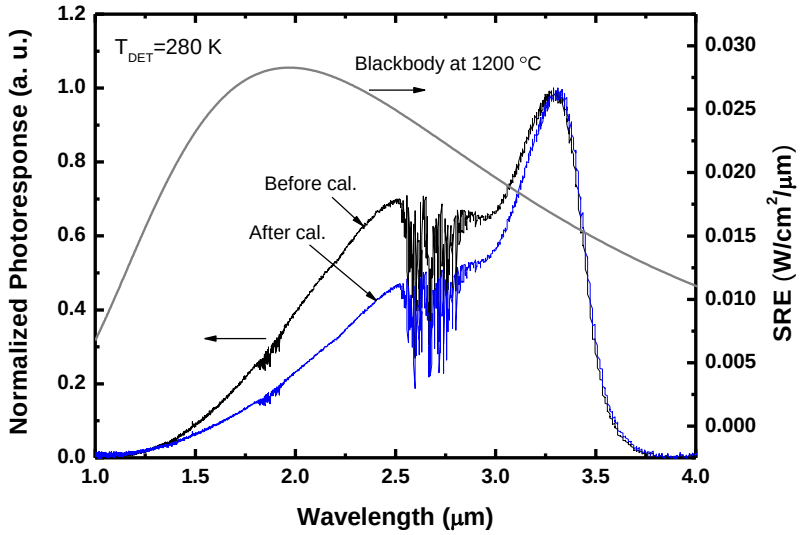

Figure 4.10 Calibration of the photoresponse signal obtained by using a glow bar as a light source. The effective temperature of 1200 ˚C of the glow bar is estimated using the InSb detector and blackbody radiator.

The effect of the contact layer with different conductivity on the detector performance is clearly revealed in the relative responsivity obtained by integrating the photoresponse over the wavelength range. Figure 4.12 plots the relative responsivity normalized by the value at 300 K. The responsivity of the nBn detector gradually decreases as temperature decreases and the maximum responsivity is obtained at 320 K. This is direct indication that the photo excited holes in the absorber layer have to overcome the band bending energy to reach the top contact layer with help of thermal energy. Thus, the responsivity of the nBn detector increases with increase of the device temperature. The absence of the energy barrier in the nBp structure allows the responsivity to be improved with decrease of device temperature. However, the responsivity was abruptly decreased below 125 K. The non-zero VBO near the absorber-barrier interface is possibly responsible for this situation that suggests the VBO of ~10 meV. Since this effect should affect both detectors, the signal drop below 125 K on the nBn detector is predominantly relevant to this. Figure 4.13 shows the dark current density dependent as a function of

temperature. From 0 to -0.2 V, dark current density increased in the super-linear relation and below -0.2 V both detectors showed nearly constant dark current density. The activation energy of 488 meV, corresponding to the bandgap energy of InAs, is obtained from both detectors in the temperature range between 330 K and 200 K. This confirms both detectors are diffusion current limited within this temperature range.

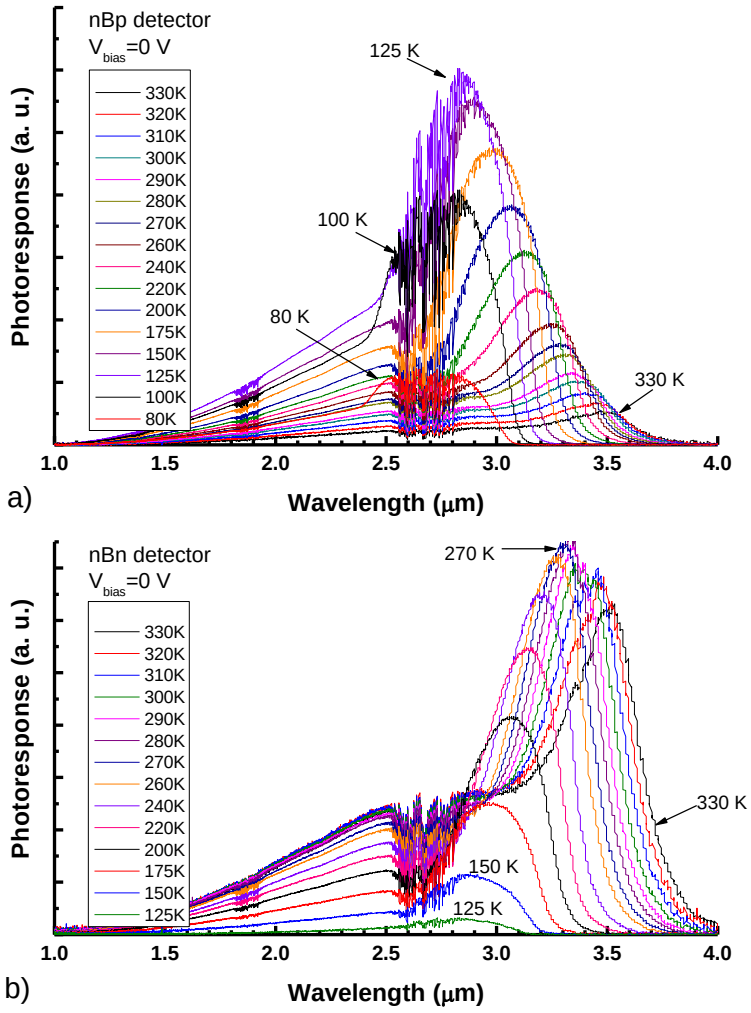

Figure 4.11 Photo-response of the nBp (a) and nBn (b) detector measured at various temperatures. V_{bias}=0 V for both detectors.

Figure 4.15 shows the responsivity measured at room temperature. A Blackbody radiator emitting at 700 ˚C illuminated light into the optical aperture of both detectors having the same diameter of 150 μm. The incident light was chopped at 500 Hz. Photocurrent was amplified through a Stanford trans-impedance amplifier and measured from an oscilloscope. As the

negative bias voltage increased, the responsivity of both detectors increased. Initial abrupt increase at the bias range between 0 V and -0.2 V corresponds to the dark current range in the superlinear increase, indicating that the applied bias is consumed to reduce the band bending energy as well as the barrier at the metal-semiconductor interface due to potential imperfection of Ohmic contacts. The responsivity of both detectors became saturated at the bias voltage above -0.5 V but with twofold difference magnitude. The fact that the nBp detector required less voltage than the nBn detector to reach the same responsivity suggests that the p-type contact layer can provide better voltage efficient. The responsivities as high as 0.09 A/W for the nBn and 0.18 A/W for the nBp were obtained at -1 V.

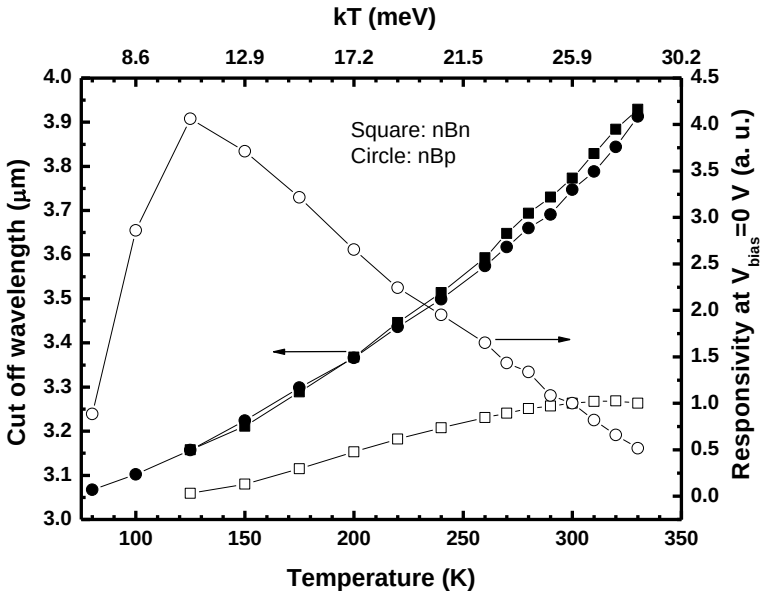

Figure 4.12 The cut off wavelength and relative responsivity at zero bias as a function of temperature. Top x-axis is the thermal energy corresponding to the bottom x-axis. Square is for the nBn and circle is for the nBp.

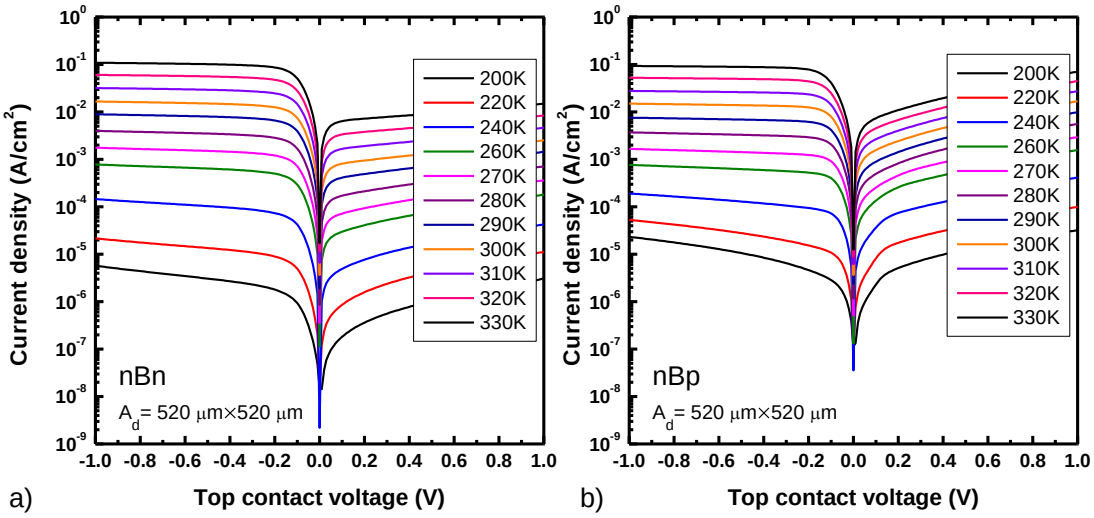

Figure 4.13 Dark current density measured at different temperatures for the nBn (a) and nBp (b) detector.

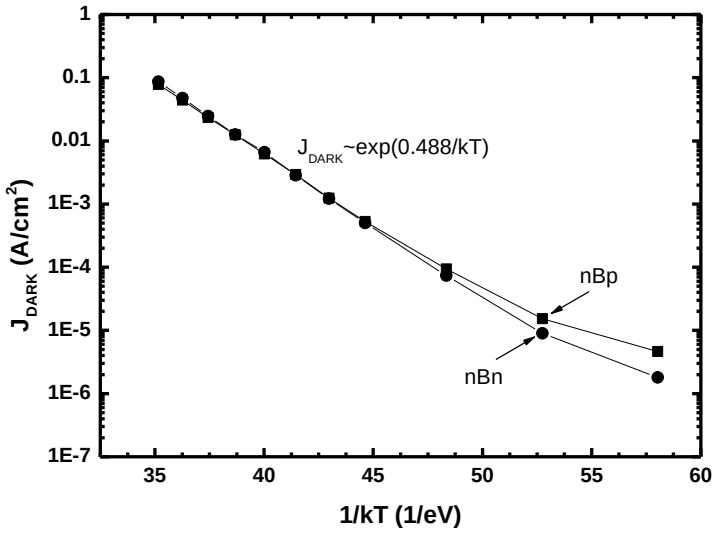

Figure 4.14 Dark current density as a function of 1/kT for the nBn (circle) and nBp (square) detector. The similar activation energy of 488 meV is obtained from both detectors.

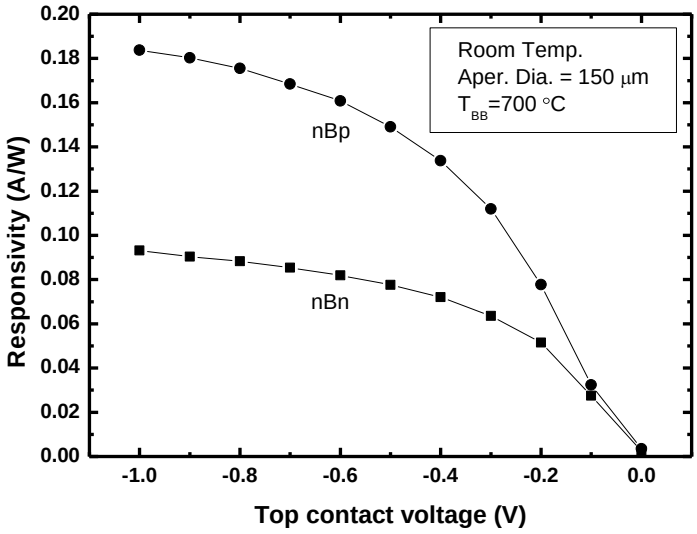

Figure 4.15 The responsivity of the nBn and nBp detector measured at room temperature with a Blackbody emitting at 700 ˚C. The aperture diameter is 150 μm for both detectors.

4.4.4 Front- and back-illumination

Advantages of the back-illumination scheme include minimal obscuration of incident light and circumvention of epi-layer damage during wire bonding process. High electron concentration at the n-type InAs surface (Fermi level pinning) allows applying back contact as small as possible, which may be difficult to realize on the top-contact side because the lateral carrier motion may be limited within the relatively thin n+ (or p+) contact layer. A way to create spectral window within the same substrate and absorber material, i.e. the InAs absorber on the InAs substrate, is to use the Burstein-Moss effect: apparent bandgap change due to carrier concentration change in a material. Thus, introducing the doping difference between the substrate and absorber can control the spectral transmission for a desired wavelength and simultaneously provide natural spectral band pass filter for the target wavelength [109].

Figure 4.16 shows the normalized photo-response of the nBp detectors measured at room temperature. Apparent difference on the spectral bandwidth between front- and back-illumination schemes was obtained. Both detectors show the cut off wavelength of ~3.7 μm that is corresponding to the absorption edge of undoped InAs. The cut-on wavelength of the front-

illuminated detector of ~1.2 μm is limited by the AlAsSb barrier but that of the back illuminated detector of ~2.9 μm is limited by the substrate absorption edge. The peak wavelength of the front detector is about 2.4 μm corresponding to the band gap energy of the contact layer, while that of the back detector is 3.3 μm which is exactly matched to CH_4 peak absorption region. Full width at half maximums are 1.59 μm and 0.41 μm for the front- and back- detector, respectively.

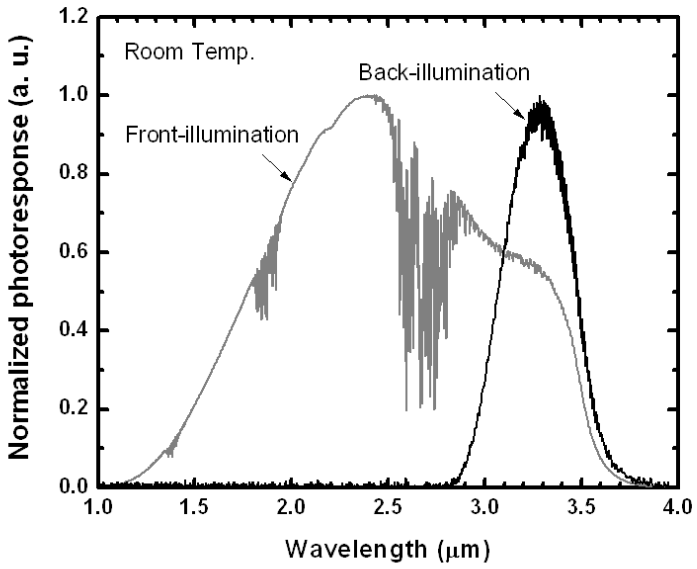

Figure 4.16 Normalized room temperature photoresponse from the front- and back-illuminated detector.

The absorption coefficients of the InAs substrate and absorber layer were estimated by comparing the transmittance of the samples listed in Table 4-3. A part of the detector wafer was cleaved and polished to introduce sample thickness difference. By taking the ratio of the transmittance between the sample 3 and 4, we estimated the absorption coefficient of the InAs substrate, which was also used as a reference value for the comparison of the sample 1 and 2. Absorption through the barrier and contact layer is assumed negligible due to high bandgap energy and small thickness. At 0.375 eV (3.3 μm), the absorption coefficients of the InAs substrate and absorber layer were obtained as 25 cm^{-1} and 2050 cm^{-1}, respectively. Similar values were obtained from LPE grown InAs substrates by Dixon and Ellis [110]. The two orders of magnitude difference between the coefficients ensures that the heavily doped substrate can

provide reasonably transparent substrate near λ~3.3 μm. Increase of the absorption coefficient at low energy side is due to free carrier absorption [27].

The absorption length of the undoped InAs layer can be estimated to be about 5 μm. Since the diffusion length of minority carrier in the undoped InAs is about 10 μm [5], thicker absorber layer can be utilized to increase the responsivity. Taking into account the hole diffusion length of >10 μm, the absorption length of ~5 μm would be the upper limit of the absorber thickness.

Table 4-3 The nBp detector samples for the absorption coefficient measurement.

Sample	Layers	Thickness (μm)
1	Active + InAs substrate	118
2	Active + InAs substrate	285
3	InAs substrate	144
4	InAs substrate	283

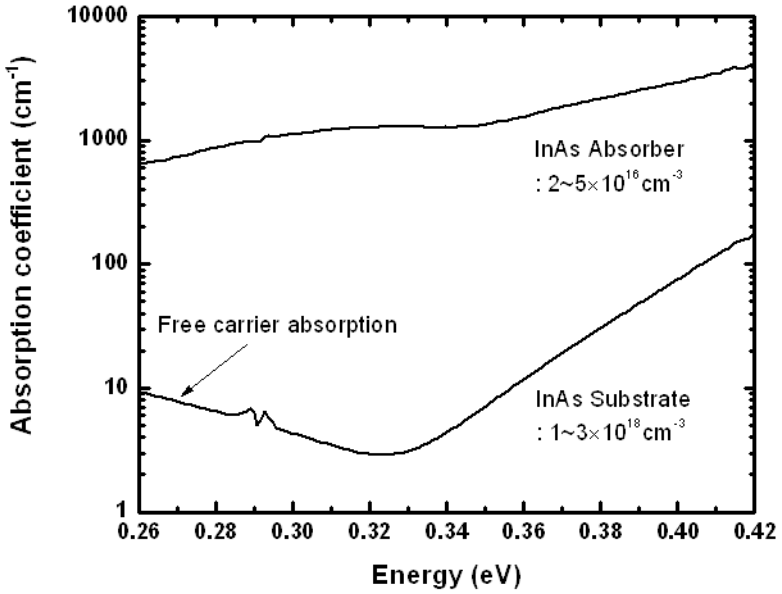

Figure 4.17 Absorption coefficients of InAs with different doping concentrations.

The responsivity at λ=3.3 μm as a function of the top contact bias is shown in Figure 4.18. The optical area was estimated by subtracting the contact area from the detector area. The back illuminated detector showed about 60% higher responsivity than the front detector. Both

detectors reached the saturation at -0.2 V, which was possibly due to the same reasons mentioned in the previous section. The shot noise limited specific detectivity is estimated by plugging the equation 4-4 and 4-5 into the equation 4-7, written as,

$$D^* = \frac{R}{\sqrt{2qJ_{tot} + \frac{4kT}{R_d A_d}}} \qquad 4\text{-}18$$

, where R is the responsivity, q is the elementary charge, J_{tot} is total current density, kT is thermal energy, R_dA_d is the dynamic resistance detector area product.

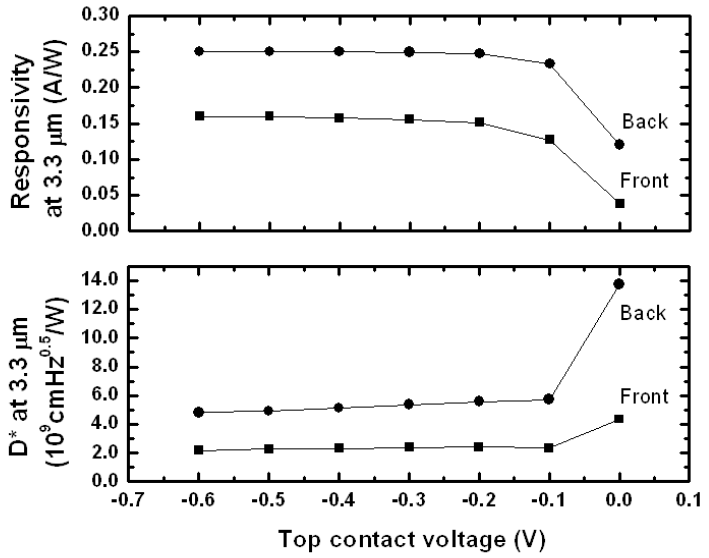

Figure 4.18 The peak responsivity and specific detectivity at 3.3 μm measured at room temperature using a blackbody operating at 700 ˚C and the chopper modulating at 500 Hz. Square: front-illumination; circle: back-illumination.

The responsivity dependence on different optical aperture area is shown on Fig. 4.19. The maximum responsivity at λ=3.3 μm was obtained from the detectors with largest opening area for both front- and back-illumination scheme. In ideal case, the responsivity may be the same regardless of the size of the optical area unless incident power is non-uniformly scaled. Experimental results show that the larger the optical area the higher the responsivity. Such increase of the responsivity as a function of the optical area would be counterintuitive; the increase of the photocurrent is faster than the incident power increase. It may be attributed to the

non-uniform quantum efficiency across the lateral direction, efficiency at the center of the optical area higher than that near metal contact.

To fully understand this result, effect of lateral current diffusion and local sensitivity should be investigated, which we shall leave for the future work. However, in design point of view the smaller metal contact with the back illumination scheme is favored to achieve the maximum responsivity.

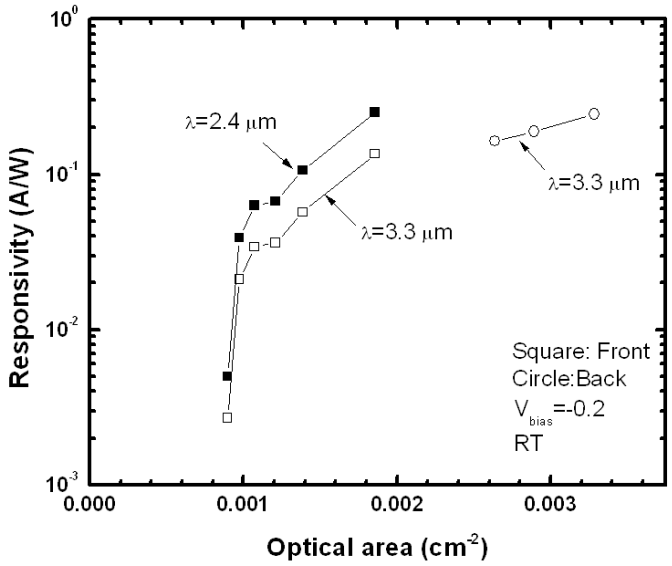

Figure 4.19 The responsivity dependence on optical area of the front- (square) and back- (circle) illuminated detectors measured at room temperature. Closed square is the peak responsivity obtained at λ=2.4 μm and open one is the peak responsivity at 3.3 μm. The bias voltage was -0.2 V.

4.4.5 LED-Detector optopair

Figure 4.20 shows the LED electroluminescence and detector photo-response together with the methane gas absorption spectrum. The LED structure is based on the type I QW active region introduced in Chapter 2. The methane absorption spectrum was obtained from the transmission measurement using the FTIR and methane gas cell. The absorption peak of methane gas is well matched to the peak sensitivity of LED and detector so that the presence of methane in the optical path between the LED and detector will introduce LED signal drop that can be converted to the amount of gas.

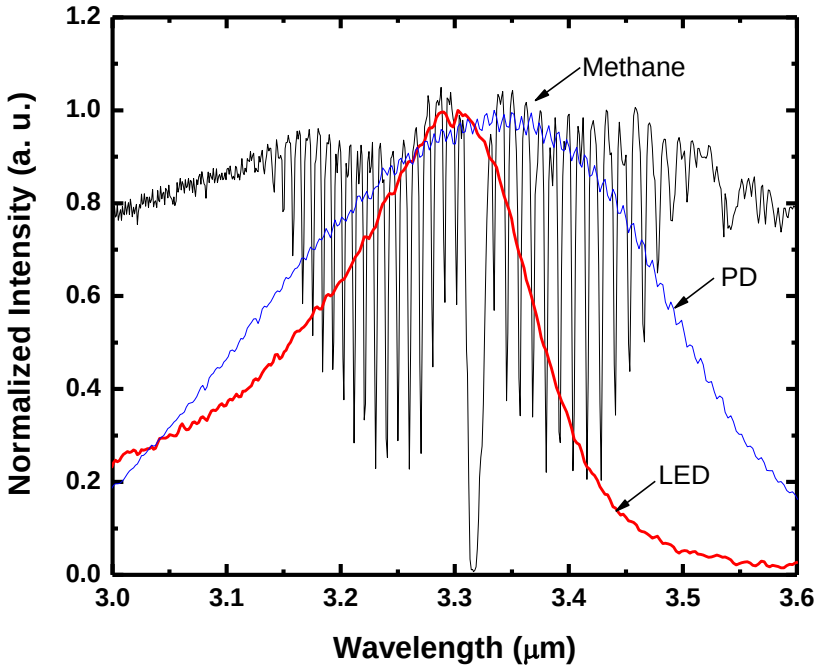

Figure 4.20 Normalized LED electroluminescence, detector photoresponse, and methane absorption spectrum.

4.5 Conclusion and future work

Opto-pairs with the new type of detectors and type I QW LEDs has been developed for the methane gas sensing application. The technological breakthrough on the InAs based nBn type detector is the demonstration of back-illuminated nBp detector consisting of the same absorber and substrate. Narrow spectral bandwidth that perfectly matches to the methane absorption peak has been realized using the Burstein-Moss effect describing absorption edge change dependent on doping concentration in the same material. Such back-illumination allows to effectively avoid epi-layer damaging during wire-bonding process and to improve responsivity about 70% compared to the front-illumination scheme.

We have also compared the performance of the nBn and nBp detectors with respect to the different contact layers. Overall, the detector with the p-type contact layer showed better performance. Both detectors exhibited the similar peak sensitivity at the wavelength of 3.3 μm at room temperature and the activation energy of 0.488 eV corresponding to the bandgap energy of the InAs absorber, confirming that the dark current was limited by the diffusion process. However, the opposite direction of the band bending that was caused by the contact layer led to the photoresponse increase in the nBp detector as the device temperature decreased up to 125 K, while the photoresponse of the nBn detector gradually decreased under the same temperature change. The abrupt signal drop below 125 K for both detectors was attributed to the non-flat VBO that impedes the transport of the photo-excited holes, which suggests the VBO of ~ 10 meV at the absorber and barrier interface. The nBn and nBp detector showed the responsivity of 0.08 A/W and 0.16 A/W at the bias voltage of -0.5 V with dark current densities of 1.6×10^{-2} A/cm^2 and 1.4×10^{-2} A/cm^2, respectively.

Performance comparison on detectors with front- and back-illumination scheme has been carried out at room temperature. The room temperature responsivities (specific detectivities) at 3.3 μm for front- and back-illumination are 0.13 A/W (2×10^9 cmHz$^{0.5}$/W) and 0.25 A/W (5×10^9 cmHz$^{0.5}$/W), respectively. The responsivity dependence as a function of the optical area suggests that the higher responsivity can be obtained in the lager optical area regardless of the illumination scheme. The back-illumination scheme is preferred since it can offer large optical area, narrower photoresponse, and no wire-bonding on the epi side.

The development of the photodetector for this particular wavelength is ultimately to realize the optical methane gas sensors with high sensitivity and high temperature tolerance. To

increase the responsivity, the absorber thickness can be further optimized taking into account the absorption length of 5 μm. Thus, we shall try to perform the experiment with various absorber thicknesses of 1 μm, 3 μm, and 5 μm. In addition, the ‘xBx’ concept can be applied by using the pBp or pBn detectors that will use electrons as minority carriers with several orders of magnitude higher mobility. For improved temperature tolerance, we may consider intentional mismatch of an emitter and detector sensitivity to maintain the nearly consistent sensitivity with a certain range of temperature variation.

References

1. Hall, R.N., et al., *Coherent Light Emission From GaAs Junctions.* Physical Review Letters, 1962. **9**(9): p. 366-368.

2. Nathan, M.I., et al., *Stimulated emission of radiation from GaAs p-n junctions.* Applied Physics Letters, 1962. **1**(3): p. 62-64.

3. Holonyak, J.N. and S.F. Bevacqua, *Coherent (visible) light emission from Ga($As_{1-x}P$) junctions.* Applied Physics Letters, 1962. **1**(4): p. 82-83.

4. Lawson, W.D., et al., *Preparation and properties of HgTe and mixed crystals of HgTe-CdTe.* Journal of Physics and Chemistry of Solids, 1959. **9**(3–4): p. 325-329.

5. Maimon, S. and G.W. Wicks, *nBn detector, an infrared detector with reduced dark current and higher operating temperature.* Applied Physics Letters, 2006. **89**(15): p. 151109-3.

6. Smith, S.D., et al., *The Prospects of LEDs, Diode Detectors and Negative Luminescence in Infrared Sensing of Gases and Spectroscopy.* Philosophical Transactions: Mathematical, Physical and Engineering Sciences, 2001. **359**(1780): p. 621-634.

7. Zhurtanov, B., et al., *High-efficiency 3.4–4.4 μm light-emitting diodes based on a p-AlGaAsSb/n-InGaAsSb/n-AlGaAsSb heterostructure operating at room temperature.* Technical Physics Letters, 2001. **27**(3): p. 173-175.

8. Kizhayev, S.S., et al., *Powerful InAsSbP/InAsSb light emitting diodes grown by MOVPE.* Journal of Crystal Growth, 2003. **248**(0): p. 296-300.

9. Danilova, T., et al., *Light-emitting diodes based on GaSb alloys for the 1.6–4.4 μm mid-infrared spectral range.* Semiconductors, 2005. **39**(11): p. 1235-1266.

10. Astakhova, A., et al., *High-power InAs/InAsSbP heterostructure leds for methane spectroscopy (λ ≈ 3.3 μm).* Semiconductors, 2010. **44**(2): p. 263-268.

11. Matveev, B.A., et al., *Mid-infrared (3-5 μm) LEDs as sources for gas and liquid sensors.* Sensors and Actuators B: Chemical, 1997. **39**(1–3): p. 339-343.

12. Aidaraliev, M., et al., *Light emitting diodes for the spectral range of λ=3.3–4.3 μm fabricated from the InGaAs-and InAsSbP-based solid solutions: Electroluminescence in the temperature range of 20–180°C.* Semiconductors, 2000. **34**(1): p. 104-107.

13. Matveev, B.A., et al., *Towards efficient mid-IR LED operation: optical pumping, extraction or injection of carriers?* Journal of Modern Optics, 2002. **49**(5-6): p. 743-756.

14. Zotova, N., et al., *Luminescence of multilayer structures based on InAsSb at λ = 6−9 μm.* Semiconductors, 2005. **39**(2): p. 214-217.

15. Zotova, N., et al., *Flip-chip LEDs with deep mesa emitting at 4.2 μm.* Semiconductors, 2006. **40**(6): p. 697-703.

16. Gao, H.H., et al., *InAsSb/InAsSbP light emitting diodes for the detection of CO and CO_2 at room temperature.* Journal of Physics D: Applied Physics, 1999. **32**(15): p. 1768.

17. Krier, A., V.V. Sherstnev, and H.H. Gao, *A novel LED module for the detection of H_2S at 3.8 μm.* Journal of Physics D: Applied Physics, 2000. **33**(14): p. 1656.

18. Krier, A. and V.V. Sherstnev, *Powerful interface light emitting diodes for methane gas detection.* Journal of Physics D: Applied Physics, 2000. **33**(2): p. 101.

19. Carrington, P.J., et al., *Room temperature midinfrared electroluminescence from InSb/InAs quantum dot light emitting diodes.* Applied Physics Letters, 2008. **93**(9): p. 091101.

20. Krier, A., et al., *The development of room temperature LEDs and lasers for the mid-infrared spectral range.* physica status solidi (a), 2008. **205**(1): p. 129-143.

21. Tang, P.J.P., et al., *Efficient 300 K light-emitting diodes at $\lambda \sim 5$ and ~ 8 μm from InAs/In($As_{1-x}Sb_x$) single quantum wells.* Applied Physics Letters, 1998. **72**(26): p. 3473-3475.

22. Pullin, M.J., et al., *Room-temperature InAsSb strained-layer superlattice light-emitting diodes at lambda = 4.2 μm with AlSb barriers for improved carrier confinement.* Applied Physics Letters, 1999. **74**(16): p. 2384-2386.

23. Koerperick, E.J., et al., *Active Region Cascading for Improved Performance in InAs/GaSb Superlattice LEDs.* Quantum Electronics, IEEE Journal of, 2008. **44**(12): p. 1242-1247.

24. Koerperick, E.J., et al., *High-Power MWIR Cascaded InAs/GaSb Superlattice LEDs.* Quantum Electronics, IEEE Journal of, 2009. **45**(7): p. 849-853.

25. Koerperick, E.J., et al., *Cascaded Superlattice InAs/GaSb Light-Emitting Diodes for Operation in the Long-Wave Infrared.* Quantum Electronics, IEEE Journal of, 2011. **47**(1): p. 50-54.

26. Garbuzov, D.Z., *Reradiation effects, lifetimes and probabilities of band-to-band transitions in direct A_3B_5 compounds of GaAs type.* Journal of Luminescence, 1982. **27**(1): p. 109-112.

27. Culpepper, R.M. and J.R. Dixon, *Free-Carrier Absorption in n-Type Indium Arsenide.* J. Opt. Soc. Am., 1968. **58**(1): p. 96-101.

28. Schroder, D.K., R.N. Thomas, and J.C. Swartz, *Free Carrier Absorption in Silicon.* Solid-State Circuits, IEEE Journal of, 1978. **13**(1): p. 180-187.

29. Chandola, A., R. Pino, and P.S. Dutta, *Below bandgap optical absorption in tellurium-doped GaSb.* Semiconductor Science and Technology, 2005. **20**(8): p. 886.

30. Vurgaftman, I., J.R. Meyer, and R. Mohan, *Band parameters for III--V compound semiconductors and their alloys.* Journal of Applied Physics, 2001. **89**(11): p. 5815-5875.

31. Gao, H.H. and et al., *InAsSb/InAsSbP light emitting diodes for the detection of CO and CO_2 at room temperature.* Journal of Physics D: Applied Physics, 1999. **32**(15): p. 1768.

32. Kipshidze, G., et al., *High-Power 2.2-μm Diode Lasers With Metamorphic Arsenic-Free Heterostructures.* Photonics Technology Letters, IEEE, 2011. **23**(5): p. 317-319.

33. Onabe, K., *Unstable Regions in III-V Quaternary Solid Solutions Composition Plane Calculated with Strictly Regular Solution Approximation.* Japanese Journal of Applied Physics, 1982. **21**(Part 2, No. 6): p. L323.

34. Tang, P., et al., *4-11 μm infrared emission and 300 K light emitting diodes from arsenic-rich $InAs_{1-x}Sb_x$ strained layer superlattices.* Semiconductor Science and Technology, 1995. **10**(8): p. 1177.

35. Smith, D.L. and C. Mailhiot, *Proposal for strained type II superlattice infrared detectors.* Journal of Applied Physics, 1987. **62**(6): p. 2545-2548.

36. Pikhtin, N., et al., *Internal optical loss in semiconductor lasers.* Semiconductors, 2004. **38**(3): p. 360-367.

37. Bastard, G., *Superlattice band structure in the envelope-function approximation.* Physical Review B, 1981. **24**(10): p. 5693-5697.

38. Bastard, G., *Theoretical investigations of superlattice band structure in the envelope-function approximation.* Physical Review B, 1982. **25**(12): p. 7584-7597.

39. Haugan, H.J., et al., *Optimization of mid-infrared InAs/GaSb type-II superlattices.* Applied Physics Letters, 2004. **84**(26): p. 5410-5412.

40. Venkateswaran, U.D., et al., *Strain mapping in [111] and [001] InGaAs/GaAs superlattices.* Applied Physics Letters, 1990. **56**(3): p. 286-288.

41. Levy, R.A., et al., *A comparative study of plasma enhanced chemically vapor deposited Si-O-H and Si-N-C-H films using the environmentally benign precursor diethylsilane.* Materials Letters, 2002. **54**(2–3): p. 102-107.

42. Garcia, J.C., et al., *Epitaxially stacked lasers with Esaki junctions: A bipolar cascade laser.* Applied Physics Letters, 1997. **71**(26): p. 3752.

43. Kim, J.K., et al., *Near-room-temperature continuous-wave operation of multiple-active-region 1.55 μm vertical-cavity lasers with high differential efficiency.* Applied Physics Letters, 2000. **77**(20): p. 3137.

44. Yang, R.Q. and Y. Qiu, *Bipolar cascade lasers with quantum well tunnel junctions.* Journal of Applied Physics, 2003. **94**(11): p. 7370.

45. Prineas, J.P., et al., *Cascaded active regions in 2.4 μm GaInAsSb light-emitting diodes for improved current efficiency.* Applied Physics Letters, 2006. **89**(21): p. 211108.

46. Jung, S., et al., *Single spatial mode 2–2.2 μm diode lasers fabricated by selective wet etching.* Semiconductor Science and Technology, 2012. **27**(8): p. 085004.

47. Tsang, W.T., et al., *Molecular beam epitaxial growth of $In_{1-x}Ga_xAs_{1-y}Sb_y$ lattice matched to GaSb.* Applied Physics Letters, 1985. **46**(3): p. 283-285.

48. Jung, S., et al., *GaSb-Based Mid-Infrared Single Lateral Mode Lasers Fabricated by Selective Wet Etching Technique with an Etch Stop Layer.* Journal of Electronic Materials, 2012. **41**(5): p. 899-904.

49. Flatt, et al., *Carrier recombination rates in narrow-gap InAs/$Ga_{1-x}In_xSb$-based superlattices.* Physical Review B, 1999. **59**(8): p. 5745.

50. Ongstad, A.P., et al., *Linewidth analysis of the photoluminescence from InAs/GaSb/InAs/AlSb type-II superlattices.* Journal of Applied Physics, 2000. **87**(11): p. 7896-7902.

51. Donetsky, D., et al., *Carrier lifetime measurements in short-period InAs/GaSb strained-layer superlattice structures.* Applied Physics Letters, 2009. **95**(21): p. 212104-3.

52. Das, N.C., et al., *Long-wave (10 μm) infrared light emitting diode device performance.* Solid-State Electronics, 2008. **52**(11): p. 1821-1824.

53. Cole, B.E., et al., *512×512 infrared cryogenic scene projector arrays.* Sensors and Actuators A: Physical, 1995. **48**(3): p. 193-202.

54. Beasley, D.B., et al. *Dynamic IR scene projector based upon the digital micromirror device*. 2001. Orlando, FL, USA: SPIE.

55. Thompson, G.H.B., *Physics of semiconductor laser devices*, 1980: Wiley.

56. Schubert, E.F., *Light emitting diodes*, 2003: Cambridge Univ. Press.

57. Oliver, D. and et al., *Selective and non-selective wet-chemical etchants for GaSb-based materials.* Semiconductor Science and Technology, 2004. **19**(11): p. 1250.

58. Ozden, I., et al., *A dual-wavelength indium gallium nitride quantum well light emitting diode.* Applied Physics Letters, 2001. **79**(16): p. 2532-2534.

59. Sun, D., et al., *Red and infrared side by side semiconductor quantum well lasers integrated on a GaAs substrate.* Applied Physics Letters, 1998. **73**(13): p. 1793-1795.

60. Aidaraliev, M., et al., *Two-wavelength emission from a GaInPAsSb/InAs structure with a broken-gap isotype heterojunction and a p-n junction in the substrate.* Technical Physics Letters, 2002. **28**(12): p. 1001-1003.

61. Choi, H.W., et al., *GaN micro-light-emitting diode arrays with monolithically integrated sapphire microlenses.* Applied Physics Letters, 2004. **84**(13): p. 2253-2255.

62. Das, N.C., *Increase in midwave infrared light emitting diode light output due to substrate thinning and texturing.* Applied Physics Letters, 2007. **90**(1): p. 011111-3.

63. Schnitzer, I., et al., *30% external quantum efficiency from surface textured, thin-film light-emitting diodes.* Applied Physics Letters, 1993. **63**(16): p. 2174-2176.

64. Kim, J.K., et al., *Light-Extraction Enhancement of GaInN Light-Emitting Diodes by Graded-Refractive-Index Indium Tin Oxide Anti-Reflection Contact.* Advanced Materials, 2008. **20**(4): p. 801-804.

65. Fan, S., et al., *High Extraction Efficiency of Spontaneous Emission from Slabs of Photonic Crystals.* Physical Review Letters, 1997. **78**(17): p. 3294-3297.

66. Schubert, E.F., et al., *Highly Efficient Light-Emitting Diodes with Microcavities.* Science, 1994. **265**(5174): p. 943-945.

67. Rouillard, Y., et al., *Edge and vertical surface emitting lasers around 2.0–2.5 μm and their applications.* Philosophical Transactions of the Royal Society of London. Series A:Mathematical, Physical and Engineering Sciences, 2001. **359**(1780): p. 581-597.

68. Daneu, V., et al., *Spectral beam combining of a broad-stripe diode laser array in an external cavity.* Opt. Lett., 2000. **25**(6): p. 405-407.

69. Garcia, M., et al., *Low threshold high-power room-temperature continuous-wave operation diode laser emitting at 2.26 μm.* Photonics Technology Letters, IEEE, 2004. **16**(5): p. 1253-1255.

70. Rattunde, M., et al., *GaSb-based 2.X μm quantum-well diode lasers with low beam divergence and high output power.* Applied Physics Letters, 2006. **88**(8): p. 081115-3.

71. Garbuzov, D.Z., et al., *4 W quasi-continuous-wave output power from 2 μm AlGaAsSb/InGaAsSb single-quantum-well broadened waveguide laser diodes.* Applied Physics Letters, 1997. **70**(22): p. 2931-2933.

72. Rui, L., et al., *High-Power 2.2-μm Diode Lasers With Heavily Strained Active Region.* Photonics Technology Letters, IEEE, 2011. **23**(10): p. 603-605.

73. Clawson, A.R., *Guide to references on III–V semiconductor chemical etching.* Materials Science and Engineering: R: Reports, 2001. **31**(1–6): p. 1-438.

74. Kawaguchi, H. and T. Kawakami, *Transverse-mode control in an injection laser by a strip-loaded waveguide.* Quantum Electronics, IEEE Journal of, 1977. **13**(8): p. 556-560.

75. Agrawal, G., *Lateral analysis of quasi-index-guided injection lasers: Transition from gain to index guiding.* Lightwave Technology, Journal of, 1984. **2**(4): p. 537-543.

76. Achtenhagen, M., A. Hardy, and C.S. Harder, *Lateral mode discrimination and self-stabilization in ridge waveguide laser diodes.* Photonics Technology Letters, IEEE, 2006. **18**(3): p. 526-528.

77. Alibert, C., et al., *Refractive indices of AlSb and GaSb-lattice-matched $Al_xGa_{1-x}As_ySb_{1-y}$ in the transparent wavelength region.* Journal of Applied Physics, 1991. **69**(5): p. 3208-3211.

78. Jianfeng, C., et al., *Effect of Quantum Well Compressive Strain Above 1% On Differential Gain and Threshold Current Density in Type-I GaSb-Based Diode Lasers.* Quantum Electronics, IEEE Journal of, 2008. **44**(12): p. 1204-1210.

79. Hosoda, T., et al., *Continuous-wave room temperature operated 3.0 μm type I GaSb-based lasers with quinternary AlInGaAsSb barriers.* Applied Physics Letters, 2008. **92**(9): p. 091106-3.

80. Chen, J., G. Kipshidze, and L. Shterengas, *Diode lasers with asymmetric waveguide and improved beam properties.* Applied Physics Letters, 2010. **96**(24): p. 241111-3.

81. Hakki, B.W. and T.L. Paoli, *Gain spectra in GaAs double - heterostructure injection lasers.* Journal of Applied Physics, 1975. **46**(3): p. 1299-1306.

82. Hu, S.Y., et al., *Lateral carrier diffusion and surface recombination in InGaAs/AlGaAs quantum-well ridge-waveguide lasers.* Journal of Applied Physics, 1994. **76**(8): p. 4479-4487.

83. Letal, G.J., et al., *Determination of active-region leakage currents in ridge-waveguide strained-layer quantum-well lasers by varying the ridge width.* Quantum Electronics, IEEE Journal of, 1998. **34**(3): p. 512-518.

84. Herzog, W.D., et al., *Beam divergence and waist measurements of laser diodes by near-field scanning optical microscopy.* Applied Physics Letters, 1997. **70**(6): p. 688-690.

85. Schlereth, K.H. and M. Tacke, *The complex propagation constant of multilayer waveguides: an algorithm for a personal computer.* Quantum Electronics, IEEE Journal of, 1990. **26**(4): p. 627-630.

86. Luryi, S. and M. Gouzman, *Feasibility of an optical frequency modulation system for free-space optical communications.* International Journal of High Speed Electronics and Systems, 2006. **16**(02): p. 559-566.

87. Hayes, R.R., *Analog Intersatellite Communication with Frequency-Modulated Light. Part 1. Noise Theory.* Appl. Opt., 2001. **40**(35): p. 6445-6465.

88. Kosterev, A.A., et al., *Cavity Ringdown Spectroscopic Detection of Nitric Oxide with a Continuous-Wave Quantum-Cascade Laser.* Appl. Opt., 2001. **40**(30): p. 5522-5529.

89. Beyer, T., M. Braun, and A. Lambrecht, *Fast gas spectroscopy using pulsed quantum cascade lasers.* Journal of Applied Physics, 2003. **93**(6): p. 3158-3160.

90. Bismuto, A., et al., *Electrically tunable, high performance quantum cascade laser.* Applied Physics Letters, 2010. **96**(14): p. 141105-3.

91. Yu, Y., et al., *Voltage Tunability of Quantum Cascade Lasers.* Quantum Electronics, IEEE Journal of, 2009. **45**(6): p. 730-736.

92. Suchalkin, S., et al., *Widely tunable type-II interband cascade laser.* Applied Physics Letters, 2006. **88**(3): p. 031103-3.

93. Teissier, J., et al., *Electrical modulation of the complex refractive index in mid-infrared quantum cascade lasers.* Opt. Express, 2012. **20**(2): p. 1172-1183.

94. Chen, G., et al., *Optically induced fast wavelength modulation in a quantum cascade laser.* Applied Physics Letters, 2010. **97**(1): p. 011102-3.

95. Faist, K., et al., *Bound-to-continuum and two-phonon resonance, quantum-cascade lasers for high duty cycle, high-temperature operation.* Quantum Electronics, IEEE Journal of, 2002. **38**(6): p. 533-546.

96. Paskov, P.P., *Refractive indices of InSb, InAs, GaSb, $InAs_xSb_{1-x}$, and $In_{1-x}Ga_xSb$: Effects of free carriers.* Journal of Applied Physics, 1997. **81**(4): p. 1890-1898.

97. Alam, M.S., et al. *Refractive Index, Absorption Coefficient, and Photoelastic Constant: Key Parameters of InGaAs Material Relevant to InGaAs-Based Device Performance*. in *Indium Phosphide & Related Materials, 2007. IPRM '07. IEEE 19th International Conference on*. 2007.

98. Evans, C., et al., *The role of temperature in quantum-cascade laser waveguides.* Journal of Computational Electronics, 2012. **11**(1): p. 137-143.

99. Suchalkin, S., et al., *In-plane and growth direction electron cyclotron effective mass in short period InAs/GaSb semiconductor superlattices.* Journal of Applied Physics, 2011. **110**(4): p. 043720-5.

100. Sirtori, C., et al., *Low-loss Al-free waveguides for unipolar semiconductor lasers.* Applied Physics Letters, 1999. **75**(25): p. 3911-3913.

101. Nudelman, S., *The Detectivity of Infrared Photodetectors.* Appl. Opt., 1962. **1**(5): p. 627-636.

102. Jones, R.C., *Immersed Radiation Detectors.* Appl. Opt., 1962. **1**(5): p. 607-613.

103. Piotrowski, J. and Rogalski, Antoni, *High-operating-temperature infrared photodetector*, 2007, USA: SPIE.

104. Cowan, V.M., et al., *Low-temperature noise measurements of an InAs/GaSb-based nBn MWIR detector*. 2011: p. 801210-801210.

105. Rodriguez, J.B., et al., *nBn structure based on InAs/GaSb type-II strained layer superlattices.* Applied Physics Letters, 2007. **91**(4): p. 043514-2.

106. Plis, E., et al., *Lateral diffusion of minority carriers in InAsSb-based nBn detectors.* Applied Physics Letters, 2010. **97**(12): p. 123503-3.

107. Schuster, J., et al., *Numerical Simulation of InAs nBn Back-Illuminated Detectors.* Journal of Electronic Materials, 2012. **41**(10): p. 2981-2991.

108. NSMSemiconductor. Available from: http://www.ioffe.rssi.ru/SVA/NSM/Semicond/.

109. Cheung, D.T., et al., *Backside-illuminated $InAs_{1-x}Sb_x$-InAs narrow-band photodetectors.* Applied Physics Letters, 1977. **30**(11): p. 587-589.

110. Dixon, J.R. and J.M. Ellis, *Optical Properties of n-Type Indium Arsenide in the Fundamental Absorption Edge Region.* Physical Review, 1961. **123**(5): p. 1560-1566.

Appendix 1

We assume that the signal of the detector is proportional to the total optical power emitted by the blackbody. Since the blackbody is placed close to the input aperture of the integrating sphere, we assume that all the photons emitted by the blackbody reach the sphere. The total number of photons with wavelengths in the range from λ to λ+dλ emitted by the blackbody into the integration sphere is

$$N_{total}(\lambda) = S_{eff} R(\lambda, T_B) \frac{\lambda}{hc} \quad \text{A-1}$$

, where S_{eff} is the effective area of the blackbody and $R(\lambda,T_B)$ is the spectral radiant exitance of the black body:

$$R(\lambda, T_B) = \frac{2hc^2}{\lambda^5} \frac{1}{exp\left(\frac{hc}{\lambda k T_B}\right) - 1} \quad \text{A-2}$$

, where T_B is the black body temperature. The number of electron-hole pairs produced per unit time in the detector by the blackbody emission is

$$N_B = \frac{\eta S_{eff} \int_0^\infty D(\lambda) R(\lambda, T_B) \frac{\lambda}{hc} d\lambda}{\int_0^\infty D(\lambda') d\lambda'} \quad \text{A-3}$$

, where η is the coefficient describing the detector efficiency and attenuation of the integrating sphere, $D(\lambda)$ is the detector sensitivity in arbitrary units. During the calibration procedure, we measure the voltage (ΔV_B) from the preamplifier as a response of the setup to the modulated signal from the blackbody. The measured voltage ΔV_B is proportional to N_B,

$$N_B = k \Delta V_B \quad \text{A-4}$$

Combining A-3 and A-4, we obtain,

$$k = \frac{\eta S_{eff} \int_0^\infty D(\lambda) R(\lambda, T_B) \frac{\lambda}{hc} d\lambda}{\Delta V_B \int_0^\infty D(\lambda') d\lambda'} \quad \text{A-5}$$

. The coefficient k is determined by the detector characteristics and trans-impedance gain of the preamplifier. The number of electron-hole pairs produced in the detector by LED emission is

$$N_{LED} = \frac{\eta P_{LED} \int_0^\infty D(\lambda') S(\lambda' - \lambda_0) \frac{\lambda'}{hc} d\lambda'}{\int_0^\infty D(\lambda''') d\lambda''' \int_0^\infty S(\lambda'' - \lambda_0) d\lambda''} \quad \text{A-6}$$

, where $S_{\lambda_0}(\lambda) \equiv S(\lambda - \lambda_0)$ is the LED emission spectrum normalized to the total optical power P_{LED}. We assume that the shape of the LED spectrum does not depend on the peak wavelength λ_0. The same coefficient k in A-5 can be used to obtain the voltage signal ΔV_{LED} due to LED emission

$$N_{LED} = k \Delta V_{LED} \quad \text{A-7}$$

Combining A-5, A-6 and A-7, we obtain,

$$K(\lambda_0) = \frac{S_{eff} \int_0^\infty S(\lambda'' - \lambda_0) d\lambda'' \int_0^\infty D(\lambda) R(\lambda, T_B) \lambda d\lambda}{\Delta V_B \int_0^\infty D(\lambda') S(\lambda' - \lambda_0) \lambda' d\lambda'} \quad \text{A-8}$$

Both the detector sensitivity (*D*) and LED spectrum (*S*) can be taken in arbitrary units.